Western Australian School of Mines
Minerals, Energy and Chemical Engineering

Rock Physics Characterization using Physical Methods on Powders

Zubair Ahmed

This thesis is presented for the Degree of
Doctor of Philosophy
of
Curtin University

September 2018

Declaration

To the best of my knowledge and belief this thesis contains no material previously published by any other person except where due acknowledgment has been made.

This thesis contains no material which has been accepted for the award of any other degree or diploma in any university.

Signature: 

Date: 01-04-2019

To my eldest sister

Shamsun Nahar Begum

Abstract

This dissertation describes a detailed investigation of the microstructural properties of unconsolidated granular samples, their impact on laboratory ultrasonic velocities and a methodology with its implementation to obtain the elastic properties of the constituent grains utilising Hertzian contact models. To do so, we prepare four quartz sand samples with different sorting indices and grain shape factors. We perform ultrasonic velocity measurements through these samples that are subjected to uniaxial stress inside a confined cylindrical chamber. These velocities provide the dynamic effective elastic properties, which are included in the contact-based effective medium models to calculate the elastic properties of the grains. After successfully implementing this technique in the mono mineral pack, we apply this to three samples of rock powders collected during drilling in hard rock mineral exploration to obtain the elastic properties of the respective core samples.

High resolution micro-CT images provide accurate micro-structural parameters that are crucial in understanding the elastic behaviour of a granular medium. We develop a computer code to calculate such parameters: namely, the coordination number and contact surface areas. We also determine the shape characteristics of the grains and study their potential relationship with those micro-structural parameters. We observe that well-sorted samples with more spherical and rounded grains have higher coordination number and contact surface area than those in poorly sorted samples with less spherical and rounded grains in the same stress and porosity range. Inside a particular sand pack, the sphericity of the grains is weakly correlated with the coordination numbers; less spherical grains tend to have higher coordination numbers.

Grain shape factors and sorting indices have a major impact on the seismic wave velocities. Well-sorted samples with more spherical and rounded grains have higher velocities than those of the poorly sorted samples with less spherical and rounded grains. We carefully determine the experiment parameters such as loading–unloading cycles to settle the grains, and top stress limit to avoid grain crushing and to restrict for a constant coordination number which otherwise increases much with increasing stress. Coordination numbers calculated from the micro-CT images are found very efficient in modelling the effective bulk moduli of the samples. The approach of using a frictional

parameter that is calculated from the velocity (dynamic) data itself tackles the longstanding problem of over-predicting the effective shear modulus of the pack. Our results for the elastic properties of the quartz grains calculated using the contact models are very close to the elastic properties of quartz. This result encourages us to apply this technique to rock powders that are composed of a number of minerals.

Individual mineral composition has to be taken into account in studying the elastic properties of the rock powders. We have extended an existing contact-based model that integrates the combined effect of multiple minerals on the effective elastic properties of the granular pack. Integrating this parameter into our technique developed for quartz sand seems a viable option to determine the elastic properties of the corresponding core sample. Changes in coordination number and porosity with stress are found significantly higher compared with the changes observed in quartz sand samples. Variation in grain shapes due to different minerals, especially the presence of platy minerals, could be a vital reason for that. One of the three samples shows the elastic properties of the constituent grains are close to the elastic properties of the corresponding solid core sample; refinement of the experiment procedure may improve the results for the other two as well. Elastic properties of the constituent grains obtained using our technique can be helpful in determining the elastic properties of hard rock core samples that might be broken or absent. Additionally, this technique can be used to calculate the elastic properties of the solid phase for rock physics characterisation; for example, in fluid substitution for unconsolidated sand reservoirs.

Acknowledgements

I would like to express my heartfelt gratitude to my advisor Professor Dr Maxim Lebedev for providing me this huge opportunity to carry out my research as a DET CRC Project 3.2 PhD student. I am indebted to him for his continuous support, encouragement and guidelines that helped shaping up this research. His devotion to the students is exemplary and I am fortunate that I have got the opportunity to work under his supervision.

It gives me immense pleasure to thank the members of my advisory panel, Dr Mahyar Madadi, Dr Stanislav Glubokovskikh, and Dr Andrej Bóna for their support, meticulous suggestions and astute criticism in times of need. I would also like to extend my gratitude to Professor Dr Boris Gurevich for his comments and suggestions. My heartfelt thanks to Dr Andrew Squelch and Dr Yathunanthan Sivarajah for their help in using the image processing software.

I am indebted to my co-advisor Dr. Yulia Uvarova for her valuable suggestions and support throughout my study especially by providing the rock powder samples. I am immensely grateful to Professor Dr David Giles for his kind help in collecting the core samples.

I am obliged to the DET CRC, Curtin International Postgraduate Research Scholarship and Australian Government Research Training Program for the scholarships awarded to me. I am also grateful to Australian Society of Exploration Geophysicists (ASEG) for providing a research grant (RF16M04) for two years.

I am grateful to National Geosequestration Laboratory (NGL) for letting me acquire micro-CT images and Pawsey Supercomputing Centre for letting use their supercomputing facility to process those images.

My profound gratitude to our research secretary Miss Nichole Sik for her tremendous support in administrative purposes. I would also like to thank our former administrative officers Ms Deirdre Hollingsworths, Mrs Lynda Bergey and research secretary Miss Zuzzanna Kuklinski for their support throughout my endeavour at Curtin.

I would like to thank my colleagues and friends, especially Roman, Alexey, Bryce, Nazanin, Shahadat, Thong, Felix, Kevin, and Dmitry for their support and encouragements.

No words would be enough to express my hearty feelings to my family for their unconditional support, love and encouragement. I would like to remember the memory of my father for his *can do* attitude. I would like to pay my tribute to my mother and sisters who always believe in me. I am deeply indebted to the caring and support from my wife Lutfun Nahar to keep every aspect of our lives orderly especially managing our two little sons Zahian Ahmed and Zuhair Ahmed at home. They have been staying by my side and patiently supporting me in all the ups and downs I have been going throughout the doctoral study.

This work has been supported by the Deep Exploration Technologies Cooperative Research Centre whose activities are funded by the Australian Government's Cooperative Research Centre Programme.

Table of contents

List of figures

List of tables

1. Introduction

1.1. Motivation

Geophysical methods are being widely used to delineate the subsurface in order to better understand the potential targets in mineral and hydrocarbon exploration. Most of these methods are non-invasive and carried out over the surface to capture different physical responses of the subsurface formations. To obtain more accurate physical properties, laboratory measurements on extracted core samples are robustly performed. However, extraction of solid core samples needs extra arrangements at the drilling site. This can increase the operation time and cost, and require more expert personnel to be deployed, with specialised instruments. Moreover, sometimes the acquired cores can be fragmented into pieces that can no longer be used for certain laboratory testing, such as seismic velocities, elastic properties, density, resistivity and so on. Considering these drawbacks of the usage of solid core samples, one alternative is to use the rock powders that come up during drilling to obtain the elastic properties of the formation from where they are fragmented. In contrast to the extra procedure required to extract the drill core, rock powders are the customary product of any drilling in a hard rock environment for mineral exploration. Proper sampling of these powders from suitable intervals can be beneficial in studying the elastic properties of the subsurface formations where core samples are unavailable.

Another motivation comes from the use of *ad hoc* elastic properties of the solid phase in fluid substitution for determining seismic wave velocities through fluid saturated porous medium. Fluid substitution is one of the key steps for rock physics characterisation in the presence of fluids with varying saturations. In this step, most often elastic properties of mineral quartz or effective medium bounds are readily used even though the rock may be composed of multiple minerals of varying elasticity. In place of this arbitrary elastic constant, using the effective elastic properties of the mineral composite as the elastic property of the solid phase can provide better results.

Both of these motivations lead to a common solution which lies in effective medium models that involve grain-to-grain contacts in terms of the contact stiffness formulated in a pack of granular materials. The contact stiffness is dependent on the elastic

properties of individual grains and the geometry of the contacts. Recent advancement in the acquisition of high resolution images by micro computed tomography (micro-CT) and the capability of high-speed computation provide the leverage to obtain accurate microstructural parameters of the granular pack in micrometre scale. Sophisticated ultrasonic measurements can also be helpful to measure the dynamic elastic moduli of the granular pack. In essence, both micro-CT imaging and ultrasonic velocity measurement are the two primary tools and the effective medium model is the backbone of the method that I have aimed to use in this study to pursue the objectives.

1.2. Background

Each chapter in this thesis contains background studies relating to its topic. Additionally, in the following sections, I provide a discussion on the relevant background of the micro-CT imaging technique and ultrasonic velocity measurement, which are not included in the subsequent chapters.

1.2.1. Micro-computed tomography

X-ray computed tomography (XCT) is a non-destructive and non-invasive imaging technique where a number of individual radiographs taken from different angles are reconstructed to delineate the three-dimensional internal structure of a material of interest. Micro-computed tomography (micro-CT) is named as a variant of XCT that captures higher-resolution images in micrometre scale. The repetition of various inspections – which may include changing source parameters, resolutions and so on – during image acquisition after reinstalling the sample multiple times is another great advantage. Moreover, the acquired digital images can be stored forever and used as many times as needed for various analyses of interest. However, several disadvantages are also noteworthy. Perhaps the biggest one is the representative sample size and corresponding spatial resolution. For example, to image a sandstone at pore scale in micrometres, the sample size should be a couple of millimetres, which might not provide the calculated effective properties that are representative of the whole rock sample. Maire and Withers (2014) presented an excellent review on the journey of the micro-CT imaging technique to this point, including the obstacles and limitations that it faced and their potential solutions. These limitations included the suitability of

choosing right type of X-ray source with their corresponding spatial and temporal resolutions, inadequate algorithms for iterative reconstruction of the acquired projections, the lacking of error bars in the quantitative analysis of the petrophysical properties and underused strategy in dealing with the representative elementary volume (REV). In another angle to tackle this REV problem, Dvorkin et al. (2011) pointed out that computational rock physics that calculates effective properties from micro-CT images can be a viable option. They proposed to calculate those properties in subsamples of different sizes and follow the trend of two or more properties. This trend could link the properties between laboratory scale and the regional scale of a particular formation type.

Implementation of the micro-CT imaging method has been widespread over the last decade throughout a number of new applications in diversified fields including material and biomedical sciences (Stock 2009, Stock 2013). Cnudde and Boone (2013) provided a review on the principle, advantages and limitations of micro-CT imaging and shed light on the already established and prospective applications in the field of geoscience. Mees et al. (2003) demonstrated its applications in studying porosity and fluid flow to investigate potential reservoirs in the fields of petroleum geology, rock mechanics and soil science. Berg et al. (2017) provided an overview of digital rock technology in current industrial applications. Their findings referred to the well-established applications in the field of formation evaluation and irreducible water saturation by implementing the flow simulation in the acquired images.

Modifications to the instrumentation and customised approaches to deal with particular problems have become common since early this decade. Iovea et al. (2009) showed the usage of a dual energy source for quantitative analysis of textural features resulting from the chemical and mineralogical composition in various rock types. Madonna et al. (2013) described the advantages of using Synchrotron Radiation X-ray Tomographic Microscopy (SRXTM) over traditional X-ray micro-CT in terms of high temporal and spatial resolution. Athanassiadis et al. (2014) developed an experimental setup that integrates a medical mini C-arm with traditional material testing apparatus for imaging granular samples by X-ray tomography while the sample is subjected to loading. Schindler et al. (2017) had a description of an experimental setup that included both micro-CT imaging and ultrasonic velocity measurement with increasing pressure

performed on the same sample to study the interaction between gas hydrate and host rocks. Bultreys et al. (2016) demonstrated that the advancement of micro-CT imaging with sub-minute time resolution could be effective in visualising drainage events of solute transport in porous media. This real-time imaging technique seemed beneficial to reservoir managements by understanding the behaviour of the fluid flow in pore scale. Moreno-Atanasio et al. (2010) presented a review on combining X-ray micro tomography with computer simulation to solve problems related to the transport properties of rocks, packing of particles with different shapes, mechanical loading and sintering. They emphasised that the link between these two techniques should be based on quantitative parameters such as inter-particle contact numbers, force networks or shape factors of the grains.

Different techniques in numerical simulation to calculate the effective elastic properties or seismic wave velocities from the micro-CT images are also finding their way to success in some cases. Arns et al. (2002) successfully derived the relationship between the elastic property and porosity of Fontainebleau sandstone using a finite element method developed by Garboczi and Day (1995). Shulakova et al. (2013) developed an approach to upscale the elastic moduli calculated from micro-CT images using a finite-element simulation and found a good match with the laboratory-measured data. Madonna et al. (2012) predicted seismic wave velocities on micro-CT images of Berea sandstone by numerical simulation of dynamic wave propagation developed by Saenger et al. (2004) and compared these with the laboratory measurement. Results from the numerical simulation were found to be quite a bit higher than the measured velocities in the experiment. They assumed that the micro-cracks and grain-to-grain contacts that were not resolvable by the images could be the cause of such discrepancy. They also proposed a calibration procedure to predict the velocities using both micro-CT images and laboratory measurement.

Implementation of micro-CT images to solve different rock physics problems is gaining more solid ground day by day. Andrä et al. (2013a and 2013b) provided benchmarks on this progress that are evaluated in terms of image processing parameters and algorithms for computing effective properties. Dvorkin et al. (2011) concluded that computational rock physics had already become a powerful technique and would grow tremendously in the future. They also pointed out that this branch of rock physics had

provided reliable results besides laboratory experiments which could contribute to the applied technology and fundamental science.

1.2.2. Ultrasonic velocity measurement

Ultrasonic velocities are commonly measured following a pulse transmission technique described in Birch (1960) and Christensen (1965). A rectangular electric pulse was generated and applied to a transducer made of barium titanate which imparts compressional pulse to the attached face of the sample. After travelling through the sample, that mechanical pulse was received by a similar transducer attached to the opposite face of the sample. This received mechanical pulse was converted to an electric signal that was amplified and displayed on an oscilloscope. To measure the travel time, simultaneously and separately, the same initial pulse was sent through a mercury column with a variable height. One transducer was set at the base of the column and the other was mounted on a plate that could be vertically moved to adjust the height. The height of the mercury column was then adjusted to match the first arrival of the signal through the mercury column with the first arrival that went through the sample. Thus the travel time was taken from the known velocity of mercury and was used to calculate the velocity of the sample. Nowadays, instead of using the mercury delay technique for time registration, sophisticated oscilloscopes can monitor the pulse transmission time after averaging a number of transmitted waveforms. Sophisticated piezoelectric sensors made of PZT (Lead Zirconate Titanate) ceramic materials and single mineral crystals (Gallium Phosphate, Quartz, Tourmaline) are being widely used.

Modifications of the experiment setup, including the instruments as well are quite common in the literature. Timur (1977) added a temperature component with overburden and pore fluid pressure system to simulate reservoir conditions that are normally found at the subsurface. He measured the ultrasonic velocities in that setup and observed that increasing temperature caused decreasing velocity. Marion (1990) Added electrical conductivity measurement along with the ultrasonic measurement setup for velocity measurements through a granular sample immersed in fluid. This additional setup was to test the sensitivity of the velocity to the rheological transition from suspension to load bearing. Prasad and Manghnani (1997) included the pore pressure component in their experiment setup for measuring the ultrasonic P wave

velocity of Berea and Michigan sandstones. Zimmer (2003) improvised the ultrasonic transducer by incorporating low-frequency broadband piezoelectric crystals and low-impedance face plates to accurately capture the transmitted signal through highly attenuated unconsolidated samples. Fawad et al. (2011) describe how their experiment setup had separate P and S wave transducers to measure the respective velocities of granular samples, which were put inside the oedometric cell under uniaxial stress.

1.3. Research objective

My principal objective in this study is to calculate the elastic properties of a rock from physical measurements on the powder that comes up during drilling. To achieve that goal, I have set the following milestones in each step:

- To investigate the micro-structural properties of the granular pack by analysing high-resolution micro-CT images. This investigation consists of finding potential relationships among the grain shape factors and micro-structural properties that could impact the elastic properties of the granular pack.
- To develop a simple and robust technique to estimate the elastic properties of the constituent grains from the ultrasonic velocity data measured in a granular pack that contains a single mineral. Additionally, to study the impact of shape factors and intergranular arrangement on the elastic wave velocities through the granular pack.
- To implement this technique on the rock powder samples of multiple minerals that are collected from an exploratory drilling to obtain the elastic properties of the hard rocks from where they have been fragmented. Consequently, to develop a model that calculates the effective elastic property of the mineral composite inside the pack.

1.4. Thesis organisation

This thesis is based on three journal papers (one accepted and two submitted) as three chapters from Chapter 2 to Chapter 4. All three chapters are sequentially connected. Micro-structural findings of the granular samples in Chapter 2 are used in the contact-based models described in Chapter 3. Further, the prototype developed in Chapter 3 for

calculating the elastic property of the constituent mineral in mono-mineral quartz sand samples is implemented to poly mineral rock powders in Chapter 4.

Chapter 2 is published in *Geophysical Prospecting* as the first part of twin papers entitled “Elastic properties of sands, Part 1: Micro computed tomography image analysis of grain shapes and their relationship with microstructure”. This chapter describes the micro-CT image acquisition and comprehensive image processing steps of four quartz sand samples prepared with different grain shapes and sorting indices. It also has a computer code that calculates a couple of micro-structural parameters of the granular pack. Further, a detailed investigation of the relationships among the calculated micro-structural parameters and the shape factors of the grains is presented based on the data from all four samples.

Chapter 3 has been submitted to *Geophysical Prospecting* as Part 2, with the title “Elastic properties of sands, Part 2: Implementation of contact-based model to determine the elasticity of the grains”. This chapter describes the experiment setup with loading–unloading procedure to measure the ultrasonic velcoties and volumetric changes resulting from successive stresses in the four quartz sand samples described in Chapter 2. This is followed by a description of the contact-based models together with the approach to utilising one of the models for calcualting the elastic moduli of the constituent grains. After that, the experiement results and calculations are described, including well-defined graphs. All the calcualtions are warranted by the necessary analysis considering the potential factors that could have an impact on the results.

Chapter 4 is going to be submitted to *Exploration Geophysics* with the title “Elastic properties of hard rock core sample calculated from the ultrasonic velocities of its powder collected during drilling”. This chapter examines three rock powder samples together with their corresponding solid cores that are collected during drilling in hard rock mineral exploration. These rock powders are composed of multiple minerals unlike the quartz sand sample described in Chapter 3. Therefore, a modification of an existing model is presented to calculate the effective elastic properties of the composite mineral. The outputs from this model are then fed into the prototype and then the

procedures in Chapter 3 are followed to calculate the elastic properties of the corresponding core sample.

Chapter 5 includes a conclusion that summarises all the outcomes from this study. This is followed by recommendations for potential approaches that could be implemented to advance this study further.

1.5. List of publications

The following first list contains the titles of the papers submitted and published in well-reputed, peer-reviewed journals. The second list has the extended abstracts accepted for oral and poster presentations in international conferences.

1.5.1. Journal publications

- Ahmed, Z. & Lebedev, M. 2018b. Elastic properties of sands, Part 1: Micro computed tomography image analysis of grain shapes and their relationship with microstructure. *Geophysical Prospecting.* https://doi.org/10.1111/1365-2478.12652.
- Ahmed, Z. & Lebedev, M. 2018c. Elastic properties of sands, Part 2: Implementation of contact-based model to determine the elasticity of the grains from ultrasonic measurement. *Geophysical Prospecting*. (accepted 08/01/2019)
- Ahmed, Z., Lebedev, M., Uvarova, Y. and Urosevic, M. Elastic properties of hard rock core sample calculated from the ultrasonic velocities of its powder collected during drilling. *Exploration Geophysics.* (Intended submission on April, 2019)

1.5.2. Conference publications

- Ahmed, Z. & Lebedev, M. 2018a, Optimum image resolution of a micro-CT image to characterise shape descriptors of unconsolidated sand. *First Australasian Exploration Geoscience Conference*, 18–21 February 2018, Sydney, Australia.

- Ahmed, Z. & Lebedev, M. 2017. Elastic parameters of the grain inverted from ultrasonic measurement of unconsolidated sands. *EAGE Workshop on Seismic Inversion for Reservoir Characterisation*, 16–17 November, 2017, Perth, Australia.
- Ahmed, Z. & Lebedev, M. 2017. Ultrasonic Velocities of unconsolidated Sand: Evaluating the Microstructure and Contact based Models. *Fouth EAGE Workshop on Rock Physics*, 11–13 November, 2017, Abu Dhabi, UAE.
- Ahmed, Z., Lebedev, M. & Madadi, M. 2017. Effect of grain shapes on coordination number from micro-CT image analysis of an unconsolidated sand. *79th EAGE Conference and Exhibition,* Paris, France.
- Ahmed, Z., Lebedev, M., Madadi, M. & Uvarova, Y. 2016. Inverting Dynamic Elastic Moduli of a Granular Pack to Get Shear Modulus of the Grain. *ASEG-PESA-AIG 2016, 25th Geophysical Conference and Exhibition*, pp. 944–948.

1.6. References for Chapter 1

Andrä, H., Combaret, N., Dvorkin, J., Glatt, E., Han, J., Kabel, M., Keehm, Y., Krzikalla, F., Lee, M., Madonna, C., Marsh, M., Mukerji, T., Saenger, E.H., Sain, R., Saxena, N., Ricker, S., Wiegmann, A. & Zhan, X. 2013a. Digital rock physics benchmarks—Part I: Imaging and segmentation. *Computers & Geosciences* **50**, 25-32.

Andrä, H., Combaret, N., Dvorkin, J., Glatt, E., Han, J., Kabel, M., Keehm, Y., Krzikalla, F., Lee, M., Madonna, C., Marsh, M., Mukerji, T., Saenger, E.H., Sain, R., Saxena, N., Ricker, S., Wiegmann, A. & Zhan, X. 2013b. Digital rock physics benchmarks—part II: Computing effective properties. *Computers & Geosciences* **50**, 33-43.

Arns, C.H., Knackstedt, M.A., Pinczewski, W.V. & Garboczi, E.J. 2002. Computation of linear elastic properties from microtomographic images: Methodology and agreement between theory and experiment. *Geophysics* **67**, 1396-1405.

Athanassiadis, A.G., La Riviere, P.J., Sidky, E., Pelizzari, C., Pan, X. & Jaeger, H.M. 2014. X-ray tomography system to investigate granular materials during mechanical loading. *Rev Sci Instrum* **85**, 083708.

Berg, C.F., Lopez, O. & Berland, H. 2017. Industrial applications of digital rock technology. *Journal of Petroleum Science and Engineering* **157**, 131-147.

Birch, F. 1960. The velocity of compressional waves in rocks to 10- kilobars: Part 1. *Journal of Geophysical Research* **65**, 1083–1102.

Bultreys, T., Boone, M.A., Boone, M.N., De Schryver, T., Masschaele, B., Van Hoorebeke, L. & Cnudde, V. 2016. Fast laboratory-based micro-computed tomography for pore-scale research: Illustrative experiments and perspectives on the future. *Advances in Water Resources* **95**, 341-351.

Christensen, N.I. 1965. Compressional wave velocities in metamorphic rocks at pressures to 10 kilobars. *Journal of Geophysical Research* **70**, 6147-6164.

Cnudde, V. & Boone, M.N. 2013. High-resolution X-ray computed tomography in geosciences: A review of the current technology and applications. *Earth-Science Reviews* **123**, 1-17.

Dvorkin, J., Derzhi, N., Diazan, E. & Fang, Q. 2011. Relevance of computational rock physics. *Geophysics* **76**, E141-E153.

Fawad, M., Mondol, N.H., Jahren, J. & Bjørlykke, K. 2011. Mechanical compaction and ultrasonic velocity of sands with different texture and mineralogical composition. *Geophysical Prospecting* **59**, 697-720.

Garboczi, E.J. & Day, A.R. 1995. An algorithm for computing the effective linear elastic properties of heterogeneous materials- three-dimensional results for composites with equal phase poisson ratios. *J. Mech. Phys. Solids* **43**, 1349-1362.

Iovea, M., Oaie, G., Ricman, C., Mateiasi, G., Neagu, M., Szobotka, S. & Duliu, O.G. 2009. Dual-energy X-ray computer axial tomography and digital radiography investigation of cores and other objects of geological interest. *Engineering Geology* **103**, 119-126.

Madonna, C., Almqvist, B.S.G. & Saenger, E.H. 2012. Digital rock physics: numerical prediction of pressure-dependent ultrasonic velocities using micro-CT imaging. *Geophysical Journal International* **189**, 1475-1482.

Madonna, C., Quintal, B., Frehner, M., Almqvist, B.S.G., Tisato, N., Pistone, M., Marone, F. & Saenger, E.H. 2013. Synchrotron-based X-ray tomographic microscopy for rock physics investigations. *Geophysics* **78**, D53-D64.

Maire, E. & Withers, P.J. 2014. Quantitative X-ray tomography. *International Materials Reviews* **59**, 1-43.

Marion, D.P. 1990. Acoustical, mechanical and transport properties of sediments and granular materials. Vol. PhD. Stanford University.

Mees, F., Swennen, R., Geet, M.V. & Jacobs, P. 2003. Applications of X-ray computed tomography in the geosciences **Geological Society, London, Special Publications**, 1-6.

Moreno-Atanasio, R., Williams, R.A. & Jia, X. 2010. Combining X-ray microtomography with computer simulation for analysis of granular and porous materials. *Particuology* **8**, 81-99.

Prasad, M. & Manghnani, M.H. 1997. Effects of pore and differential pressure on compressional wave velocity and quality factor in Berea and Michigan sandstones. *Geophysics* **62**, 1163-1176.

Saenger, E.H., Krüger, O.S. & Shapiro, S.A. 2004. Numerical considerations of fluid effects on wave propagation: Influence of the tortuosity. *Geophysical Research Letters* **31**, n/a-n/a.

Schindler, M., Batzle, M.L. & Prasad, M. 2017. Micro X-Ray computed tomography imaging and ultrasonic velocity measurements in tetrahydrofuran-hydrate-bearing sediments. *Geophysical Prospecting* **65**, 1025-1036.

Shulakova, V., Pervukhina, M., Müller, T.M., Lebedev, M., Mayo, S., Schmid, S., Golodoniuc, P., De Paula, O.B., Clennell, M.B. & Gurevich, B. 2013. Computational elastic up-scaling of sandstone on the basis of X-ray micro-tomographic images. *Geophysical Prospecting* **61**, 287-301.

Stock, S.R. 2009. *MicroComputed Tomography Methodology and Applications.* CRC Press, Taylor & Francis Group, ISBN ISBN 978-1-4200-5876-5.

Stock, S.R. 2013. Recent advances in X-ray microtomography applied to materials. *International Materials Reviews* **53**, 129-181.

Timur, A. 1977. Temperature Dependence Of Compressional And Shear Wave Velocities In Rocks. *Geophysics* **42**, 950-956.

Zimmer, M.A. 2003. Seismic velocities in unconsolidated sands: measurements of pressure, sorting, and compaction effects. In: *Department of Geophysics*, Vol. PhD thesis. Stanford University.

2. Elastic properties of sands, Part-1: Micro computed tomography image analysis of grain shapes and their relationship with microstructure.[1]

2.1. Abstract

Elastic properties of an unconsolidated sand are largely dependent on the elastic properties of its constituent grain and the microstructure that defines how the grains are arranged within themselves. Coordination number, i.e. the average number of contacts a grain has with its neighbours, and contact surface area are the two parameters closely related to the microstructure. Moreover, grain shapes and sorting also have substantial influence on these parameters. To calculate these parameters and find any potential relationships with the shape factors, we acquire high resolution micro-CT images of four mechanically compacted unconsolidated dry sand samples which are of different shape factors and sorting indices. After a comprehensive voxel based data processing, we calculate shape factors such as sphericity and roundness of each grain in all samples. Using own algorithm, we then calculate the coordination number and contact surface area. Results show that samples of well sorted and higher spherical and rounded grains have higher coordination number and contact surface area than the samples of poorly sorted and lower spherical and rounded grains. Among the poorly sorted samples, coordination number is largely dependent on the fraction of larger grain sizes present in the sample. Inside any given sample, grains of lower sphericity tend to have higher coordination numbers. Moreover, more spherical and rounded grains have greater contact surface area with their neighbours.

---

[1] This Chapter is an extended version of the paper published at *Geophysical Prospecting (https://doi.org/10.1111/1365-2478.12652)*

2.2. Introduction

Study of granular materials has a wide range of applications due to its relevance to various disciplines such as powder technology in food, the pharmaceutical and agricultural industries, and construction engineering for road and railway pavements. It is crucially important in near surface geophysics to predict elastic properties of unconsolidated reservoirs. The mechanical properties of granular material are largely controlled by the coordination number (C); i.e., the average number of contacts a grain has with its neighbours (Agnolin and Roux 2008, Oda 1972, Zimmer 2003, Ahmed and Lebedev 2017). The size, shape and angularity of the grains also have similar importance in determining the effective mechanical properties of such granular media (Cavarretta 2009, Dondi et al. 2012, Ha Giang et al. 2015, Santamarina and Cho 2004).

A number of studies emerge from the literature that calculate C using different approaches. Graton and Fraser (1935) calculated C ranging from 6 to 12 for different systematic geometric arrangements of identical spheres. Smith et al. (1929) literally counted the number of contacts using steel balls poured into acid that left marks of the contacts. Murphy (1982) has a compilation of C s as a function of porosity from theoretical, computer simulation and experimental observations by different authors. A number of authors obtained C s from numerical simulation of monodisperse (Sain 2010, Silbert et al. 2002), bimodal (Makse et al. 2004, Sain 2010) and polydisperse (Garcia and Medina 2006, Sain 2010) spherical grains. Dutta et al. (2010) inverted ultrasonic velocity data of an unconsolidated sand using contact-based models to get separate C s for P- and S-wave velocities as functions of porosity and pressure, and implemented their findings to predict the velocities of another unconsolidated sand sample.

With the advancement of image acquisition technology (Wildenschild and Sheppard 2013), 3D micro-CT images are providing great insight into the microstructure of the granular material as well as the morphology of the constituent grains. Analysis of 3D images from micro-CT has become a very useful tool in geoscience applications in recent years (Moreno-Atanasio et al. 2010). Using radial distribution of the neighbours of a particular grain, Seidler et al. (2000) and Aste et al. (2005) implemented micro-CT images to obtain Cs of monodisperse glass bead samples. Hasan and Alshibli (2010) calculated the relationship between void ratio and C from CT images using the codes

from Thompson et al. (2006). Al-Raoush (2007) and Druckrey et al. (2016) developed computer codes for 3D image analysis to obtain C from the voxels that are in contact between the grains. Ahmed et al. (2017) used micro-CT images of an unconsolidated sand to calculate C and grain-shape characteristics of a well-sorted and rounded unconsolidated sand.

Up until now, grain shape quantification by fractal dimension (Arasan et al. 2011), SEM image analysis (Cox and Budhu 2008) and shape effect on mechanical behaviour (Chaze and Cambou 2014, Ham et al. 2012, Liu et al. 2015) have mostly been based on 2D images. Some studies have used 3D tomography images to calculate grain morphology (Alshibli et al. 2015, Druckrey et al. 2016, Lin and Miller 2005) as well as grain size distribution (Gualda and Rivers 2006). Comparing results obtained from 2D and 3D image analysis, calculated shape factors are more accurate when using 3D image data (Alshibli et al. 2015, Fonseca et al. 2012) as the projection planes cannot represent the actual shape of the object in a 2D image.

Porosity, grain morphology and C are all inter-related. There are several studies (e.g., Murphy 1982) that link porosity with C but there is also evidence that the same porosity and pressure range can have different Cs (Duffaut et al. 2010). Questions are also raised as to why Cs obtained from numerical simulations are lower than those obtained from the corresponding experimental data (Dutta et al. 2010). On the other hand, comparison of Cs between 3D images of natural sand and numerical simulation of spherical grains with the same porosity shows that the C is affected by the grain shapes (Al-Raoush 2007). The effect of the sorting index in C is also evident from numerical simulations (Sain 2010).

However, implementing such 3D imaging techniques to estimate effective elastic properties of granular media requires detailed knowledge of the C for a particular granular sample. In this chapter we report on a detailed investigation of C and grain morphology for real sands. We use these results in the next chapter to invert the results of ultrasonic experiments performed on the same samples in order to obtain the elastic properties of individual grains based on a contact-based model. We also link contact surface area with grain morphology.

This chapter is structured as follows: first we describe sample preparation and 3D image acquisition, followed by outlining the processing steps of those acquired images. We then describe the procedure of calculating C and contact surface areas. We also report key parameters, which must be considered in image processing and analysis. We then present the results and describe potential relationships between grain shape characteristics and microstructural properties. Finally, we present in Appendix 2.A a computer code that has been used for calculating coordination number and contact surface area from the micro-CT images. In Appendix 2.B, we give a review on the correlation coefficients that are used in quantifying potential relationships among grain morphology and micro-structure.

2.3. Sample preparation and image acquisition

We prepare the samples from Esperance Beach sand (33°59′40″S 122°13′57″E) that is composed totally of quartz grains. The original sand is very well sorted, with sizes within the range of 106 to 256 μm. We pulverize the sand manually and sieve it to two finer size groups ranging from 56 to 256 μm. The collision of the grains during pulverization makes the grain shapes different to the original intact sand as well. Finally, we mix sand fractions with different weight proportions to make four samples (Table 2.1).

Table 2.1: Weight grain size distribution and information on acquired images of sample.

Sample name	Grain size (Weight percent)			Image Resolution, μm/voxel edge	Number of slices	Number of grains studied
	36–56 μm	56–106 μm	106–256 μm			
S-0	0	0	100%	0.9814	998	61
				2.2899	991	1090
S-1	0	30%	70%	1.7174	989	878
S-2	0	70%	30%	1.7174	991	1609
S-3	0	50%	50%	0.9814	990	289
				1.7174	991	1553

We put the sand samples in a cylindrical oedometric chamber with a diameter of 38.5 mm. Then we close the chamber with two cylindrical pistons made from PEEK plastics that are used to apply axial stress to the sample. After putting the set up vertically, we attach a pair of transducers to the pistons and measure ultrasonic travel times at different vertical stresses. A detailed description of the ultrasonic measurement procedure is described in the next chapter. After two loading-unloading cycles in which axial stress does not exceed 2.52 MPa, the samples are subjected to axial loading up to 12.6 MPa. Ultrasonic measurement is performed during the last loading phase. Using similar samples, setup and apparatus, Ahmed et al. (2016) demonstrated that during unloading after a preceding loading phase, sample length does not recover its previous length. In that context, we can infer that slowly removing the top piston does not significantly change grain arrangement. Moreover, the couple of loading-unloading cycles in the beginning can settle the grains beforehand. After ultrasonic measurement, we carefully remove one of the pistons and pour low viscosity epoxy resin slowly inside the chamber to solidify the sample. The solidified part of the sample is then cut to a 5mm long cylinder with a 4mm diameter and polished to be ready for image acquisition.

Micro-CT images (Figure 2.1) are acquired by 3D X-ray microscope VersaXRM-500 (XRadia-Zeiss) (Figure 2.2) at X-ray energy of 80kV at three different resolutions. Table 1 listed the image resolutions, number of slices acquired after image reconstruction for each sample, and number of individual grains studied.

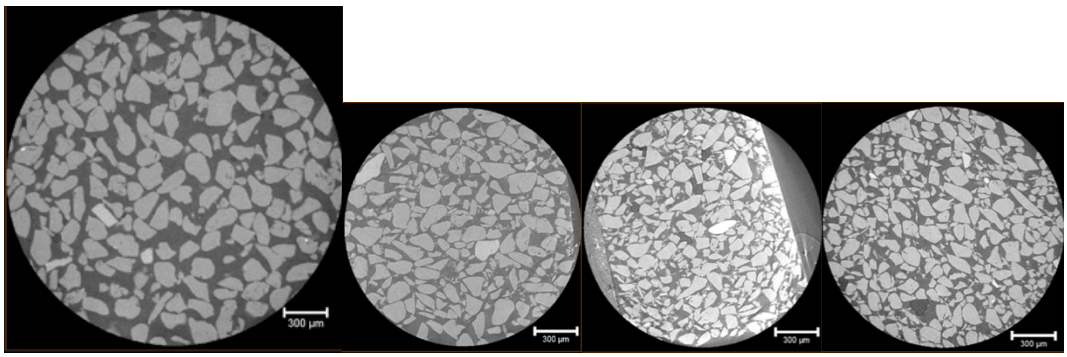

Figure 2.1: Slices of micro-CT images of S-0, S-1, S-2, and S-3 (from left to right).

Figure 2.2: X-Radia-Zeiss Versa XRM500 which is used to acquire micro-CT images of the samples.

2.4. Image processing

2.4.1. Grain size and shape attributes

Grain shapes in geoscience are mostly interpreted using a qualitative approach described by Powers (1953) and using charts from Krumbein and Sloss (1963). Zavala (2012) has a thorough review on the grain shape indices that exist in the literature. The main attributes that we use in this study are equivalent diameter, sphericity and roundness of the grain.

For describing the size of a grain, we use equivalent diameter that is defined as the diameter of a sphere that has the same volume as the particular grain.

$$\boldsymbol{EqDiameter, EqD} = \sqrt[3]{\frac{6 \times \boldsymbol{Volume}}{\boldsymbol{\pi}}} \tag{1}$$

The sphericity of the grain is a measure that describes how "spherical" the grain is with respect to a perfect sphere. Wadell (1934) defined sphericity as the ratio between particle volume and the volume of a sphere that envelops the particle. In contrast, Alshibli et al. (2015) introduced sphericity as the ratio between the particle volume and

the volume of a sphere with the shortest diameter on three orthogonal axes passing through the centre of the mass. In our calculation, we use the following equation of sphericity (equation 2) used by Wadell (1932) which is described as "degree of true sphericity." It is the ratio of the surface area of a sphere that has equal volume of the grain to the surface area of the grain. The range of this sphericity lies between 0 and 1, where 1 corresponds to a perfect sphere.

$$Sphericity, Sph = \frac{\sqrt[3]{36 \times \pi \times Volume^2}}{Surface\ Area} \tag{2}$$

Roundness is considered as the lack of angularity. It describes how sharp or round the edges of the grains are. We calculate the roundness from the ratio between surface area of the grain to the surface area of a sphere produced from the maximum and minimum diameter of the grain in 3D space. Higher roundness value represents more rounded grains. This value can be more than 1 for the grains that have more surface area than the surface area of the sphere produced from the average diameter.

$$Roundness, Rnd = \frac{Surface\ Area}{4 \times \pi \times (\frac{Diameter\_Max + Diameter\_Min}{4})^2} \tag{3}$$

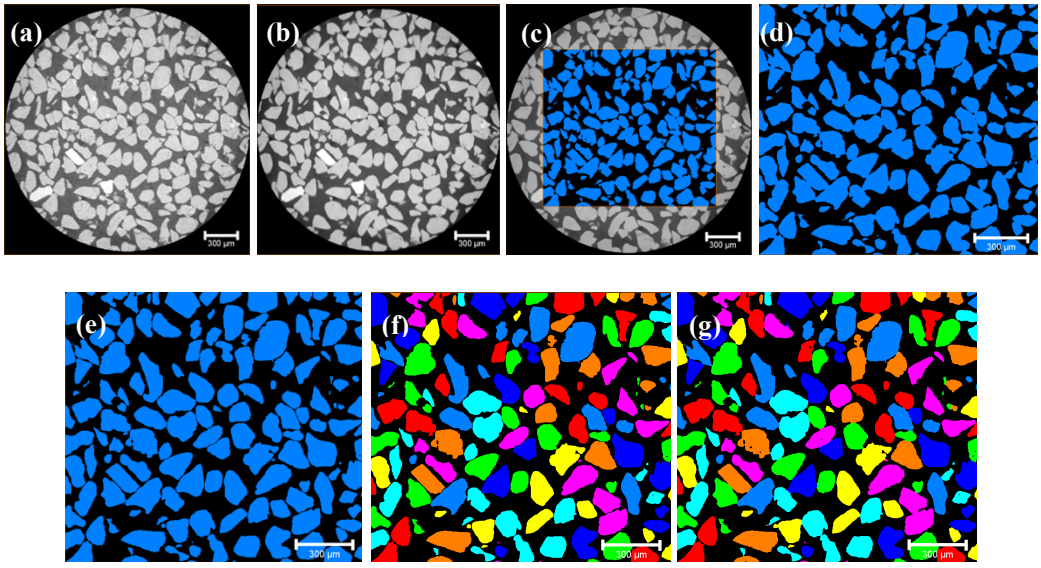

Figure 2.3: Processing steps (shown on a single slice). (a) Acquired image, (b) non-local means filter to remove noise, (c) interactive thresholding to separate the grains from background and select the region of interest (ROI), (d) fill holes to get rid of the voids inside the grain, (e) separate objects to remove the contacts between the grains,

(f) labelling to give individual grain a unique ID, and (g) contacts re-established to restore the original image with individual grain labels.

2.4.2. Processing steps

The advantages of micro-CT image analysis for a granular medium are enormous. We can visualise in detail and recognize each individual grain, and assign a unique identification number (ID) to it. This unique ID can be used to recall a particular grain to check by visualization for further clarification. We can also reproduce these procedures using different parameters to compare and get optimal results. Image processing steps and subsequent parameters can significantly affect the final results (Andrä et al. 2013). Therefore, it is essential to compare the results using different input parameters to get reliable results. We use a specialized micro-CT image processing software, Avizo 9.2, to process the image, calculate the shape factors and prepare the input image for calculating the C and contact surface area using Matlab.

Although the 3D acquired images of the sand samples in this study are very good quality, there are still so called "salt and pepper" noises to some extent (Figure 2.3(a)). To reduce these, we test using two different filters. The first one is a *3D Median filter* with 26 connectivity (6 face centre, 8 corner centre and 12 edge centre), around each centre voxel which takes the median value of all the assigned voxels and moves on. A median filter gives better results in images that contain non-Gaussian noises and very small artefacts. It also does not blur the image, instead keeping the edges sharp. The second one is a *Non-Local Means Filter* that is adapted from Buades et al. (2005). Instead of comparing the value of each voxel with every other voxel in the image, Avizo uses a search window to reduce the run time. Each voxel in the window is compared with its neighbours to get the similarity which gives a weight that influences the new value of the particular voxel being evaluated. Although a 3D Median Filter works better than a non-local means filter for the images with larger grain sizes (such as S-0), samples with smaller grains (S-1, S-2 and S-3) have some drawbacks. The boundaries of the smaller grains become blurrier, which makes them difficult to isolate from the background. On the other hand, a non-local means filter, although not as effective in removing the holes inside the grain, can retain the grain boundaries and remove the noise to output an acceptable noise-free image. To evaluate and compare the samples

on an even ground, we use a non-local means filter (Figure 2.3(b)) in all the samples. Comparison among the results from both of the filters show a slightly higher average C (Figure 2.4(a)), and lower sphericity (Figure 2.4(b)) and roundness (Figure 2.4(c)) values using a non-local means filter than those using a 3D median filter. This median filter assigns the boundary voxels the median values among the surrounding voxels and itself. After several iterations of using this filter, surface roughness becomes comparatively smoother. Thus surface smoothening causes very subtle contacts formed by angular edges of the grains to be lost. As non-local means filter better preserves the outline of the grains found in original image, we think coordination number calculated using this filter would be more accurate. For the shape characteristics, the filters provide very close values, thus we think any of these filters are appropriate for image processing of a well sorted and rounded samples such as S-0, which is well sorted and has more spherical and rounded grains of 106-256 μm in diameter. It should also be noted that image resolution or the size of the grains have significant influence in calculating shape characteristics.

(a)

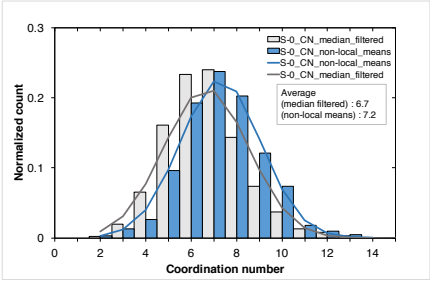

(b)

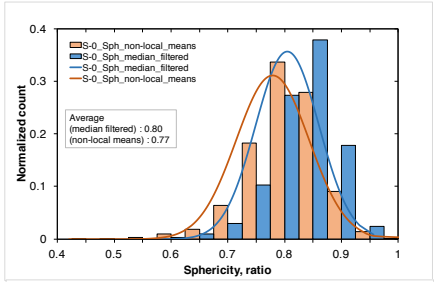

(c)

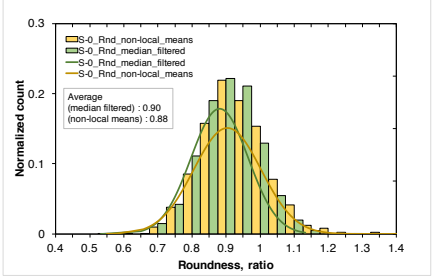

Figure 2.4: Comparing results from application of 3D median filter and non-local means filter in sample S-0. (a) C, (b) sphericity, and (c) roundness.

A robust review of different thresholding techniques that are required to isolate grains from their background is presented by Sezgin and Sankur (2004). Iassonov et al. (2009) also compare the results from using a number of thresholding techniques on different kind of samples. They concluded that methods from Otsu (1979) and Ridler and Calvard (1978) give an adequate result for the whole images whereas the indicator kriging method developed by Oh and Lindquist (1999) gives overall better results on their particular samples. We use a global thresholding technique called *Interactive thresholding* that uses a histogram of a grey label image to find the separation value. We use different ranges of thresholding values and check the results on random slices by comparing with the original image using interactive visualizations before finalizing one (Figure 2.3(c)).

We use the *Fill Holes* option in 3D with 26 connectivity to remove the holes that are enclosed inside the grain (Figure 2.3(d)). It works with complementing the image and applying geodesic dilation afterwards. The final image is complementing the image again to get the original image with holes "filled".

As soon as the images are thresholded – i.e. grains are separated from the background – they are ready to be segmented by removing the contacts between them. The *Separate object* module – a high-level combination of watershed, distance transform and numerical reconstruction – can effectively separate the grains that are in contact (Figure 2.3(e)).

After segmentation, grains are ready to be labelled. In *Labelling*, each grain gets its unique label (ID) or index ranging from 1 to the total number of grains. We label all the grains, including both full grains and partial grains that are cut by the border of the image. Figure 2.3(f) shows grains that are labelled individually shown in individual colours.

The *Label analysis* option gives the size and shape measurements for each grain. Inbuilt attributes such as *Equivalent Diameter*, *Area3D*, *3D length*, *3D width* and so on, as well as customized equations for sphericity and roundness, are put into this option.

Now we need to re-establish the grain contacts. To do that, we expand the grain boundary voxels in all directions with 26-connectivity to capture the contacts lost

during segmentation. Then we mask this image with the thresholded image to remove the unnecessary expanded portion, keeping the contacts of the grains intact.

Finally, we export this labelled and masked image file in ASCII format that contains all the grains (both full and partial) with their respective labels in each voxel. This ASCII image file then goes into Matlab code, which calculates the C and contact surface area of the full grains that are fully inside the image box and are not cut or touched by the image borders.

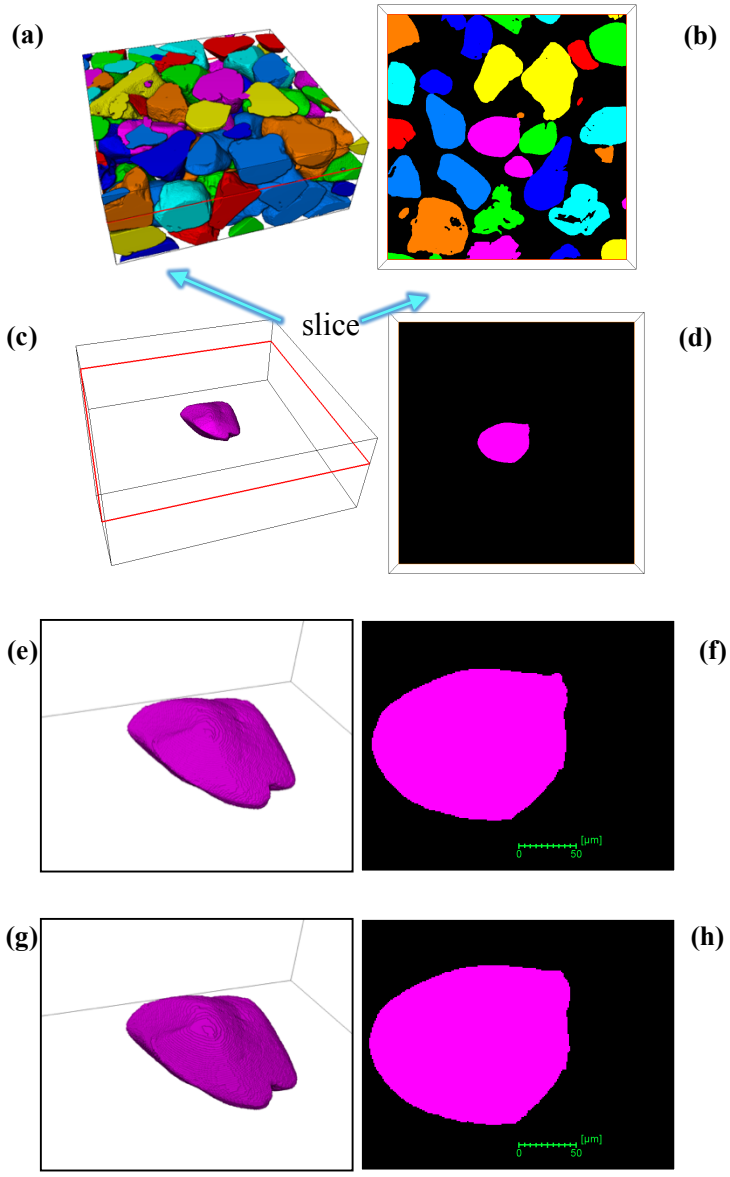

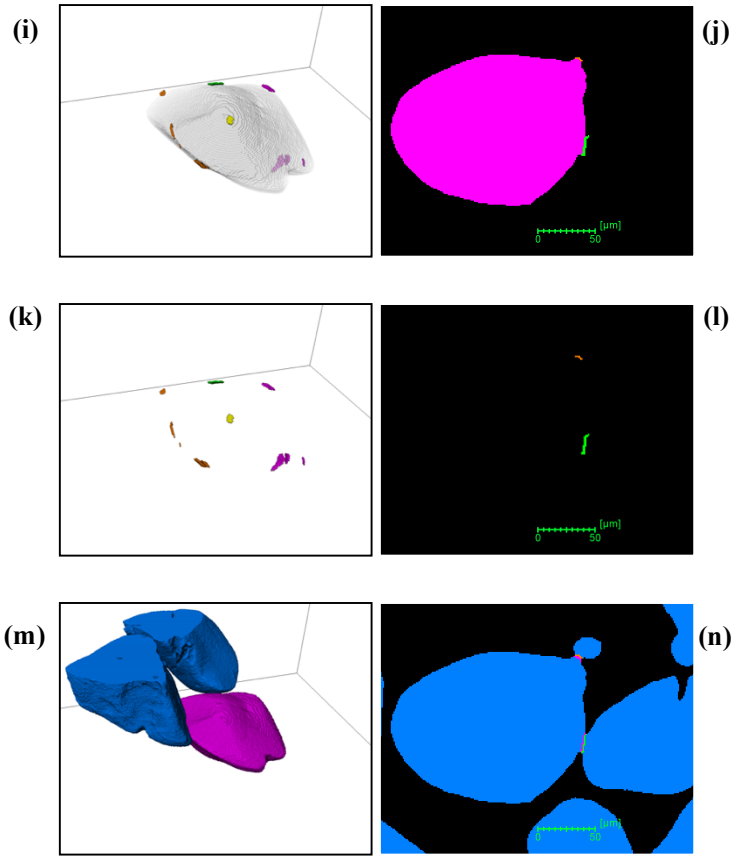

Figure 2.5: Graphical representation of the code to calculate C and contact surface area. (a) Convert the ASCII file into 3D image. (b) A slice from the 3D image where the position is marked as a red line. (c) Extraction of a single grain for which parameters are to be calculated. (d) Slice view Figure (c). (e) and (f) Zoomed view for better visualization of the previous two Figures (c) and (d) respectively. (g) Grain expanded on its boundary voxels. (h) Slice of Figure (g). (i) Contact voxels from the neighbouring grains with the target grain. (j) Slice of Figure (i). (k) Contact voxels from the neighbouring grains clearly shown without the target grain. (l) Slice of Figure (k). (m) Two of the grains that are in contact with the target grain. (n) Contact voxels of both of the grains that are shown in different colours in the slice.

2.5. Results

2.5.1. Coordination number and contact surface area calculations

We write a Matlab code to obtain C and contact surface area from the ASCII image file exported from Avizo 9.2. Figure 2.5 has the graphical representation of the code. The image volume has 259 slices of sample S-0. Figures of the left column show the 3D view and the right column is the 2D representation from a slice of the immediate left figure.

The exported ASCII file contains the voxel labels as corresponding grain labels that are arranged in one dimensional string. We convert this string of labels into a 3D matrix so that each voxel of the 3D image represents its corresponding coordinate position of that matrix. This conversion is actually recreating the image exported from the Avizo 9.2 (Figure 2.5(a)). Figure 2.5(b) shows a slice that is marked as a red line in the image box boundary in Figure 2.5(a). Each grain has own unique label from 1 to the total number of grains which are shown in different colours in the Figures 2.5(a) and (b). The void space in the image has the label 0 which is transparent and black in the images of the left and right columns respectively. For any particular full grain (that does not touch the image boundary) in which the parameters are to be calculated, we extract that one leaving other voxels 0 (Figures 2.5(c) and (d)). Figures 2.5(e) and (f) are just the zoomed representation of the immediate last two figures respectively to have a close view. Now to capture the voxels that have contacts with the boundary voxel of this grain, we expand each boundary voxel by one voxel in all directions with 26 connectivity (Figures 2.5(g) and (h)). Multiplication of this expanded grain with the original image results in a 3D matrix that contains the grain and the contact voxels from the neighbouring grains (Figures 2.5(i) and (j)). Thus, the number of unique labels (or IDs) except the label of that particular grain and 0 (void space) is the C for that particular grain (Figure 2.5(k) and (l)). The code also provides the grain labels that are in contact with any particular grain. This allows us to recheck the validity of the code after recalling the respective grain labels into Avizo and visualizing the contacts. Figure 2.5(m) shows two of the grains that are in contact. We can also see the contact voxels of both of the grains in Figure 2.5(n). To calculate the contact surface area, we extract only the contact voxels leaving all other voxels as 0 (e.g. Figure 2.5(k)). The number of contact voxels for a particular grain together with the image resolution gives the

contact surface area. The total contact surface is just a summation of the areas from all contacts. We have presented the Matlab code in the Appendix 2.A.

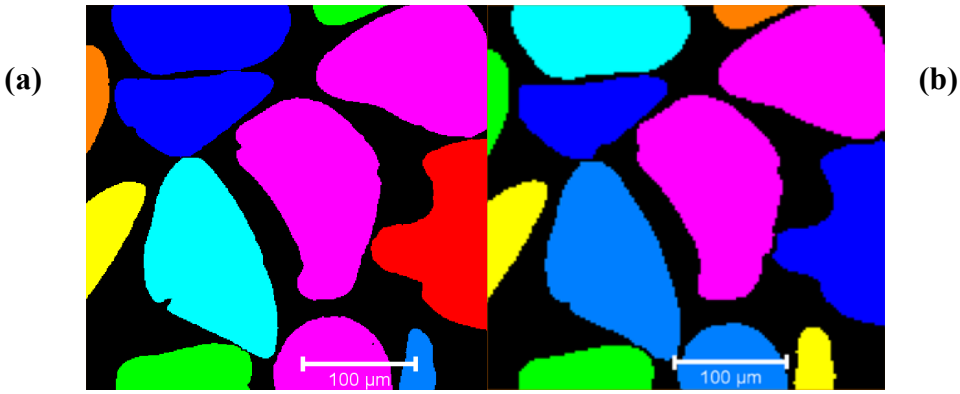

Figure 2.6: Labelled images of S-0 with a resolution of (a) (0.9814 µm)3/voxel and (b) (2.2899 µm)3/voxel

2.5.2. Impact of image resolution on the results

Image resolution has substantial influence on the calculated shape factors of the grains. Zeidan et al. (2007) found the calculated area (2D) or volume (3D) strongly depend on the system resolution: the higher the resolution, the better the accuracy. The accuracy is also dependent on the shape and size of the particle. Kröner and Doménech Carbó (2013) showed some comparison study on pixel resolution in defining shape characteristics such as elongation vs sphericity and roundness for 2D particles. In our case, although all three resolutions are quite high for the grain sizes that our samples are composed of, we examine how results obtained from images with different resolutions of (0.9814 µm)3/voxel and (2.2899 µm)3/voxel for S-0 (Figure 2.6), and (0.9814 µm)3 and (1.7174 µm)3/voxel for S-3 (Figure 2.8) differ from one another.

(a)

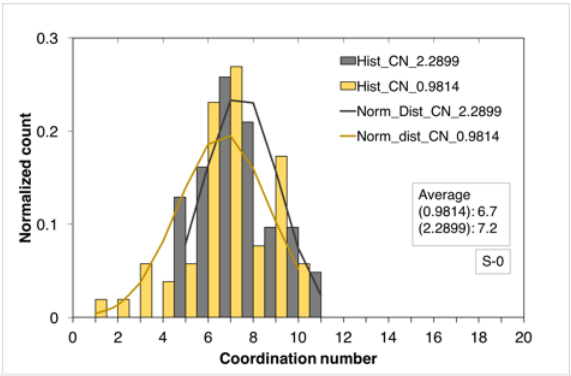

(b)

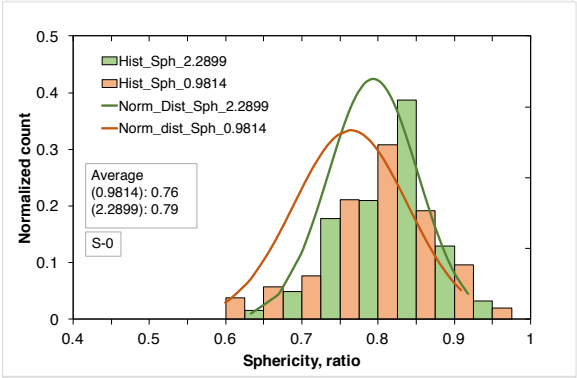

(c)

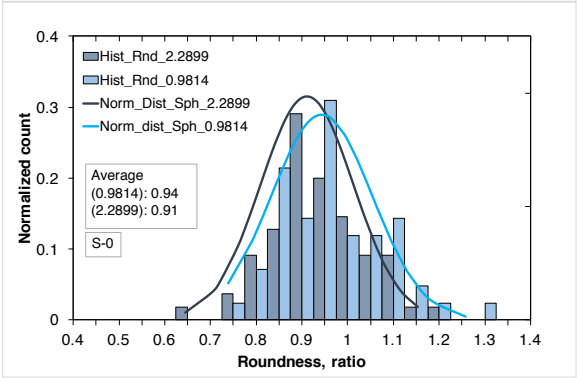

Figure 2.7: Comparing image resolutions on calculated (a) C, (b) sphericity, and (c) roundness in S-0. The bar diagram is for normalized count of the histogram and the solid lines are the bell curves for normal distribution.

(a)

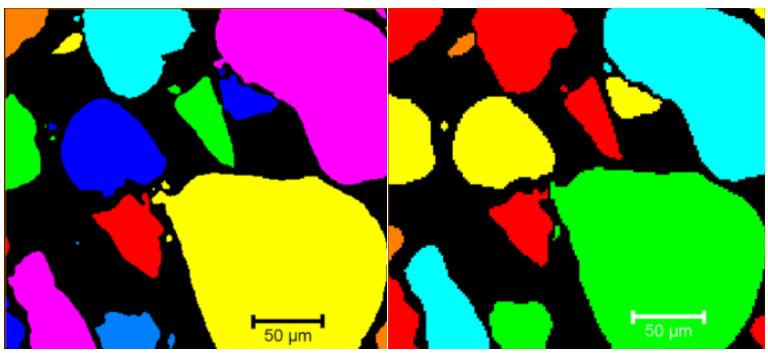

(b)

Figure 2.8: Labelled images of S-3 with a resolution of (a) (0.9814 µm)3/voxel and (b) (1.7174 µm)3/voxel

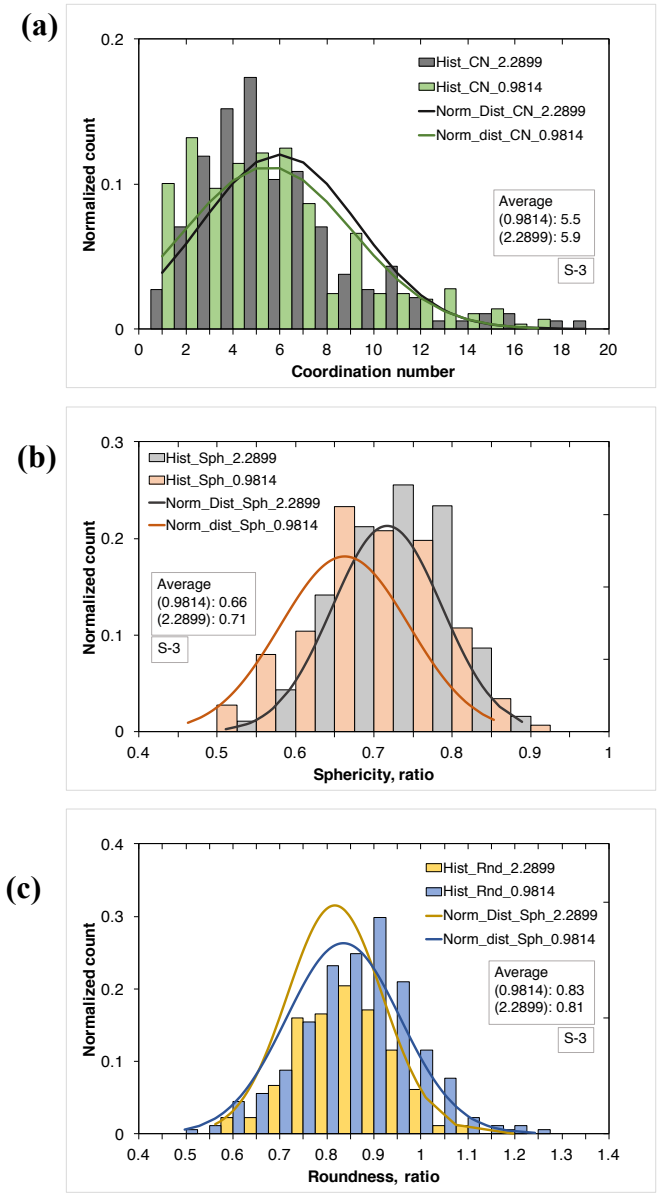

Figure 2.9: Comparison of the results of (a) C, (b) sphericity and (c) roundness using resolution of (0.9814 µm)3/voxel and (1.7174 µm)3/voxel in S-3. The bar diagram is the normalized count of the histogram and the solid lines are the normal distribution curves.

The C obtained from higher resolution images for both of the samples show slightly lower values (average C s are 6.7 and 5.5 for S-0 and S-3 respectively) than those of the lower counterparts (average C s are 7.2 and 5.9 for S-0 and S-3 respectively), which are shown in Figures 2.7(a) and 2.9(a). Moreover, resolution affects the number of boundary voxels used in calculating the surface area of the grains. This surface area is involved in sphericity and roundness equations (Eq.2 and 3), resulting in lower average

sphericity (0.76 and 0.66 for S-0 and S-3 respectively) in higher resolution image than those (0.76 and 0.71 in S-0 and S-3 respectively) of the lower resolution images (Figures 2.7(b) and 2.9(b)). On the other hand, a higher resolution image provides higher roundness values (0.94 and 0.83 in S-0 and S-3 respectively) than those (0.91 and 0.81 in S-0 and S-3 respectively) of the lower resolution images (Figures 2.7(c) and 2.9(c)).

2.5.3. Representative Elementary Volume (REV) analysis

We perform representative volume analysis to understand whether our region of interest (ROI) is representative of the whole sample image. We use sorting index, porosity, C and grain shape factors in REV analysis. Al-Raoush and Papadopoulos (2010) successively increased the diameter of the studied volume anchored in a fixed centre to compare minimum REV for porosity, coordination number, size distribution of the grains and local void ratio. Unlike them, we divide the whole image volume into two, almost-equal subvolume parts, namely Seg-1 and Seg-2. In the following sections we compare the results obtained from each subvolume.

2.5.3.1. Sorting index

Sorting index (SI) gives a quantification of how diverse the grain sizes are in a given sample. Different equations to calculate SI exist in the literature but most of them are effective in certain sorted samples. Along with a presentation of a sorting index based on standard deviation and environmental significance, Friedman (1962), conducted a review on the existing literature in defining sorting that resembles an approximation of standard deviation of the grain sizes. He found Trask (1932) had a satisfactory result in case of well to very well sorted sands whereas Inman (1952) got better results in moderate to poorly sorted sands.

Similar to Sain (2010), we calculate SI as a ratio between standard deviation and mean grain size. Lower SI values indicate well-sorted samples and vice versa. Table 2.2 shows calculated SIs for all sub volumes of each sample. S-0 is well sorted whereas the other three are poorly sorted. However, similar values of SI in both of the subvolumes in each sample suggest that any of the subvolumes could be representative for calculations of the SI.

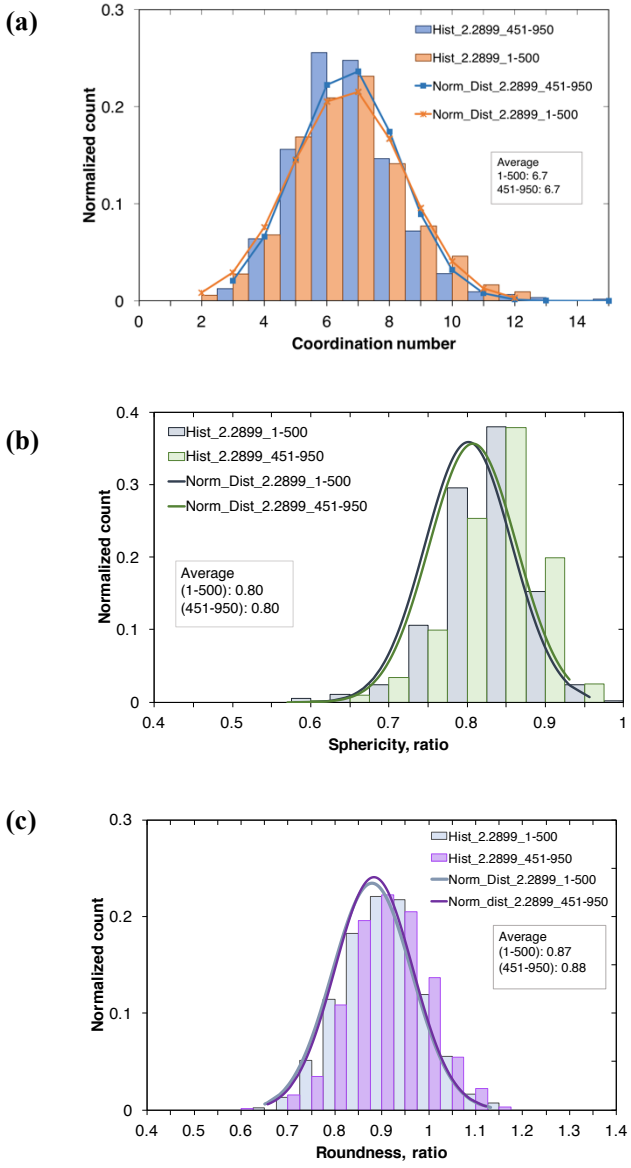

Figure 2.10: Representative Elementary Volume (REV) analysis in S-0 using two segments that consist of 1st to 500th slice and 451st to 950th slice respectively by calculating (a) C, (b) sphericity, and (c) roundness. The bar diagram is the normalized count of the histogram and the solid lines are the normal distribution curves.

2.5.3.2. Porosity, Coordination number and grain shape factors

Table 2.2 also includes porosity values calculated from the images of both of the segments in each sample. All of the porosities show close values from 42% to 44%. Both of the subvolumes show similar values, indicating the studied volume of the image is representative in terms of porosity. Results of C, sphericity and roundness show very

similar values from both of the sub volumes (Figure 2.10), which indicates that any of these segments can be representative for these properties.

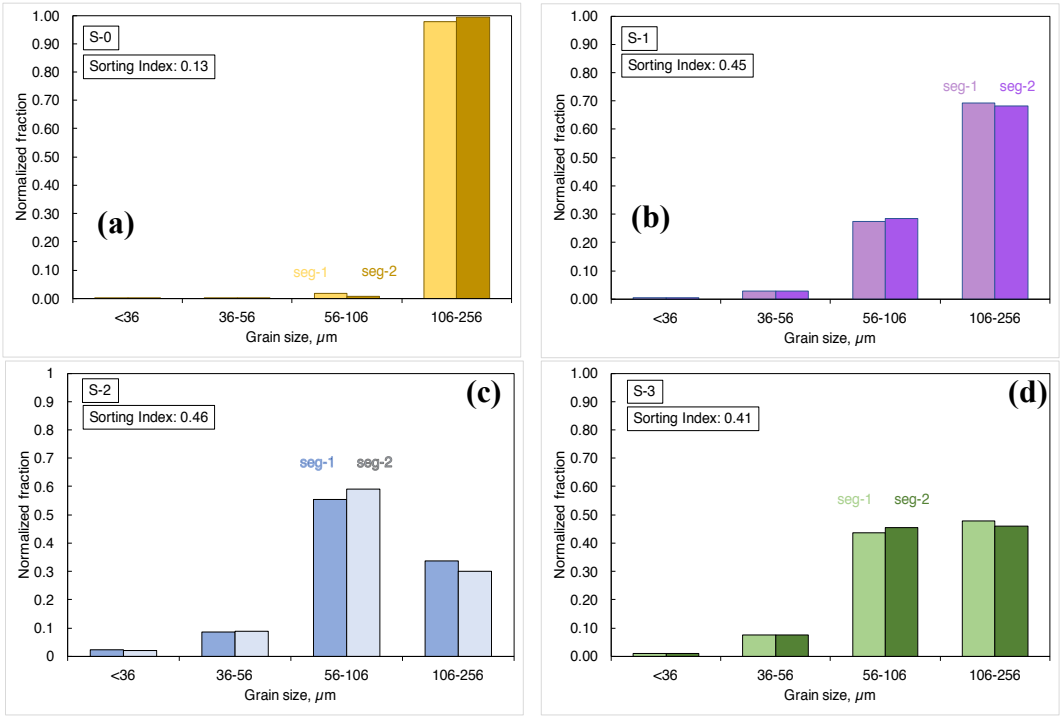

Figure 2.11: Grain size distribution by weight of the samples (a) S-0, (b) S-1, (c) S-2 and (d) S-3 obtained from micro-CT image analysis.

Table 2.2: Sorting index (SI) and Porosity of the segments of each sample.

Sample	Segment	Slices	Porosity	SI
S-0	Seg-1	38-500	0.44	0.13
	Seg-2	501-970	0.44	0.13
S-1	Seg-1	16-500	0.42	0.45
	Seg-2	501-975	0.42	0.46
S-2	Seg-1	16-500	0.45	0.46
	Seg-2	501-960	0.42	0.47
S-3	Seg-1	16-500	0.43	0.41
	Seg-2	501-975	0.43	0.43

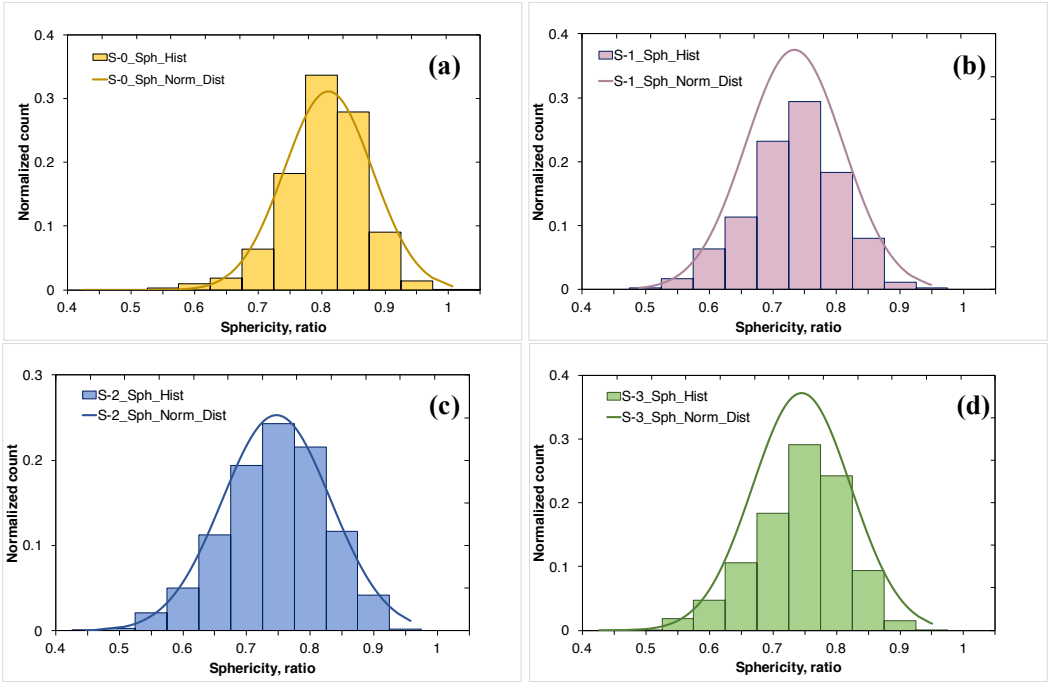

Figure 2.12: Distribution of the sphericity of the grains in samples (a) S-0, (b) S-1, (c) S-2 and (d) S-3. The bar diagram shows the normalized count of the histogram and the solid line is the normal distribution curves.

2.5.4. Grain shape characteristics

Grain size distribution by weight in S-0 calculated from the images shows similarities with the grain size distribution of the prepared sample after sieve analysis (Figure 2.11(a)). On the other hand, discrepancies exist in the other three samples where smaller grain fractions appear in the image results. From sieve analysis, grains of a 36–56 µm range are supposed to be absent but image analysis shows a presence of ~2% in S-1 and ~10% in each of S-2 and S-3. Grains smaller than 36 µm are also there but in very negligible weights (Figure 2.11(b), (c) and (d)). One potential reason for this might be the grains in these three samples were crushed during increasing loading stress in ultrasonic measurement. Grain size analysis from the images of S-0 taken before and after compaction up to 12.6 MPa show no evidence of grain crushing. In the other three samples, as the grains are less spherical and rounded (Figures 2.12, 2.13, 2.14 and 2.15), and sorting is poorer, the grains may be more prone to crushing. It is also well reported in the literature (e.g. Cox and Budhu 2008) that the grain size distributions from sieving and image analysis do not match as grains other than perfectly spherical and rounded shapes may not pass with its larger diameter through the sieve and tends to pass with

the smallest diameter. Moreover, our calculated equivalent diameter is based on the volume of the sample, thus no actual diameter is involved.

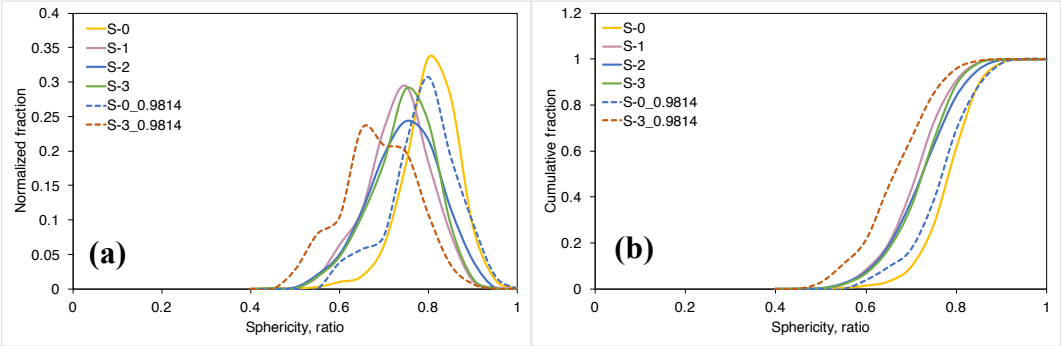

Figure 2.13: Sphericity of all four samples shown as (a) normalized count of histogram and (b) cumulative fraction. Solid lines of S-0 and the other three samples (S-1, S-2 and S-3) are from image resolution (2.2899 µm)3/voxel and (1.7174 µm)3/voxel respectively. Dashed lines are from image resolution (0.9814 µm)3/voxel of S-0 and S-3 for reference.

Grains in S-0 have greater sphericity compared with all other samples (S-1, S-2 and S-3) (Figure 2.12). As the former has a resolution of (2.2899 µm)3/voxel compared with the latter three samples of (1.7174 µm)3/voxel, and as resolution has an impact in grain shape calculation (Figures 2.7 and 2.9), we need to make a reference on the comparison that are evaluated on the same resolution. Sphericity in S-0 and S-3 from resolution (0.9814 µm)3/voxel shows a clear distinction in the grain shape as well (Figure 2.13(a)). Sphericity values in S-1, S-2 and S-3 show similar values (Figure 2.13(b)) as the grains are from the same pulverizing process.

Similar to sphericity, grains at S-0 show greater roundness than the other three samples, which share similar values (Figure 2.14). As the grains are fragmented during pulverizing, the edges of the crushed grains become more angular hence the roundness decreases. Using the same resolution images of S-0 and S-3, a histogram of roundness values shows discrepancy in peak values (Figure 2.15(a)). Figure 2.15(b) also shows a cumulative fraction of the roundness values in all the samples.

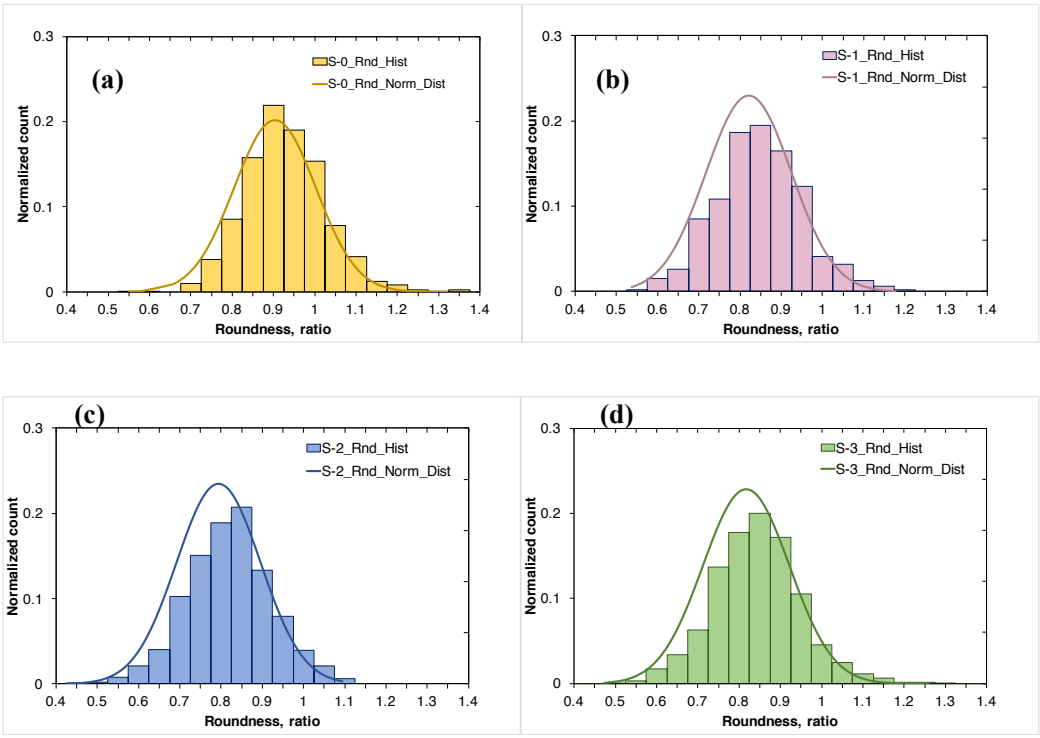

Figure 2.14: Distribution of the roundness of the grains in samples (a) S-0, (b) S-1, (c) S-2 and (d) S-3. The bar diagram shows the normalized count of the histogram and the solid line is a normal distribution curve.

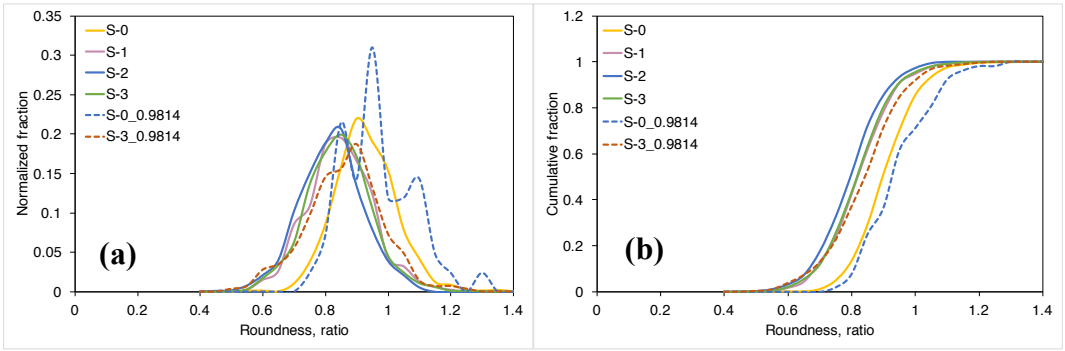

Figure 2.15: Roundness of the grains in all four samples shown as (a) a normalized count of the histogram and (b) a cumulative fraction. The solid lines of S-0 and the other three samples (S-1, S-2 and S-3) are from image resolution (2.2899 µm)3/voxel and (1.7174 µm)3/voxel respectively. The dashed lines are from image resolution (0.9814 µm)3/voxel of S-0 and S-3.

2.5.4.1. Coordination number dependence on size and shape characteristics

The calculated C in all four samples shows normal distribution (Figure 2.16). Figure 2.17(a) shows S-0 has the highest average C (7.2) whereas samples S-1, S-2 and S-3 have 6.7, 5.6 and 5.5 respectively. Using numerical simulations of poly-disperse packs of perfect spheres, Sain (2010) also found that Coordination number in well sorted samples is higher compared with the poorly sorted samples. We also present C s in S-0 and S-3 from their common resolution as a reference with dashed lines in Figure 2.17. The average C in the samples with different grain sizes depends largely on the proportion of larger grain size. S-1 shows a higher average C than both S-2 and S-3 in spite of having nearly the same sorting index. The reason is that S-1 has a higher proportion of larger grains (106-256 μm~70%), which accommodate more grains in contact around them than grains in the other two samples (Figure 2.17(b)). For a similar reason, in all the samples, the C of any particular grain increases with increasing grain diameter (Figure 2.18). On the other hand, Sain (2010) observed that C has a decreasing trend reached to a trough at nearly 85% of larger grain fraction from 0% larger grain fraction (well sorted) in a bi-disperse pack. It increases sharply from that trough to the 100 percent larger volume fraction at the same C value it had on 100% smaller grain fraction (well sorted). The depth of the trough increases with the increasing ratio between the radii of the grains in the bi-disperse pack. Comparison between these findings and our results from S-1, S-2 and S-3 is not plausible as all three samples have mostly trimodal size distribution (Figure 2.11). Moreover, unlike perfectly spheres, grains in these three samples have lower sphericity and roundness values. A sophisticated way to derive the actual trend of C with larger grain volume fraction is to use a number of samples prepared from different combination of those three sizes.

To find out any potential relationship between sphericity and C for any particular grain, we plot sphericity and equivalent diameter where we present C as colour bar (Figure 2.19). Apart from an obvious increasing trend of C with increasing grain size, we observe a subtle relationship between sphericity and C. For any given equivalent diameter, higher C s are accumulating at the bottom part of the grain population in the graph, which shows a diagonal zonation of the colours. This means a grain that has lower sphericity tends to have a higher C.

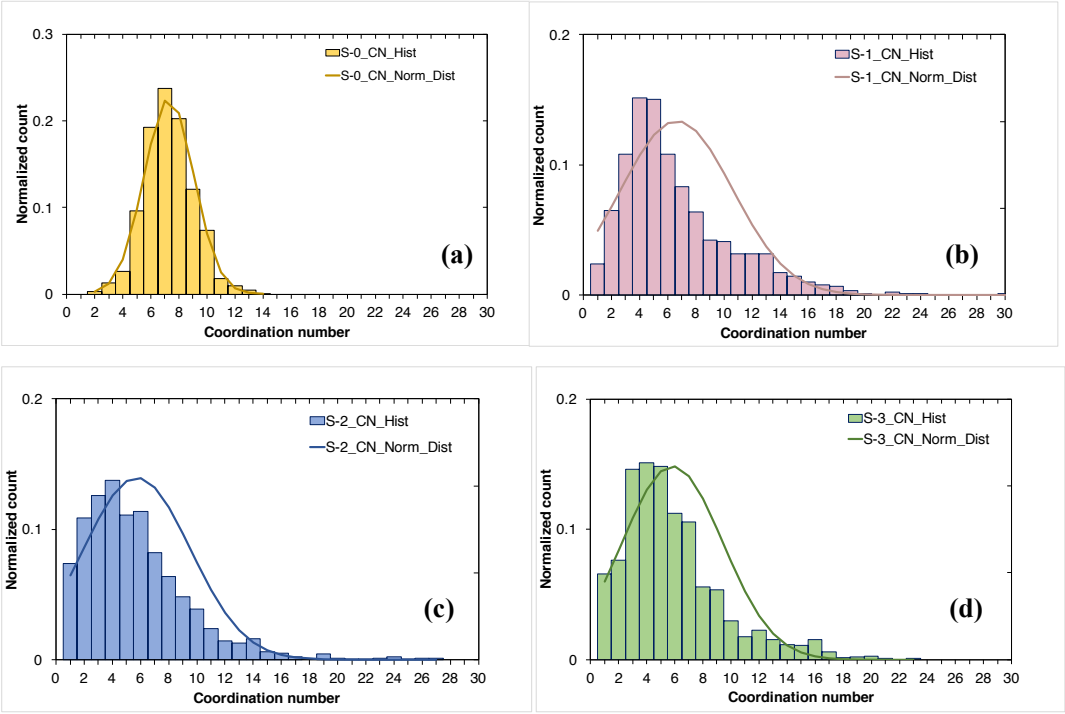

Figure 2.16: Distribution of C in samples (a) S-0, (b) S-1, (c) S-2 and (d) S-3. The bar diagram shows the normalized count of the histogram and the solid line is a normal distribution curve.

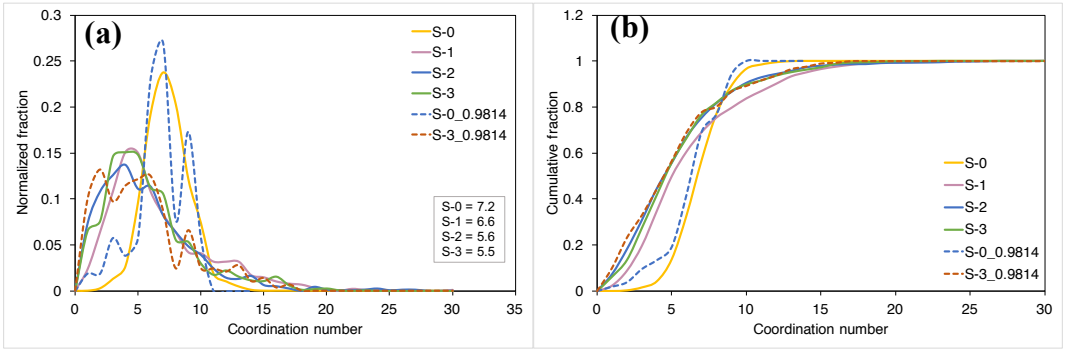

Figure 2.17: C in all four samples shown as (a) the normalized count of the histogram and (b) a cumulative fraction. Solid lines of S-0 and the other three samples (S-1, S-2 and S-3) are from image resolution (2.2899 µm)3/voxel and (1.7174 µm)3/voxel respectively. The dashed lines are from image resolution (0.9814 µm)3/voxel of S-0 and S-3.

Similar plots for roundness in samples S-1, S-2 and S-3 show that roundness increases with grain size. This is due to the sample preparation procedure. Different sizes are produced by a grain pulverization process and smaller fragments of the crushed grains

tend to be more angular than the larger ones. As with the relationship between C and sphericity, C and roundness merely show (Figure 2.20) similar relationship.

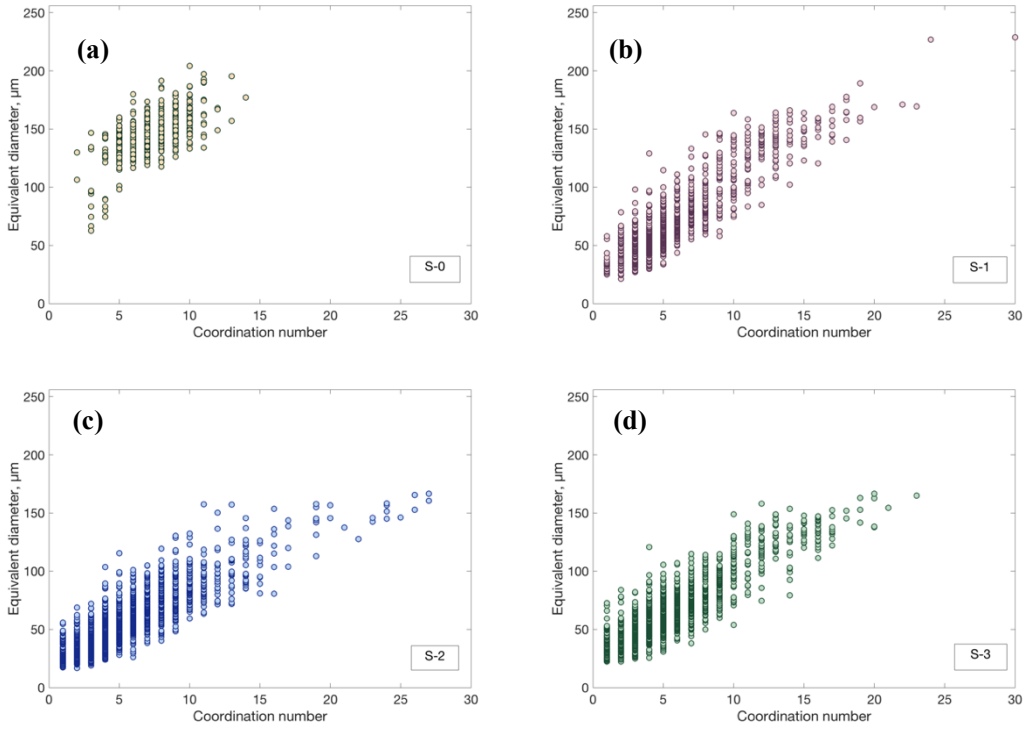

Figure 2.18: C plotted with equivalent diameter of the grains in samples (a) S-0, (b) S-1, (c) S-2 and (d) S-3.

Beside the visual analysis on the graph, we calculate Pearson linear correlation coefficient, r, to see how these parameters are related. This r value can be significantly biased by a third variable which might have a greater influence on one or both of the two variables. In fact, strong relationship is obvious between coordination number, C and equivalent diameter, EqD (Figure 2.18) for all four samples. Therefore, to get rid of any bias that can be caused by this relationship, we calculate partial correlation coefficients between the shape characteristics, C and EqD. Appendix B has a brief description on the derivation of the statistical analysis presented in this study.

We calculate zero order correlation (bivariate) between sphericity, coordination number and equivalent diameter with each other, ignoring the potential bias of the third variable (Table 2.3(a)). Size of the grains, EqD shows strong positive relationship with C in all the samples except S-0, which shows moderate r value of 0.55. The limited range of the grain size in this sample can be a reason for that. Corresponding P-values

in all the samples are much less than 0.05, which defines the statistical results on these coefficients are significant. Besides this, weak negative relationships are evident with very low P-values in sphericity, Sph and C in all the samples except S-1, where the P-values are also found large. Table 2.3(b) shows partial correlation coefficients of C and EqD in all the samples have little change compared with those from zero order correlation. This means the other variable, Sph has less impact on the relationship between C and EqD. On the other hand, C and Sph retain their negative relationship with some 5% changes that can be explained by the effect of EqD. All of these partial correlation coefficients have their corresponding P-values much less which make them statistically significant.

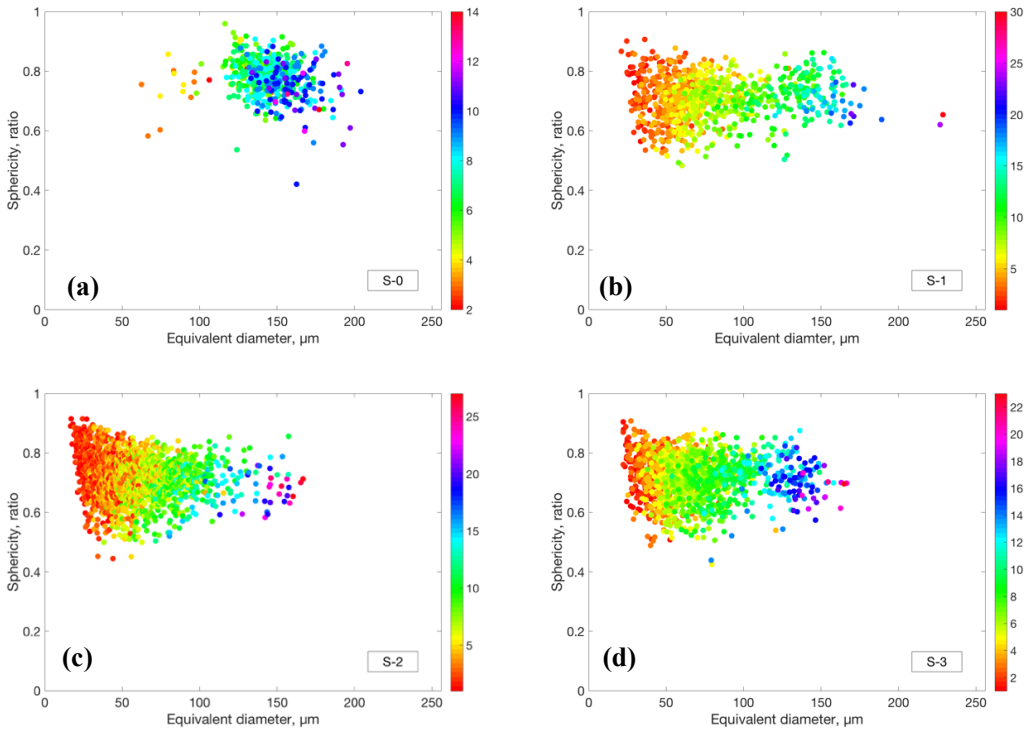

Figure 2.19: Equivalent diameter plotted with sphericity of the grains in samples (a) S-0, (b) S-1, (c) S-2 and (d) S-3, where colour represents the C.

At zero order correlation coefficient values (Table 2.4(a)), roundness, Rnd, shows moderate to weak positive relationship with C having much less corresponding P-values in all three samples of S-1, S-2 and S-3. Samples S-0 has almost all rounded grains and limited size range, hence the correlation appears negligible, which is also marred by the very high P-value, making the result insignificant. When we take the effect of EqD in partial correlation coefficients (Table 2.4(b)), r values become negative

but very low, among which sample S-1 and S-2 has higher P-value that make the relationship insignificant. This means relationship between C and Rnd is not as obvious as the negative correlation between C and Sph for any given angular and poorly sorted sample.

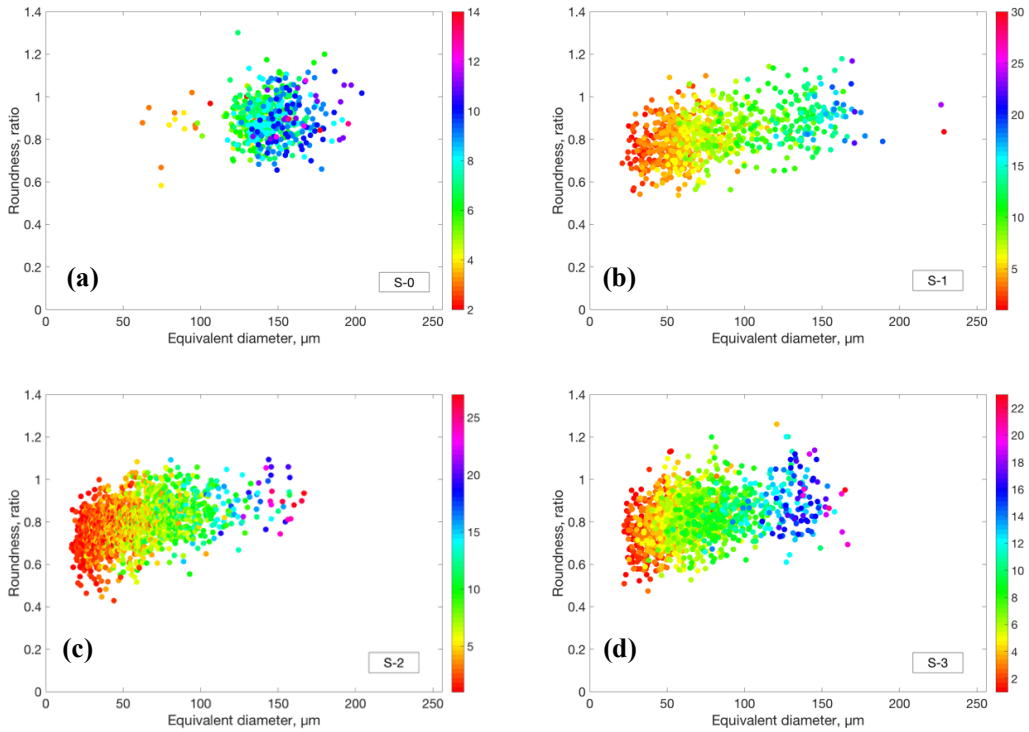

Figure 2.20: Equivalent diameter plotted with roundness of the grains in samples (a) S-0, (b) S-1, (c) S-2 and (d) S-3 where colour represents the C.

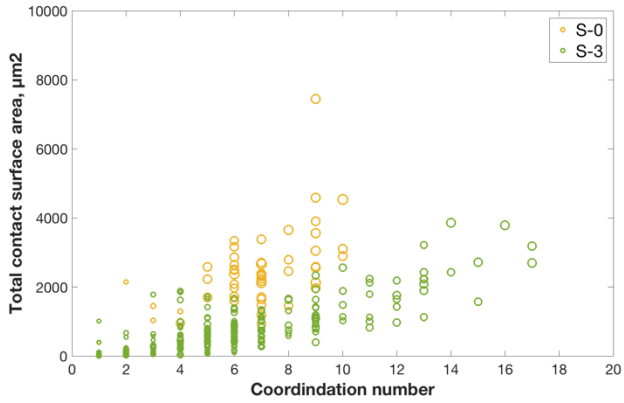

Figure 2.21: C with total contact surface area of samples S-0 and S-3 from the images with resolution of (0.9814 µm)3/voxel. The size of the marker indicates the equivalent diameter of the grains.

Table 2.3: Correlation coefficients and P-values for sphericity, coordination number and Equivalent diameter. (a) zero order correlation and (b) partial correlation.

(a)	S-0		S-1		S-2		S-3	
Zero order correlation	Sphericity (ratio)	Coordination Number	Sphericity (ratio)	Coordination Number	Sphericity (ratio)	Coordination Number	Sphericity (ratio)	Coordination Number
Coordination Number	-0.24	1	-0.05	1	-0.26	1	-0.12	1
P-value	<0.01	_	0.16	_	<0.01	_	<0.01	_
Equivalent Diameter(μm)	-0.16	0.56	0.07	0.90	-0.18	0.86	-0.05	0.88
P-value	<0.01	<0.01	0.05	<0.01	<0.01	0	0.04	0

(b)

	S-0		S-1		S-2		S-3	
Partial Correlation	Sphericity (ratio)	Coordination Number	Sphericity (ratio)	Coordination Number	Sphericity (ratio)	Coordination Number	Sphericity (ratio)	Coordination Number
Coordination Number	-0.18	1	-0.24	1	-0.21	1	-0.15	1
P-value	<0.01	_	<0.01	_	<0.01	_	<0.01	_
Equivalent Diameter(μm)	-0.04	0.54	0.25	0.90	0.09	0.85	0.11	0.88
P-value	0.20	<0.01	<0.01	<0.01	<0.01	0	<0.01	0

Table 2.4: Correlation coefficients and P-values for roundness, coordination number and Equivalent diameter. (a) zero order correlation and (b) partial correlation.

(a)	S-0		S-1		S-2		S-3	
Zero order correlation	Roundness (ratio)	Coordination Number	Roundness (ratio)	Coordination Number	Roundness (ratio)	Coordination Number	Roundness (ratio)	Coordination Number
Coordination Number	<0.01	1	0.39	1	0.35	1	0.29	1
P-value	0.95	_	<0.01	_	<0.01	_	<0.01	_
Equivalent Diameter(μm)	0.15	0.56	0.45	0.90	0.42	0.86	0.36	0.88
P-value	<0.01	<0.01	<0.01	<0.01	<0.01	0	<0.01	0

(b)	S-0		S-1		S-2		S-3	
Partial Correlation	Roundness (ratio)	Coordination Number	Roundness (ratio)	Coordination Number	Roundness (ratio)	Coordination Number	Roundness (ratio)	Coordination Number
Coordination Number	-0.10	1	-0.02	1	-0.03	1	-0.07	1
P-value	<0.01	_	0.56	_	0.17	_	<0.01	_
Equivalent Diameter(μm)	0.18	0.56	0.23	0.88	0.26	0.84	0.24	0.87
P-value	<0.01	<0.01	<0.01	<0.01	<0.01	0	<0.01	0

2.5.4.2. Contact surface area dependence on Coordination number, Grain size and Shape factors

Grains with more sphericity and roundness in S-0 tend to have more total contact surface area on a given C than grains with less sphericity and roundness in S-3 (Figure 2.21). This outcome also correlates with work by Viggiani et al. (2013) where they found that contact surface area decreases with increasing angularity of the grains in different samples. We also observe, as expected, that the total contact surface area increases with increasing grain size (Figure 2.21). For any given grain size, the total surface areas of these two samples are similar. However, grains of S-3 have more Cs, hence the average contact surface area is still less than grains in S-0. This fact is related to the grain roundness, as less rounded grains have less planar surface area to touch with other grains. In the grain-to-grain relationship inside any given sample, we do not observe any correlation between grain shape characteristics (sphericity and roundness in Figure 2.22(a) and 2.22(b) respectively) and total contact surface area for samples S-0 and S-3.

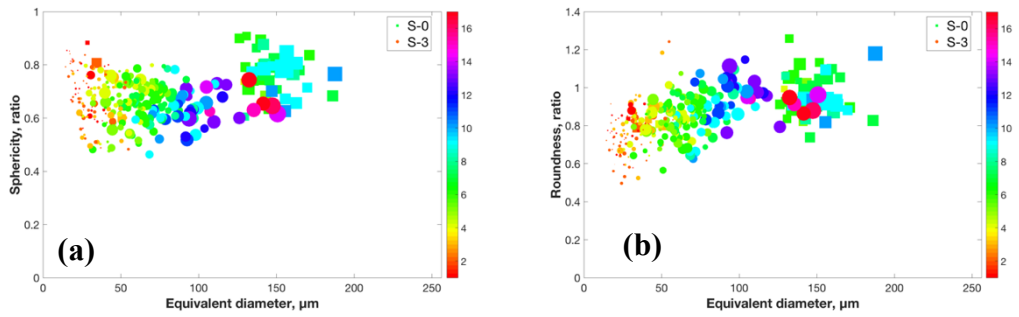

Figure 2.22: Equivalent diameter with (a) sphericity and (b) roundness of samples S-0 and S-3 from the images with resolution of (0.9814 µm)3/voxel. Marker size indicates total contact surface area and colour are for C. Circles represent grains from sample S-3 and squares are for S-0.

2.6. Conclusion

We have investigated in details relationships between the morphology of grains and coordination numbers (C) for real sand samples. We have found that the well-sorted, more spherical and more rounded sands have a higher C than the poorly sorted, less spherical and less rounded samples. We have also observed that the average C of a

poorly sorted sample is mainly controlled by the proportion of larger grains. On the other hand, samples with fewer spherical and rounded grains have lower average contact surface areas with their neighbours.

For a given sample, the C of an individual grain generally increases with its size. However, a relationship between the C with sphericity exists as well: less spherical grains tend to have more Cs. In case of roundness, similar relationship is merely observed in the plots.

C and contact surface area are the main factors that control the effective elastic properties of any granular material. As these two parameters can be affected by the grain size, shape and sorting, this study can be useful in modelling the effective elastic behaviour of different granular materials. In particular, we use the results presented in this paper to estimate the elastic properties of individual grains using ultrasonic measurement on sand pack under stress (Part-2, submitted in this issue).

2.7. Acknowledgements

This work has been supported by the Deep Exploration Technologies Cooperative Research Centre, whose activities are funded by the Australian Government's Cooperative Research Centre Programme. This is DET CRC document 2017/1060. The authors would like to thank the National Geosequestration Laboratory (NGL) for providing access to the X-ray microscope VersaXRM-500 (XRadia-Zeiss Ltd). This work was supported by resources provided by the Pawsey Supercomputing Centre with funding from the Australian Government and the Government of Western Australia. The authors also express their gratitude to ASEG Research Foundation for sponsoring them with Grant (RF16M04). ZA was supported by a Curtin International Postgraduate Research Scholarship and an Australian Government Research Training Program Scholarship.

2.8. References for Chapter 2

Agnolin, I. & Roux, J.N. 2008. On the elastic moduli of three-dimensional assemblies of spheres: Characterization and modeling of fluctuations in the particle

displacement and rotation. International Journal of Solids and Structures 45, 1101-1123.

Ahmed, Z. & Lebedev, M. 2017. Ultrasonic velocities of unconsolidated sand: Evaluating the microstructure and contact based models. In: 4th EAGE Workshop on Rock Physics, Abu Dhabi, United Arab Emirates.

Ahmed, Z., Lebedev, M. & Madadi, M. 2017. Effect of grain shapes in coordination number from micro-CT image analysis of an unconsolidated sand. In: 79th EAGE Conference and Exhibition, Paris, France.

Ahmed, Z., Lebedev, M., Madadi, M. & Uvarova, Y. 2016. Inverting Dynamic Elastic Moduli of a Granular Pack to Get Shear Modulus of the Grain. In: ASEG-PESA-AIG 2016, 25th Geophysical Conference and Exhibition, pp. 944-948.

Al-Raoush, R. 2007. Microstructure characterization of granular materials. Physica A: Statistical Mechanics and its Applications 377, 545-558.

Al-Raoush, R. & Papadopoulos, A. 2010. Representative elementary volume analysis of porous media using X-ray computed tomography. Powder Technology 200, 69-77.

Alshibli, K.A., Druckrey, A.M., Al-Raoush, R.I., Weiskittel, T. & Lavrik, N.V. 2015. Quantifying Morphology of Sands Using 3D Imaging. Journal of Materials in Civil Engineering 27, 04014275.

Andrä, H., Combaret, N., Dvorkin, J., Glatt, E., Han, J., Kabel, M., Keehm, Y., Krzikalla, F., Lee, M., Madonna, C., Marsh, M., Mukerji, T., Saenger, E.H., Sain, R., Saxena, N., Ricker, S., Wiegmann, A. & Zhan, X. 2013. Digital rock physics benchmarks—Part I: Imaging and segmentation. Computers & Geosciences 50, 25-32.

Arasan, S., Akbulut, S. & Hasiloglu, A.S. 2011. The relationship between the fractal dimension and shape properties of particles. KSCE Journal of Civil Engineering 15, 1219-1225.

Aste, T., Saadatfar, M. & Senden, T.J. 2005. Geometrical structure of disordered sphere packings. Phys Rev E Stat Nonlin Soft Matter Phys 71, 061302.

Buades, A., Coll, B. & Morel, J. 2005. A non-local algorithm for image denoising. IEEE CPVR.

Cavarretta, I. 2009. The Influence of Particle Characteristics on the Engineering Behaviour of Granular Materials. In: Dept. of Civil and Environmental Engineering, Vol. PhD. Imperial College London.

Chaze, M. & Cambou, B. 2014. Analysis of internal state and strains in granular material at meso-scale: influence of particle shape. Granular Matter 16, 657-673.

Cox, M.R. & Budhu, M. 2008. A practical approach to grain shape quantification. Engineering Geology 96, 1-16.

Dondi, G., Simone, A., Vignali, V. & Manganelli, G. 2012. Discrete Element Modelling of Influences of Grain Shape and Angularity on Performance of Granular Mixes for Asphalts. Procedia - Social and Behavioral Sciences 53, 399-409.

Druckrey, A.M., Alshibli, K.A. & Al-Raoush, R.I. 2016. 3D characterization of sand particle-to-particle contact and morphology. Computers and Geotechnics 74, 26-35.

Duffaut, K., Landro, M. & Sollie, R. 2010. Using Mindlin theory to model friction-dependent shear modulus in granular media. Geophysics 75, E143–E152.

Dutta, T., Mavko, G. & Mukerji, T. 2010. Improved granular medium model for unconsolidated sands using coordination number, porosity , and pressure relations. Geophysics 75, E91-E99.

Fonseca, J., O'Sullivan, C., Coop, M.R. & Lee, P.D. 2012. Non-invasive characterization of particle morphology of natural sands. Soils and Foundations 52, 712-722.

Friedman, G.M. 1962. On sorting, sorting coefficients, and the lognormality of the grain-size distribution of sandstones. The Journal of Geology 70, 737-755.

Garcia, X. & Medina, E. 2006. Hysteresis effects studied by numerical simulations: Cyclic loading-unloading of a realistic sand model. Geophysics 71, F13-F20.

Graton, L.C. & Fraser, H.J. 1935. Systematic Packing of Spheres- With Particular Relation to Porosity and Permeability. The Journal of Geology 43, 785-909.

Gualda, G.A.R. & Rivers, M. 2006. Quantitative 3D petrography using x-ray tomography: Application to Bishop Tuff pumice clasts. Journal of Volcanology and Geothermal Research 154, 48-62.

Ha Giang, P.H., Van Impe, P., Van Impe, W.F. & Menge, P. Year. Effects of grain size distribution on the initial small strain shear modulus of calcareous sand. Conference Effects of grain size distribution on the initial small strain shear modulus of calcareous sand, Edinburg, UK, 3177–3182.

Ham, A., Wang, J. & Stammer, J.G. 2012. Relationships between Particle Shape Characteristics and Macroscopic Damping in Dry Sands. Journal of Geotechnical and Geoenvironmental Engineering 138, 1002-1011.

Hasan, A. & Alshibli, K.A. 2010. Experimental assessment of 3D particle-to-particle interaction within sheared sand using synchrotron microtomography. Géotechnique 60, 369-379.

Iassonov, P., Gebrenegus, T. & Tuller, M. 2009. Segmentation of X-ray computed tomography images of porous materials: A crucial step for characterization and quantitative analysis of pore structures. Water Resources Research 45.

Inman, D.L. 1952. Measures for describing the size distribution of sediments. Jour. Sed. Petrology 22, 125-145.

Kröner, S. & Doménech Carbó, M.T. 2013. Determination of minimum pixel resolution for shape analysis: Proposal of a new data validation method for computerized images. Powder Technology 245, 297-313.

Krumbein, W.C. & Sloss, L.L. 1963. Stratigraphy and Sedimentation. W.H. Freeman, San Francisco 2nd Edition.

Lin, C.L. & Miller, J.D. 2005. 3D characterization and analysis of particle shape using X-ray microtomography (XMT). Powder Technology 154, 61-69.

Liu, Q., Xiang, W. & Lehane, B.M. 2015. The Effect of Overconsolidation and Particle Shape on the CPT End Resistance of Granular Soils. 229-238.

Makse, H.A., Gland, N., Johnson, D.L. & Schwartz, L. 2004. Granular Packings-Nonlinear elasticity, sound propagation and collective relaxation dynamics. Phys. Rev. E 70, 061302.

Moreno-Atanasio, R., Williams, R.A. & Jia, X. 2010. Combining X-ray microtomography with computer simulation for analysis of granular and porous materials. Particuology 8, 81-99.

Murphy, W. 1982. Effects of microstructure and pore fluids on the acoustic properties of granular sedimentary materials. PhD dissertation. Stanford University.

Oda, M. 1972. Initial fabrics and their relations to mechanical properties of granular material. Soils and Foundation 12, 17-36.

Oh, W. & Lindquist, W.B. 1999. Image Thresholding by Indicator Kriging. IEEE Trans. Pattern Anal. Mach. Intel. 21, 590– 602.

Otsu, N. 1979. A Tlreshold Selection Method from Gray-Level Histograms. IEEE Trans. Syst. Man Cybern 9.

Powers, M.C. 1953. A new roundness scale for sedimentary particles. Journal of Sedimentary Petrology 23, 117-119.

Randolph, K. A. & Myers, L. L. 2013, Basic statistics in multivariate analysis. Oxford University Press. Print ISBN-13: 9780199764044. DOI: 10.1093/acprof:oso/9780199764044.001.0001

Ridler, T.W. & Calvard, S. 1978. Picture thresholding using an iterative selection method. IEEE Trans. Syst. Man Cybern 8.

Sain, R. 2010. Numerical simulation of pore-scale heterogeneity and its effects on elastic, electrical and transport properties. In: Department of Geophysics, Vol. PhD thesis. Stanford University.

Santamarina, J.C. & Cho, G.C. 2003. Soil behaviour- The role of particle shape. Conference Soil behaviour- The role of particle shape, 604–617.

Seidler, G.T., Martinez, G., Seeley, L.H., Kim, K.H., Behne, E.A., Zaranek, S., D., C.B., Heald, S.M. & Brewe, D.L. 2000. Granule-by-granule reconstruction of a sandpile from x-ray microtomography data. Physical Review E 62, 8175–8182.

Sezgin, M. & Sankur, B. 2004. Survey over image thresholding techniques and quantitative performance evaluation. Journal of Electronic Imaging 13, 146-165.

Silbert, L.E., Ertas, D., Grest, G.S., Halsey, T.C. & Levine, D. 2002. Geometry of frictionless and frictional sphere packings. Phys Rev E Stat Nonlin Soft Matter Phys 65, 031304.

Smith, W.O., Foote, P.D. & Busang, P.F. 1929. Packing of Homogeneous Spheres. Physical Review 34, 1271-1274.

Tabachnick B. G. & Fidell L. S. 2013. Using multivariate statistics (6th ed.). Boston: Pearson Education. ISBN: 9780205849574

Thompson, K.E., Willson, C.S. & Zhang, W. 2006. Quantitative computer reconstruction of particulate materials from microtomography images. Powder Technology 163, 169-182.

Trask, P.D. 1932. Origin and environment of source sediments of petroleum. Houston, Gulf Pub. Co., 67p.

Viggiani, G., Andò, E., Jaquet, C. & Talbot, H. 2013. Identifying and following particle-to-particle contacts in real granular media: An experimental challenge. Conference Identifying and following particle-to-particle contacts in real granular media: An experimental challenge, 60-65.

Wadell, H. 1932. Shape, and Roundness of Rock Particles. The Journal of Geology 40, 443-451.

Wadell, H. 1934. Shape determination of large sedimental rock fragments. The Pan-American Geologist 61, 187-220.

Wildenschild, D. & Sheppard, A.P. 2013. X-ray imaging and analysis techniques for quantifying pore-scale structure and processes in subsurface porous medium systems. Advances in Water Resources 51, 217-246.

Zavala, J.M.R. 2012. Particle shape quantities and influence on geotechnical properties—A review. In: Department of Civil, Environmental and Natural Resources, Vol. PhD thesis. Luleå Univ. of Technology, Luleå, Sweden.

Zeidan, M., Jia, X. & Williams, R.A. 2007. Errors implicit in digital particle characterisation. Chemical Engineering Science 62, 1905-1914.

Zimmer, M.A. 2003. Seismic velocities in unconsolidated sands: measurements of pressure, sorting, and compaction effects. In: Department of Geophysics, Vol. PhD thesis. Stanford University.

Appendix 2.A: Matlab code that calculates coordination number (C) and contact surface area

```
%
=========================================================================
====


% This script computes coordination number and contact surface area
% of a grain from a 3D micro-CT image of a granular pack. The image
% should be in ASCII format that has a single column of all the voxel
% values, each of which represents either a grain label or
% a void space as 0. Here in this case, it is imported from AVIZO,
% a commercial software for micro-CT image processing.


% 4th of June, 2018; Zubair Ahmed; Curtin University and DET CRC.


%=========================================================================
======


tic
%ASCII image file
D_ = dlmread('S-0_730-988_0.9814.am','\t',16,0);
%List of grain labels of which CN and contact surface area are
calculated
M = dlmread('M_S-0_730-988_0.9814.csv');
%resolution of the image (here in micrometer)
res = 0.9814;
```

```
%2D surface area of a voxel face

voxel_area = power(res,2);

%Dimnesion of the image

X = 717;

Y = 637;

Z = 259;

%Create 3D Matrix, each of the coordinates of which represents a voxel

Im_3D = reshape(D_,[X,Y,Z]);

% Preallocation

Isol_all = cell(1,length(M));

Isol_grains = cell(1,length(M));

Im_dil = cell(1,length(M));

Cont = cell(1,length(M));

Grains_cont = cell(1,length(M));

Coor_num = cell(1,length(M));

%#For CN (coordination number)

for i = 1:length(M)

    %Isolate each grain in binary

    Isol_all{i} = Im_3D ==M(i,:);

    %Isolate each grain with its respective label

    Isol_grains{i} = Isol_all{i}.*M(i,:);

    %Dilate a grain with 26 connectivity to capture all the connected
voxels

    Im_dil{i} = imdilate(Isol_grains{i},ones(3,3,3));
```

```
    %Grains that have contact with a particular grain
    Cont{i} = ((Im_dil{i})./M(i,:)).*(Im_3D);
    %Make the label of that particular grain 0
    Cont{i}(Cont{i} == M(i,:)) = 0;
    %Label of the grains that are in contact
    Grains_cont{i} = unique(Cont{i})';
    Grains_cont{i}(Grains_cont{i}==0) = NaN;
    %Coordination number of the particular grain
    Coor_num{i} = numel(Grains_cont{i})-1;
    Cn_ = cell2mat(Coor_num)';
end


%#For contact area
%Number of grains that are to calculate the contact area
for j = 1:length(Grains_cont)
    %Number of grains that are in contact with a particular grain
    for k = 1:(length(Grains_cont{j}))
        % number of contact voxels
        Cn_area=
sum(sum(sum(Cont{j}==Grains_cont{j}(k))))*voxel_area;
        area_Cn{j}(k) = Cn_area;
    end
end
```

```
%%Output of CN and Contact surfacea area in two separate files

%Get the maximum vector size

maxSize = max(cellfun(@numel,Grains_cont));

%# Create an anonymous function

fcn = @(x) [x zeros(1,maxSize-numel(x))];

%# Pad each cell with NaNs

rmat_G = cellfun(fcn,Grains_cont,'UniformOutput',false);

rmat_A = cellfun(fcn,area_Cn,'UniformOutput',false);

%# Vertically concatenate cells

rmat_G = vertcat(rmat_G{:});

rmat_A = vertcat(rmat_A{:});

%CN of all the grains in the list M

CN_ = [M Cn_ rmat_G];

%Output Columns

%Column_1, M = Grain index or ID

%Column_2, Cn_= Coordination number

%Column_3, rmat-G = Grain ID that have contact with the targer grain

%Total contact surface area of each grain in the list M

CN_AREA = [M Cn_ sum(rmat_A,2) rmat_A];

%Output Columns

%Column_1, M = Grain index or ID

%Column_2, Cn_= Coordination number

%Column_3, sum(rmat_A,2) = total contact surface area
```

```
%Column_4 and on, rmat_A = Surface area of individual contacts

toc
```

Appendix 2.B: Correlation Coefficients

Statistical analysis for finding the correlation between two or more variables are available in a number of text books that covers the basics of multivariate regressions (e.g. Tabachnick and Fidell (2013) and Randolph and Myers (2013)). However, we are presenting a summary of the correlation terms and their derivation to give an overview on the data analysis used in our study.

Correlation coefficient is the quantitative measure of strength of the relationship between two variables. One of the common and popular type is Pearson's Correlation Coefficient, *r*, that describes linear relationship in a range of -1 to +1, inclusive. In this range, 1 means the strongest possible relationship and 0 means no relationship at all whereas negative and positive signs mean opposite and similar trend between the variables, respectively. This correlation coefficient can be formulated as

$$r_{xy} = \frac{1}{n-1}\sum_{i=1}^{n}\frac{(x_i-\bar{x})(y_i-\bar{y})}{\sigma_x\sigma_y} \qquad \text{B-1}$$

where x_i and y_i are the ith data, $\bar{x}$ and $\bar{y}$ are the arithmetic mean, σ_x and σ_y are the standard deviation of the variables of x and y, respectively, and n is the number of samples in a variable.

A common practice to understand the acceptance of this coefficient and test the hypotheses is to calculate the Probability value, more robustly termed as P-value which ranges from 0 to 1. This value is used for considering to reject either null (H_0) or alternative (H_1) hypotheses where the former one is assumed to be true during the testing. This rejection decision normally depends on a threshold P-value called alpha level, defined by the user, below which the null hypotheses may be rejected. A typical alpha level is used as 0.05. In our case, we have taken the H_0 as no correlation exists between the variables and H_1 as the opposite, there may be an existing relationship. To find the P value, after assigning the hypothesis first, t-value (Student's T distribution) is obtained using the following equation that can be expressed in terms of Pearson r and degree of freedom (number of variables deducted from number of samples in a variable, here in our case, $n-2$):

$$t_{xy} = r_{xy}^2 \sqrt{\frac{n-2}{1-r_{xy}^2}} \quad \text{B-2}$$

From a t distribution table by using this t value, we can find the P-value for the particular degree of freedom. P-value is then compared with the user defined alpha level to make a decision on the rejection of the hypothesis.

If there are more than two variables, correlation coefficients between two variables are most likely contain the effect of other variables. To get rid of this effect, partial correlation coefficients can be calculated controlling the other variables constant. For three variable scenario, partial correlation coefficient between x and y controlling the variable z can be expressed as

$$r_{xy|z} = \frac{r_{xy} - r_{xz} r_{yz}}{\sqrt{(1-r_{xz}^2)(1-r_{yz}^2)}} \quad \text{B-3}$$

where, the subscripts of r denote the variables.

3. Elastic properties of sands, Part 2: Implementation of contact-based model to determine the elasticity of the grains from ultrasonic measurements[2]

3.1. Abstract

The prediction of effective elastic properties of a granular medium using ultrasonic data based on contact models has been studied widely in both laboratory experiments and numerical simulations. In contrast, calculation of the elastic properties of the constituent grains using similar data by inverting the equations from those models is a rather new concept. To do so, we have developed a controlled experiment technique that includes a uniaxial compaction test and measures ultrasonic velocities of four unconsolidated quartz sand samples with different sorting and grain shapes. We observe that both P and S wave velocities are significantly influenced by the microstructure or internal arrangement of the grains. Well sorted and more spherical and rounded samples show higher velocities than poorly sorted and less spherical and rounded samples. A microstructural parameter – namely the coordination number – we have calculated from high-resolution micro-CT images provides a good match between the model and the dynamic effective bulk moduli of the sand pack. Combining this coordination number with a frictional parameter calculated from the measured velocity ratios, has been very effective to fit the model with the dynamic effective shear moduli. Using these two key parameters along with the experiment results, from the contact models we have been able to obtain the elastic parameters of the quartz sand grains in the sample. Elastic parameters obtained thus are very close to the actual values of the quartz grains found in the literature. This technique can be useful in hard rock mineral exploration where missing core samples or an absence of well logs can be replaced by laboratory measurements of powders to determine the

[2] This Chapter is an extended version of the paper submitted to Geophysical Prospecting. (accepted for publication 08/01/2019)

elasticity or velocities of the rocks. Moreover, the elastic properties of the solid phase calculated using this technique can be used as input parameters for the fluid substitution and rock physics characterisation of unconsolidated reservoir sands.

3.2. Introduction

Drill cuttings that come up during drilling in hard rock environments can provide mechanical properties of the rocks from where they are fragmented. Very often, solid core samples may be broken or missing and sonic logs may be absent. Moreover, the acquisition and analysis of solid cores and sonic logs are time consuming and expensive. On the other hand, in a soft rock environment, unconsolidated sands can be potential reservoirs for hydrocarbons in shallow deposits in deep water settings. These sands can be gas hydrate-bearing sediments as well. Additionally, most of the aquifers consist of unconsolidated sands. In rock physics characterisation of these sands, most of the time, the elastic properties of quartz are used during fluid substitution processes even though the composition of rocks may have a number of other minerals with different elasticity. In both hard and soft rock cases, knowing the elastic properties of the constituent grains can resolve these problems. In this study, our aim is to develop a simple but efficient laboratory technique that incorporates ultrasonic velocity measurement and follows conventional models based on effective medium theory (EMT) on a granular medium to calculate the elastic properties of the constituent grain.

Most of the existing contact-based models in the literature are based on the assumption of different initial conditions and strain field approximations. Hertz (1882) calculates effective bulk moduli of the pack considering the normal compression of two spheres. Mindlin (1949) assumes a tangential force applied to the grain contact after initial normal compression. He assumes that the tangential force can cause partial slippage on the edge of the grain contacts. Walton (1987) differs from Mindlin (1949) by the assumption that both normal and shear strains are acting simultaneously and there is no partial slippage. Instead, the contact surfaces are assumed to have either total slippage, caused by the contact between very smooth grain surfaces, or no slippage, incorporated by extremely rough grain surfaces. Digby (1981) assumes that the grains are all bonded in their circular contact surfaces prior to applying strain. Jenkins et al. (2005) allow the relative motion of the particles to deviate from the mean homogenous

strain field. The resultant effective shear modulus of the granular pack is found to be smaller than the previous models. Brandt (1955) proposes a model to calculate the effective bulk modulus of a dry granular pack of spheres with same elasticity but different sizes. Norris and Johnson (1997) and Johnson et al. (1998) have effective medium models for predicting non-linear elasticity of the granular pack.

So far, most of the studies concentrate on a forward-modelling approach, by predicting the effective elastic moduli of the granular pack following contact-based models either using laboratory measurements (e.g. Domenico 1977, Yin 1992, Zimmer 2003) or numerical simulations (e.g. Makse et al. 2004, Sain 2010). Prediction of effective bulk moduli following the Hertz-Mindlin (HM) (Hertz 1882, Mindlin 1949) or Walton (1987) models has been found to be in good agreement with both laboratory data (Dutta et al. 2010, Saul et al. 2013) and numerical simulations (Makse et al. 1999, Sain 2010). Even though a few studies show that Walton's smooth model (total slippage) fits better with the laboratory data on dry sands (Koochak Zadeh et al. 2016) and gas hydrate bearing sediments (Sava and Hardage 2006), the majority of the published literature on this topic, including the data from Winkler (1983) and Goddard (1990), reports that effective shear modulus is largely over-predicted by HM and Walton's no slip models. Unconsolidated sand, having no adhesive bonding by cements, is much more likely to have a situation in between the two extreme cases modelled by Walton (1987). Therefore, to deal with this over-prediction in effective shear moduli, a number of studies (Bachrach and Avseth 2008, Dutta et al. 2010, Gallop 2013) emerge using a parameter called 'fraction of no slip' contact, termed 'α' by Jenkins et al. (2005). This parameter represents the fraction of contacts that have no slippage at all in the medium. Duffaut et al. 2010 modified this parameter using Mindlin's frictional term, which is a function of the friction coefficient of the grains and considers the partial slippage over the contact surface. On the other hand, Makse et al. 1999, after a granular dynamics (GD) simulation, argue that grain relaxation after affine strain is the main cause of this discrepancy, which EMT models overlook. On that basis, Sain (2010) implements relaxation corrections calculated from numerical simulations on the ultrasonic laboratory data. Saul et al. (2013) follow a similar concept by applying calibration parameters to the effective shear modulus derived from least square fitting on the same data. They also use another calibration parameter as a replacement of the coordination number (C), which is a crucial parameter in predicting the effective bulk

moduli of the sample. Discrepancies between the calculated coordination numbers obtained from empirical relationships and numerical simulations are reported in a number of works (e.g. Duffaut and Landrø 2007, Makse et al. 1999, Dutta et al. 2010, and Bachrach and Avseth 2008). To avoid such discrepancy, we calculate the actual C from the micro-CT images of our sample (details are in the previous chapter).

In contrast with the forwarding approach, inverting the effective elastic properties of the granular medium to calculate the elastic properties of the constituent grain is rather new. A successful attempt to invert the contact-based model to calculate the grain's elastic properties is found in Madadi et al. (2015), where the authors use ultrasonic measurements to calculate the combined elastic constants (in terms of shear modulus and Poisson's ratio) of the grains following Hertz's (1882) model. They adopt an arbitrary factor of non-spherical grain shape and poly-dispersity to modify the coordination number-pressure function derived from numerical simulation by Makse et al. (2004). Ahmed et al. 2016 use an extended Walton model (e.g. Jenkins et al. 2005) to calculate the shear modulus of the grain using coordination numbers from existing literature and a constant fraction of no slip contact, α. In this study, we extend this previous work by implementing a refined experimental procedure, using an accurate C from micro-CT images of each sample and finally being able to obtain the elastic parameters of the grains. However, there are assumptions and limitations in both the adopted model and our experiment setup. The model considers the grain to be identical spheres with the same elasticity whereas one of our samples has a narrow size range of almost all quartz grains but not perfectly spherical. Another assumption is that during pressure increments, no new grain contacts will be added nor any of the existing ones lost, which means C is constant. In our controlled experiment, limited range of stress applied to the samples causes very insignificant change in C and this allows to adhere with that assumption. A key limitation of the model is that it allows a certain range of V_P/V_S ratio of the sample that can be validly used to determine a key parameter that involves with the intergranular friction. Moreover, the model that we used relied upon hydrostatic pressure but for the feasibility we applied uniaxial stress on the sample enclosed in a well-confined chamber. Our assumption based on the fact that the stress regime inside the closed chamber has a similar effect as hydrostatic pressure. Even though the pressure regime is slightly altered in the sample, we will see that the forward models considering the isotropic case fit well with the measured data.

To investigate the potential anisotropy effect, we also analyse the transversely isotropic version of Walton's model, from which the results show acceptable matches as well.

This chapter starts with the relevant theoretical background and how we utilize the models to solve the problem. This is followed by a comprehensive description on experiment setup and methodology to preform ultrasonic measurements with increasing stress. Later we describe preparation of the samples and an analysis of their condition after applying stress. We also provide an overview of the intergranular frictional term used in the previous literatures with a justification of a similar parameter we use in this study. Next we present the experiment results and key parameters, followed by the forward modelling and the calculation of the elastic properties of the constituent grains, with extensive analyses in each part. Before concluding, we put forward a discussion that covers the main findings from this study.

3.3. Theoretical background and our approach

Walton (1987) calculates the effective elastic moduli of a granular pack of randomly distributed spherical grains with the same size and elasticity. His approach is to calculate the elasticity from the infinitesimal strain increment resulting from tiny stress which is assumed to be homogenously distributed inside the pack. During this process, one of the key assumptions is that no new contacts are added nor are any of the existing contacts lost. Taking the contact adhesiveness into account, for simplicity, he presents two extreme cases. One is "total slip contact", where all the grains that have contacts with their neighbors slide completely over each other. The second one is "no slip contact", where all the grains are locked with each other, thus no sliding or slippage occurs over the contact surface area. These two extreme cases merely describe the practical situation a granular sample faces while confined stress is applied. A further assumption is made to adhere with the real scenario by adding a parameter that constitutes the fraction of no slip contacts over all the contacts in the pack. Hence an extended Walton model has been presented in Jenkins et al. (2005) that has been able to solve the discrepancy between the model and dynamic lab data for the prediction of shear wave velocities (Dutta et al. 2010). The fraction of no slip contacts α ranges

from 0 to 1, in which 0 means total slippage and 1 means the contact is locked (no slippage at all).

A number of previous studies (e.g. Bachrach and Avseth 2008, Dutta et al. 2010, Saul et al. 2013) included a brief overview on the derivation of effective bulk and shear moduli of the granular pack from the contact stiffness equations. Therefore, in this study we refrain from re-articulating those; rather, we start from the ultimate equations that we use in this study. When a hydrostatic pressure is applied to a granular pack in order to predict effective bulk modulus, the tangential stiffness of the grain contacts resulting from the tangential force is not accounted for, hence α is not applied. This means that the effective bulk moduli (K_{eff}) in both total slippage and no slippage cases (i.e. for any α) are equal and is expressed as:

$$K_{eff} = \frac{1}{6}\left[\frac{3C^2(1-\phi)^2P}{\pi^4B^2}\right]^{\frac{1}{3}}, \tag{3.1}$$

however, α, is included in the effective shear modulus (μ_{eff}):

$$\mu_{eff} = \frac{1}{10}\left[\frac{3C^2(1-\phi)^2P}{\pi^4B^2}\right]^{\frac{1}{3}}\left[1+\frac{3\alpha B}{2B+A}\right] \tag{3.2}$$

and in the effective Poisson's ratio (υ_{eff}) as

$$\upsilon_{eff} = \frac{2-\upsilon-2\alpha(1-\upsilon)}{8-4\upsilon+2\alpha(1-\upsilon)} \tag{3.3}$$

where,

$$A = \frac{1}{4\pi}\left(\frac{1}{\mu}-\frac{1}{\mu+\lambda}\right) \tag{3.4}$$

$$B = \frac{1}{4\pi}\left(\frac{1}{\mu}+\frac{1}{\mu+\lambda}\right). \tag{3.5}$$

A and B are combinations of shear modulus (μ) and Lamé's first parameter (λ) of the grain; υ is the Poisson's ratio of the grain, and P, ϕ, and C are respectively hydrostatic pressure, porosity and coordination number. Clearly from equation 3.3, we can see that

for the total slip condition, where α=0, effective Poisson's ratio becomes 0.25, which is the maximum possible value according to this model. In terms of the V_P/V_S ratio (where V_P and V_S are the compressional and shear wave velocities respectively), this value corresponds to around 1.731.

Hydrostatic compaction of unconsolidated sands is difficult; thus, a majority of such experiments are performed in odeometric cells, applying uniaxial stress to the sample. For uniaxial compaction rather than hydrostatic pressure the sample acts as transversely isotropic (TI) material in which the axis of symmetry has the same direction as with induced stress and the isotropic plane is vertical to it. Walton (1987) derived all the five stiffness constants for a TI medium taking the strain, e_3 in the direction of the axis of symmetry. For the no slip case, they are

$$C_{11} = 3(\gamma + 2\beta),\ C_{12} = \gamma - 2\beta,\ C_{13} = 2C_{12},\ C_{33} = 8(\gamma + \beta),\ \text{and}\ C_{44} = \gamma + 7\beta \tag{3.6}$$

where, $\gamma = \frac{C(1-\phi)e_3^{\frac{1}{2}}}{32\pi^2 B}$, $\beta = \frac{(1-\phi)Ce_3^{\frac{1}{2}}}{32\pi^2(2B+A)}$ and $e_3 = \left[\frac{6\pi^2 B(2B+A)\sigma_3}{C(1-\phi)(3B+A)}\right]^{\frac{2}{3}}$, and $\sigma_3$is the uniaxial stress in the direction of axis of symmetry. For the no slip case, the constants are

$$C_{11} = 3\gamma,\ C_{12} = C_{44} = \gamma,\ C_{13} = 2\gamma,\ \text{and}\ C_{33} = 8\gamma. \tag{3.7}$$

On the other hand, seismic phase velocities in a plane that contains the axis of symmetry can be expressed in terms of the stiffness constants and the angle, θ between the wave vector and axis of symmetry, as follows:

$$V_P = (C_{11}sin^2\theta + C_{33}cos^2\theta + C_{44} + \sqrt{M})^{\frac{1}{2}}(2\rho)^{-\frac{1}{2}} \tag{3.8}$$

and

$$V_{SH} = \left(\frac{C_{66}sin^2\theta + C_{44}cos^2\theta}{\rho}\right)^{\frac{1}{2}}$$

$$V_{SV} = (C_{11}sin^2\theta + C_{33}cos^2\theta + C_{44} - \sqrt{M})^{\frac{1}{2}}(2\rho)^{-\frac{1}{2}} \tag{3.9}$$

where,

$$M = [(C_{11} - C_{44})sin^2\theta - (C_{33} - C_{44})cos^2\theta]^2 + (C_{13} - C_{44})^2 sin^2 2\theta \quad (3.10)$$

and V_{SH} and V_{SV} are horizontally (pure shear mode) and vertically (quasi–shear mode) polarized shear waves respectively. Both equations 3.8 and 3.9 reduce to the following for $\theta = 0$, where the wave direction is along the principal axis of symmetry, as

$$C_{33} = \rho {V_P}^2 \quad (3.11)$$

and

$$C_{44} = \rho {V_{SH}}^2 = \rho {V_{SV}}^2 = \rho {V_S}^2. \quad (3.12)$$

We can rearrange Eq. 3.3 to calculate α from the effective elastic parameter expressed by the V_P/V_S ratio of the granular pack and Poisson's ratio of the constituent grain as:

$$\alpha = \frac{(2-\upsilon)(3-\frac{V_P^2}{V_S^2})}{(1-\upsilon)(3\frac{V_P^2}{V_S^2}-4)} \quad (3.13)$$

This equation also shows that α is dependent neither on P nor C; rather, it is dependent on the effective elastic modulus of the granular pack and elastic modulus of the constituent grain. Following Eq. 3.13, Figure 3.1 shows the range of α as a function of the V_P/V_S ratio of the granular pack for the theoretical boundaries of a grain's Poisson's ratios 0 and 0.5.

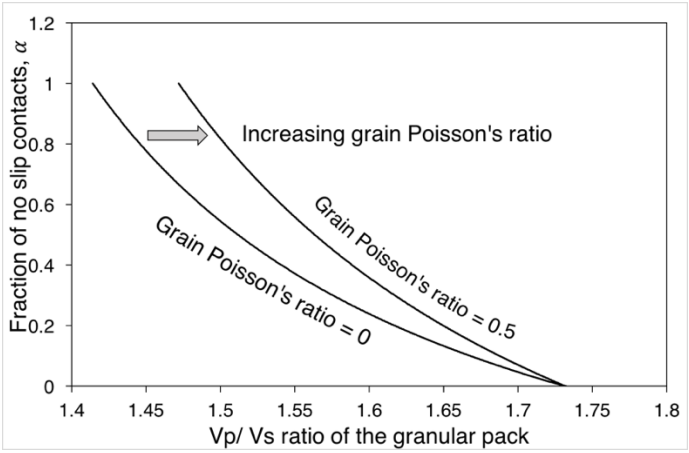

Figure 3.1: Fraction of no slip contacts, α with respect to velocity ratio of the pack and Poisson's ratio of the grain.

The velocities and porosity measured during the experiment can provide the dynamic effective elastic moduli. Thus, the effective bulk and shear moduli are determined from the experiment as:

$$K_{eff} = \rho_S(1-\phi)\left(V_P^2 - \frac{4}{3}V_S^2\right) \tag{3.14}$$

$$\mu_{eff} = \rho_S(1-\phi)V_S^2 \tag{3.15}$$

where ρ_S is the density of the constituent grain.

We calculate B at each stress from Eq. 3.1 using parameters P, ϕ and K_{eff} obtained in the experiment and C from the micro-CT image analysis. A detailed description of the image processing and procedure to obtain C can be found in the previous chapter. On the other hand, using the V_P/V_S ratio from the experiment, Eq. 3.13 can provide lower and upper limits of α at each stress level considering the grain's Poisson's ratio as 0 and 0.35. There are two reasons to choose this Poisson's ratio range. Firstly, Poisson's ratios of most of the rocks and their forming minerals fall inside this range and, secondly, a narrow constraint can facilitate a more accurate result from the final calculation. By substituting B and α values into Eq. 3.2, we can obtain the lower and upper limits of A corresponding to the upper and lower Poisson's ratio of the grain at each stress. The resultant upper and lower limits of A together with B can give the lower and upper limits of the shear modulus of the grain from Eq. 16, which is a combination of Eqs 3.4 and 3.5:

$$\mu = \frac{1}{2\pi}\left(\frac{1}{A+B}\right) \tag{3.16}$$

Finally, constraining with these upper and lower limits of the shear moduli of the grain, a non-linear least square solution of Eq. 3.2 gives the elastic properties of the grain and corresponding values of the fraction of no slip contacts, α.

3.4. Experiment setup and methodology

We put the dry sample of unconsolidated sands inside a cylindrical chamber with a diameter of 6 cm and height of 8 cm. Both ends of this chamber are open and entirely made of Polyether Ether Ketone (PEEK) plastics (Figure 3.2a). This plastic can withstand up to 40 MPa of hydrostatic pressure and 70 MPa of uniaxial stress inside the chamber. Two pistons made of the same material close both of the ends of the chamber. Two piezoelectric transducers of 1MHz central frequency are firmly attached with these pistons at their ends. All this setup stands beneath a hydraulic actuator, which is attached to the top of a metallic frame. The actuator is connected to an oil-driven pressure pump, which is used to control the applied stress on the sample. In addition, both the source and receiver transducers are connected to an Olympus square wave pulser/receiver (model 5077PR) that excites the ultrasonic wave. A digital oscilloscope (Tektronix TDS 3034C) records and stores the transmitted pulse with respect to travel time sent from the wave pulser. Also, we maintain one scale to measure the change in length of the sample along with the increasing stress to calculate the corresponding volumetric change. As the sample is enclosed inside the chamber while placed under uniaxial stress, the stress regime inside the sample is close to hydrostatic rather than uniaxial compaction.

Following the recommendations from Ahmed et al. (2016), we set key parameters that include the loading–unloading sequence and top stress level. We start our measuring sequence with a couple of loading–unloading cycles up to 2.52 MPa, and then apply a long loading tail up to 12.60 MPa (Figure 3.2b). The initial two cycles are intended to stabilise the grains' mutual arrangement prior to applying the virgin loading tail so that the later higher stresses would likely have no grain rotation or dislodgement. Moreover, to have a valid α value, the model (Figure 3.1) requires that the V_P/V_S ratio obtained from the measurements is lower than 1.731, which corresponds to a state in which at least some of the grain contacts have no slippage. Hence these prior loading–unloading cycles can establish the contact network so that S waves can travel faster to keep the V_P/V_S ratio inside the range that would provide valid α values. We limit the maximum stress level to 12.60 MPa, primarily for two reasons. Firstly, we want to reduce the effect of increasing stress on C so that we can use a constant C over the stress range. Secondly, we do not want the grains to be crushed during the

increasing stress, which could alter the granular arrangement inside the sample. We measure the ultrasonic velocities with their corresponding volumetric change in the loading tail from 3.15 to 12.6 MPa and use these measurements for further calculation.

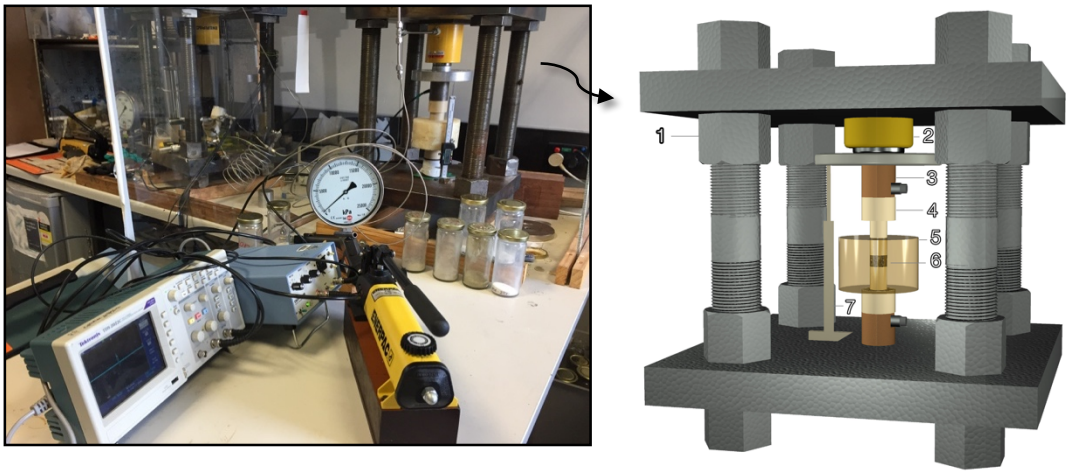

(a)

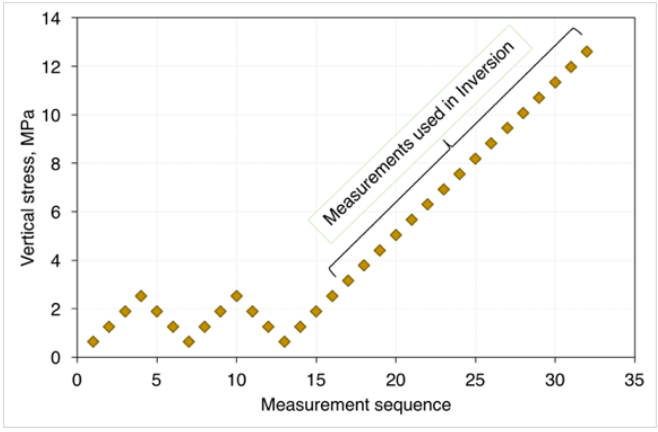

(b)

Figure 3.2: (a) Experiment set-up: (1) frame, (2) hydraulic actuator, (3) ultrasonic transducer, (4) piston, (5) plastic chamber, (6) sample, (7) measuring scale; (b) sequence of ultrasonic measurement at different vertical stresses.

3.5. Sample preparation

We prepare four samples with different grain size distribution and shape factors from an unconsolidated sand collected from Esperance Beach, Western Australia (33°59′40″S 122°13′57″E). The sand is white in color, consists of mostly quartz, and is well sorted and rounded. We pulverize the sands in a mortar and pestle to create smaller sizes and more angular shaped grains. We then sieve the sand into 56–106 μm and 106–256 μm fractions and mix the fractions with different proportions, as shown in Table 3.1. Before putting the samples into the cell for stress application and subsequent ultrasonic measurement, we demoisturise the sample in an oven for 24 hours so that P wave propagation would not be biased by effects related to fluid inside the sample. After measuring the travel times following the sequence described in the previous section (Figure 3.2b), we solidify the sample by injecting epoxy resin; after solidification, we cut and polish the subsamples to acquire a micro-CT image (described in the previous chapter).

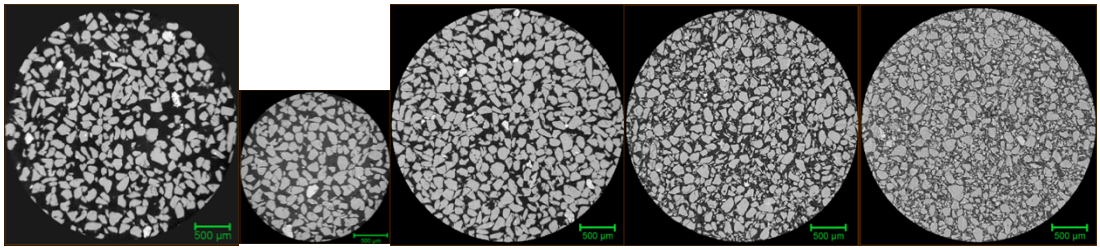

Intact 12.6 MPa 25 MPa 85 MPa 145 MPa

Figure 3.3: Slices of micro CT images of Esperance beach sand sample after applying different end stresses which are written below the respective image. The scale bar represents 500 μm in all the images.

3.6. Compaction effect on the grains

Applying stress to the granular pack during ultrasonic measurement can cause grains to be crushed. Koochak Zadeh et al. (2016) experience grain crushing in their experiment where they reach 30 MPa of vertical stress on a 355 to 500 μm grain-size sample. We investigate the possibility of grain damage by applying different axial stresses on the sands. Micro-CT images (Figure 3.3) of the sand grains that

experienced a wide range of vertical stresses show a significant number of smaller grain sizes appear when the stress exceeds 25 MPa. To avoid grain crushing, we restrict the maximum stress up to 12.6 MPa and choose a smaller grain size of no more than 200 µm. The grain size distribution expressed as a normalised count of the number of grains for sample S-0 shows no grain crushing after the compaction test (Figure 3.4).

Table 3.1: Size distribution based on sieving during the preparation of the samples. Note absence of fraction 35–56, which was found later on from micro-CT image analysis. Sorting and grain shape factors are also provided. Lower sorting index means well-sorted sample and higher sphericity and roundness values indicate more spherical and rounded grains. A detailed description of these can be found in previous chapter.

Sample name	Weight percent			Sorting Index	Sphericity	Roundness
	36–56 µm	56–106 µm	106–256 µm			
S-0	0	0	100%	0.13	0.80	0.90
S-1	0	30%	70%	0.46	0.70	0.82
S-2	0	70%	30%	0.47	0.72	0.79
S-3	0	50%	50%	0.42	0.72	0.82

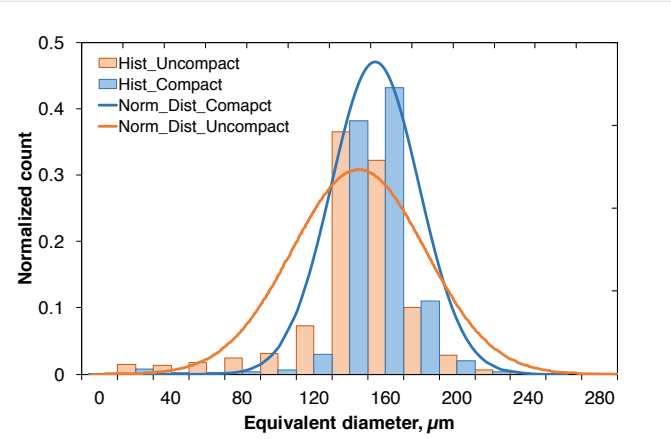

Figure 3.4: Grain size distribution by count before (orange) and after (blue) compaction following the measurement sequence shown in Figure 3.2b.

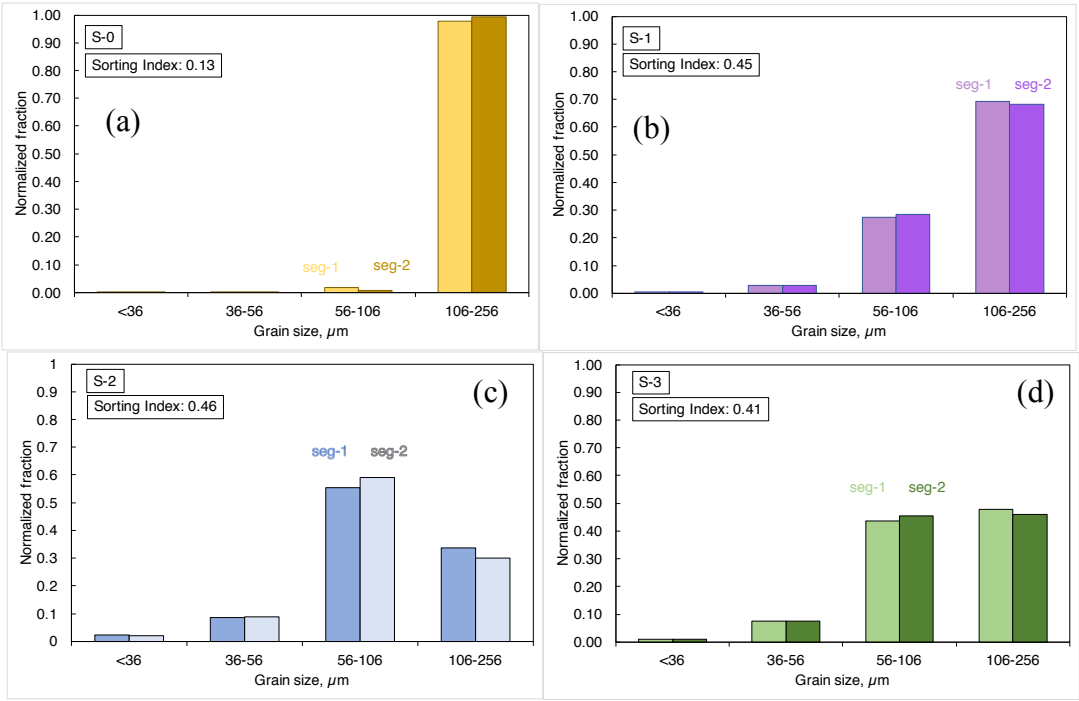

Figure 3.5: Grain size distribution by weight after compaction following the measurement sequence shown in Figure 3.2b for samples (a) S-0, (b) S-1, (c) S-2 and (d) S-3. The two segments seg-1 and seg-2 are the two almost equal halves of the samples used for representative elementary volume (REV) analysis of the whole image (Details are in previous chapter).

Grain size distribution by weight (Figure 3.5a) in S-0 shows no grain crushing as almost all the grains are 106–256 μm in equivalent diameter. On the contrary, samples S-1, S-2 and S-3 (Figures 3.5b, c and d) have more small grain size fractions than they had during preparation. This discrepancy can be related to the approach we are adopting in the calculation of the equivalent diameter, where grain volume is being used rather than any physical diameter in any directions. The equivalent diameter referring to the grain size in this study is the diameter of an equivalent sphere that has the same volume as the grain. In sieving, an elongated large grain can pass through the mesh by its smaller axis, hence misrepresenting the grain size distribution calculated using the grain volume from micro-CT images. Another possible explanation could be that the grains, being more angular in these three samples, tend to crush more easily at their sharp edges during increasing stress.

3.7. Friction term used in previous studies

We have found the usage of similar terms to 'fraction of no slip contacts' in two previous studies. Duffaut et al. 2010 modify this α term as a function of the friction coefficient of the grain following the partial slippage assumption from the HM model. This frictional parameter, termed as $f(\mu)$, is equal to the power of one-third of α. As a result, it always provides higher values than α except at the two ends 0 and 1, where they are the same. For this reason, in our case, effective shear modulus will be certainly over-predicted by $f(\mu)$ as long as the effective bulk modulus fits well with the model.

While both of these parameters act only on the tangential stiffness of the grain contact, the weight factor, w, introduced by Saul et al. (2013) acts on the entire effective shear modulus of the HM or Walton no slip model, whereas the equation for effective bulk modulus remains unchanged. Similar to α, w is dependent on neither porosity nor pressure and can be expressed by the effective elastic property of the pack and the elastic constants of the grain. It always has higher values than α as it is applied to the entire effective shear modulus rather than only on the tangential stiffness term. For the same reason, this w can cover the effective Poisson's ratio of the pack from 0 to 0.5. In other words, this weight factor from 1 to 0 covers the V_P/V_S ratio of the granular pack starting from ~1.41 asymptotically to infinity, respectively. This means unlike α, it can deal with a V_P/V_S ratio higher than 1.73. In our understanding, as both the normal and tangential stiffness are affected simultaneously in the effective shear modulus by applying a weight factor, another factor should be applied to the effective bulk modulus rather than leaving it unchanged. We present a graph to compare these factors with the V_P/V_S ratio of the pack in Figure 3.6.

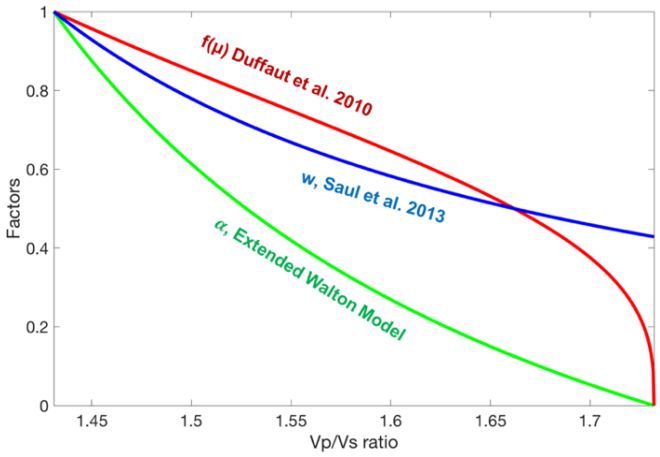

Figure 3.6: Fraction of no slip contacts, α from extended Walton model (green); friction parameter, f(μ) from Duffaut et al. (2010) and weight factor, w from Saul et al. (2013). Poisson's ratio of the grain considered here as 0.20.

3.8. Results and Analysis

3.8.1. Ultrasonic measurement

Figure 3.7 shows both P and S wave velocities in all samples are increasing with applied stress. Both of the velocities are higher in S-0 than the other three samples. This is due to the higher C and contact surface area, both of which are actually governed by the grain shape factors and sorting index. Grains in S-0 are more spherical, rounded and well sorted than the grains in S-1, S-2 and S-3 (Table 3.1). An extensive description of these effects has been provided in the previous chapter.

As expected, all the samples show velocities increasing with decreasing porosity (Figure 3.8a and 3.8b). The change in porosity is 2–3% over the applied stress range from its initial porosity at 3.15 MPa. Figure 3.9a and 3.9b show that the V_P/V_S ratio is decreasing with decreasing porosity and increasing stress in all the samples. One remarkable observation is that the range of V_P/V_S ratios throughout the stress range is narrower in S-0 than in the other three samples. The reason may lie in the fact that S-0 has very well-sorted and spherical, rounded grains compared with the other three samples, which have poorly sorted and more angular, less rounded grains. During the compaction, the refined loading-unloading cycle prior to the virgin loading phase

seemingly works well in keeping V_P/V_S ratios below 1.7321 in three of the four samples.

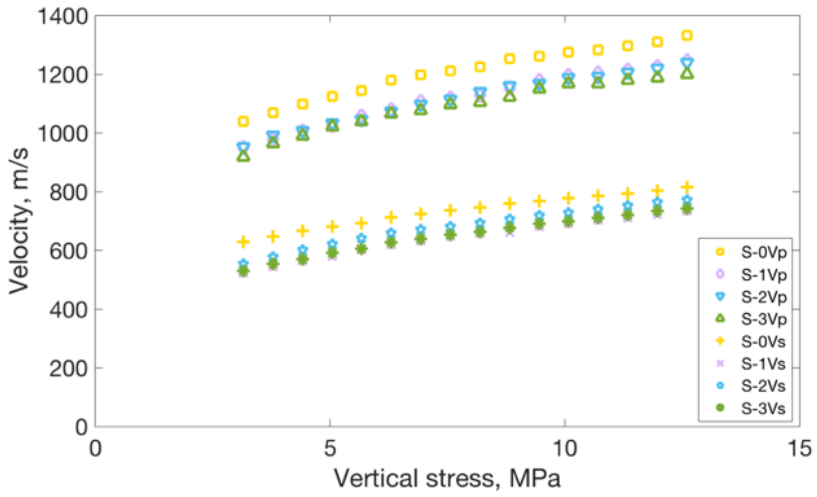

Figure 3.7: P and S wave velocities for sample S-0, S-1, S-2, and S-3 dependence on vertical stress.

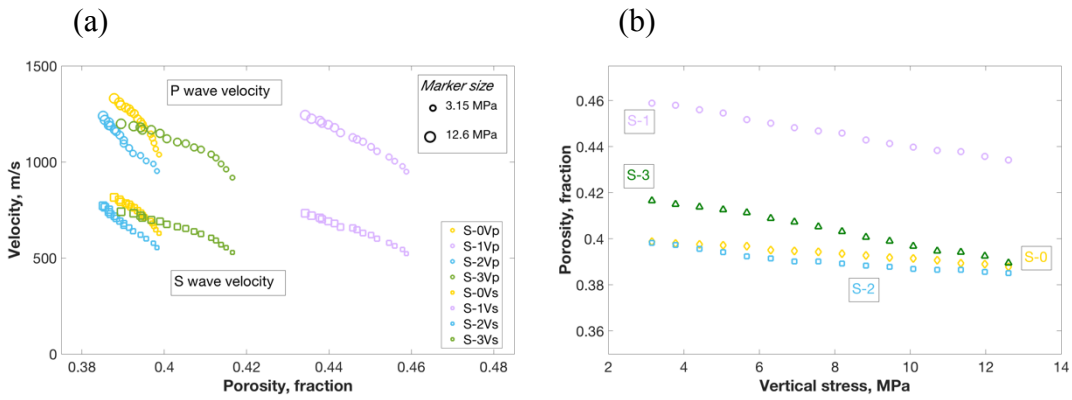

Figure 3.8: (a)Measured P and S wave velocities as a function of porosity. Marker size increases with increasing vertical stress from 3.15 to 12.6 MPa. (b) Porosity plotted as a function of vertical stress.

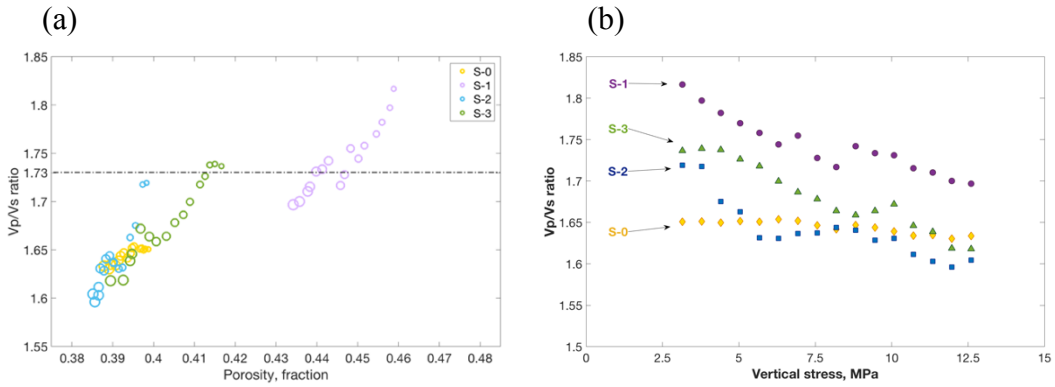

Figure 3.9: (a)Ratio between P and S wave velocities vs. porosity. Marker size increases with increasing vertical stress from 3.15 to 12.6 MPa. The dashed line indicates V_P/V_S ratio equal to 1.73, which corresponds to fraction of no slip contacts, α equal to 0. (b) Velocity ratios plotted as a function of vertical stress.

3.8.2. Coordination number and porosity of the samples

We calculate coordination number C from the micro-CT images using voxel-based processing techniques. Figure 3.10 shows the normalised fraction of the histogram of C in all the samples and average Cs are in the inset. Changes in C with respect to changes in stress and porosity are well documented in both numerical simulations by Makse et al. (2004) (in equation 29) and empirical equations from Zimmer et al. (2007) (in equation 8), which summarised a porosity-C table (Mavko et al. 2009) based on different datasets compiled by Murphy (1982). As we are going to use a constant C value that corresponds with the end stress at 12.6 MPa, it is necessary to investigate how it could have changed during the loading phase started from 3.15 MPa. To do that, we calculate Cs using both Makse et al. (2004) and Murphy (1982) in our samples. None of the results show significant changes in the Cs with applied stress and porosity changes. Calculation using the equation from Makse et al. (2004) shows an increase of C only by 0.3 with applied stress increases from 3.15 to 12.6 MPa (Figure 3.11a). Cs calculated using Murphy (1982) show the highest increase in C, by 0.6 for sample S-3 (Figure 3.11b). To visualise in a single graph, we put the results from Murphy (1982) according to their corresponding stress values in Figure 3.11a with the Cs calculated from Makse et al. (2004).

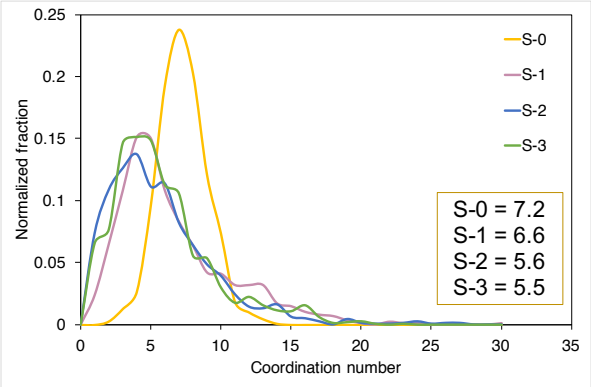

Figure 3.10: Histogram of the coordination number in the four samples expressed as normalised fraction. Inset shows the average coordination number for the four samples.

We observe that the C of S-0 obtained from the micro-CT image is closer to the C calculated using Makse et al. (2004), whereas for other three samples, the Cs are lower. The possible reason is sample S-0 has well-sorted, more spherical and rounded grains whereas the other three have poorly sorted and less spherical and rounded grains. These shape characteristics of the grains bear much closer resemblance to the same-sized spheres used in the numerical simulation by Makse et al. (2004). Cs calculated from Murphy (1982) are found much higher than those calculated from micro-CT image.

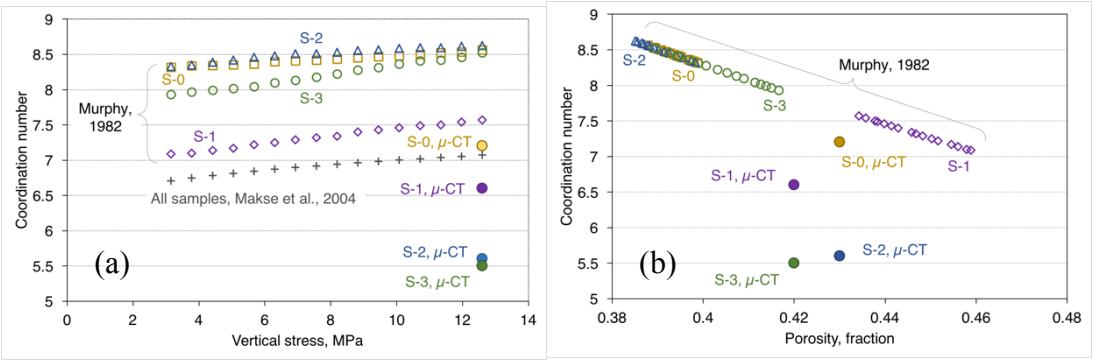

Figure 3.11: (a) Coordination number changes with applied vertical stress obtained from empirical relationships by Murphy (1982), numerical simulations by Makse et al. (2004), and from micro-CT image analysis obtained in this work at the stress of 12.6 MPa. (b) Coordination number vs porosity obtained from Murphy 1982, and micro-CT image analysis. Note that Makse et al. (2004) simulations are for hydrostatic pressure.

We calculate porosity from the volume of the total space inside the sample chamber and the volume of the grains. The volume of the grains is calculated from the mass of the sample and the density of quartz as 2.65 g/cm^3. We are also able to calculate porosity at the end stress of 12.6 MPa from the micro-CT images. After noise reduction of the image, a thresholding based on the histogram of the gray scale values of all the voxels can provide a binary image that has grains and pore spaces as separate phases labelled as 1 and 0 respectively. The total number of 0 voxels as a fraction of the total number of image voxels gives the porosity value. Porosities from these two different techniques in all the samples have differences as little as 2 to 4% (Figure 3.11b).

We note that in further calculations we are using porosities measured in the experiment (not obtained from micro-CT images) at each corresponding stress level. As the changes in C with stress using Murphy (1982) and Makse et al. (2004) are small, in our future analysis in this paper we use an individual constant C for individual samples.

3.8.3. Fraction of no slip contacts

α calculated from V_P/V_S ratio in our samples using Eq. 3.13 has lower and upper limits corresponding to the grain's Poisson's ratios 0 and 0.35 (Figure 3.12a) respectively. Some of the velocity ratios at initial stress levels in S-1, S-2 and S-3 are higher than 1.73, which results in the calculated α having non-physical negative values. Sample S-1 has higher porosity values than the other three samples and the majority of the measurements from the starting stress level show a V_P/V_S ratio higher than 1.73 (Figure 3.12b). In our understanding, a V_P/V_S ratio of 1.73 should be related to the critical porosity (Nur et al. 1998) concept where all the grains are unstable, which replicates the situation of total slippage of all the grains or, in other words, the fraction of 'no slip' is 0.

(a)

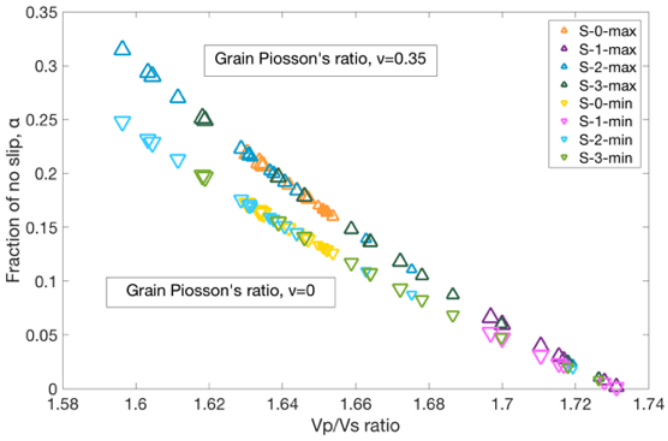

(b)

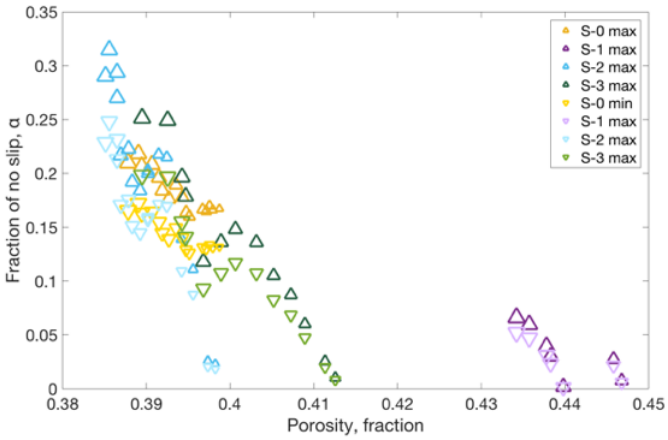

Figure 3.12: Fraction of no slip contact, α calculated for Poisson's ratio of the grain 0 and 0.35 with (a) V_P/V_S ratio and (b) porosity. Marker size increases with increasing vertical stress from 3.15 to 12.6 MPa.

3.8.4. Forward modelling

Uniaxial stress applied to our sample may result in the possible development of anisotropy inside the samples. It is likely such induced anisotropy will be TI type. As the velocity measurements are performed only in the direction of the applied stress, it is not possible to obtain all five stiffness constants, which could otherwise provide the anisotropic parameters. Rather, using equations 3.6 and 3.7, we calculate the stiffness constants in the direction of wave propagation assuming the grain's elasticity as of quartz: shear modulus as 44 GPa and Lamé's first parameter as 8 GPa (Mavko et al. 2009). Both of the stiffness constants C_{33} and C_{44} calculated at no slip and total slip cases bound the respective constants calculated from the velocity data (Figure 3.13). Comparing these constants with the isotropic model, we have found, as expected, that

both of the constants have lower values in the TI model. C_{33} in the isotropic model are 1.20 and 1.08 times higher for no slip and total slip cases, respectively, than those constants in the TI model (Figure 3.13a). On the other hand, C_{44} for isotropic case are 1.69 and 2.89 times higher (Figure 3.13b). It is important to mention that in the experiment, we do not have a perfect uniaxial compaction. The sample is inside a confined chamber where two of the principal stresses in lateral directions (along the isotropic plane) are not zero. According to this situation in the sample, both of the stiffness constants should become higher than they are calculated using TI models. As a result, they approach the values calculated from the isotropic model. For this reason, the confinement state of the sample during uniaxial stress would have very little impact on the calculations based on the hydrostatic model. Moreover, as the term fraction of no slip contact, α is well established in the isotropic model and both of these models bound the dynamic data (Figure 3.13), we will apply the hydrostatic model in our calculation to obtain the elastic properties of the grains.

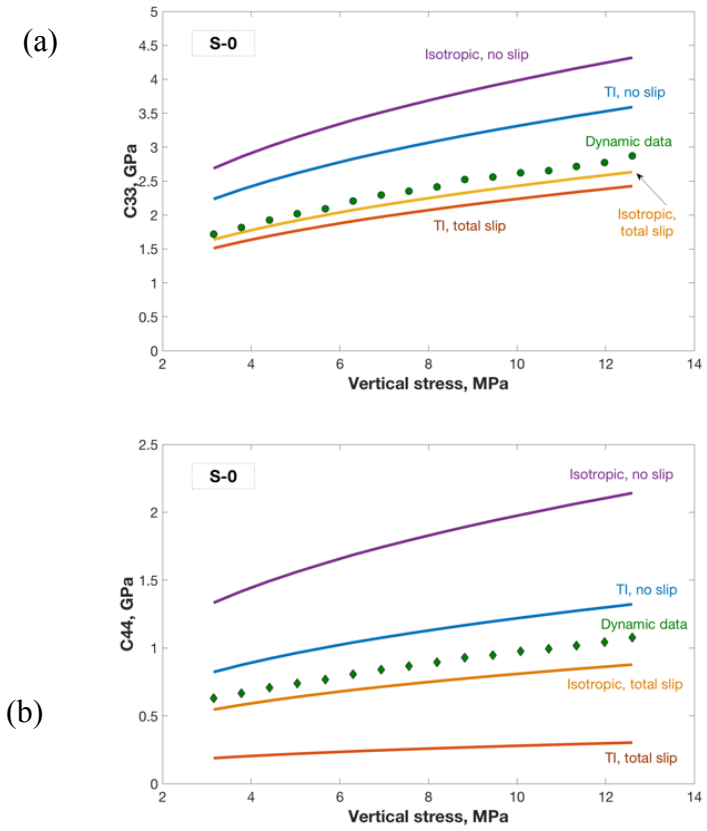

Figure 3.13: Stiffness constants (a) C_{33} and (b) C_{44} in sample S-0 following isotropic and transversely isotropic (TI) models assuming total slip and no slip between the grain contacts. Dynamic data calculated from the velocities shown in green.

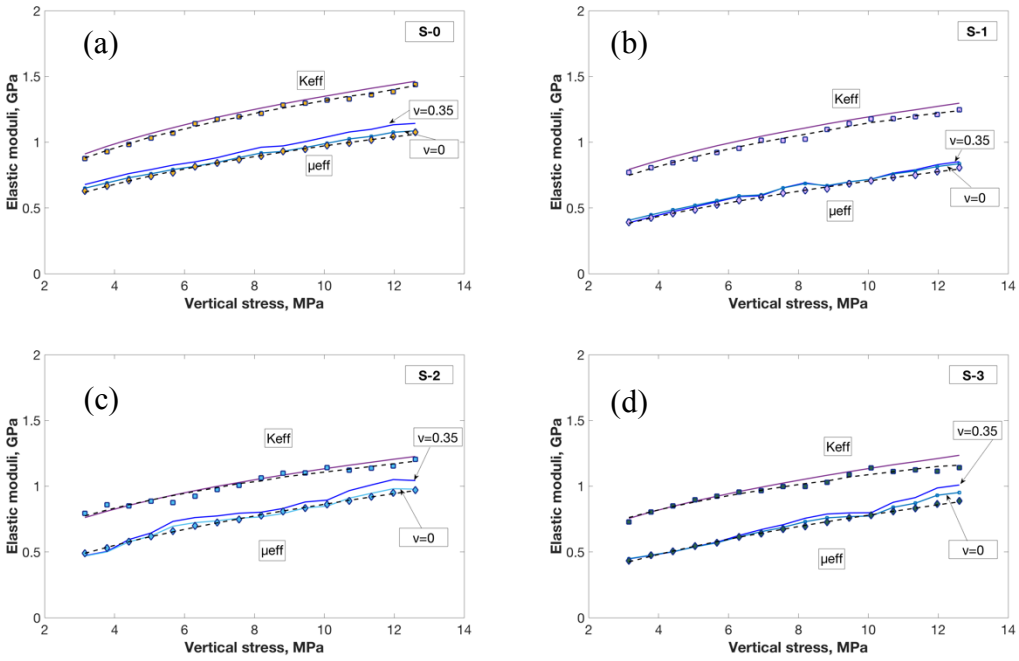

Figure 3.14: Forward modelling using the parameters from the experiment, micro-CT image analysis and typical quartz elastic constants in samples (a) S-0, (b) S-1, (c) S-2 and (d) S-3. Solid lines are from the models and dashed lines are the best fit to the dynamic data shown as points. Deep and light blue solid lines in effective shear modulus are for Poisson's ratio of the grains 0.35 and 0 respectively.

To check how two of the key parameters C and α help in matching the hydrostatic model with the dynamic data, we prepare models (Figure 3.14) using Eqs 3.1 and 3.2. All the samples have a fairly good match between the model and the dynamic data. Calculated Cs from the micro-CT images are found to be very effective in predicting effective bulk modulus in all the samples. As fraction of no slip contacts, α is calculated from the dynamic data itself, the upper and lower limits of the effective shear moduli match well with the effective shear modulus from the dynamic data. In poorly sorted samples S-1, S-2 and S-3, some of the initial data points at low stresses have V_P/V_S ratio greater than 1.731, which gives negative α values. As a result, depending on the magnitude of the negative α, we see a flip over between the upper and lower limits of the effective shear modulus in the model.

3.8.5. Elastic parameters of the constituent grain and their no slip contacts

Using the methodology described in section 3.2.1, we calculate the upper and lower limits of the shear modulus of the grain assuming its Poisson's ratio as 0 and 0.35 respectively. Figure 3.15 shows all results for four samples, where S-1, S-2 and S-3 do not have values plotted in the initial stress levels. As α at these stresses are negative or close to zero, the inverted results give erratic values. For this reason, we intend to omit those in our calculation. The upper and lower limits of the calculated shear modulus bound the actual shear modulus of quartz (Mavko et al. 2009) in all the samples (Figure 3.15). To determine a single upper and lower limit for each sample, we prepare the normal distribution (Figure 3.16) of the calculated results presented in Figure 3.15. The peaks of the curves that represent the limits bound the actual shear modulus shown as a dotted vertical line. We constrain these peak values as upper and lower limits in the non-linear least square solution of Eq. 3.2 to obtain the shear modulus (Figure 3.17a) and Poisson's ratio (Figure 3.17b) of the grain. Both of these elastic parameters are close to the actual values found in the literature.

We also calculate the α values from the elastic parameters of the grain and the V_P/V_S ratio of the sand pack at each stress. Figure 3.18 shows all the α values ranging from 0.001 to 0.26 in all four samples at their corresponding stresses. For individual samples, the α value has the least change in S-0 as it has the least change in V_P/V_S ratio. Note that, in Figure 3.12a, the α values are calculated from the two ends of the Poisson's ratio values namely 0 and 0.35 whereas here at Figure 3.18, the α values are calculated from the elastic properties of the constituent minerals obtained from the methodology described in this chapter.

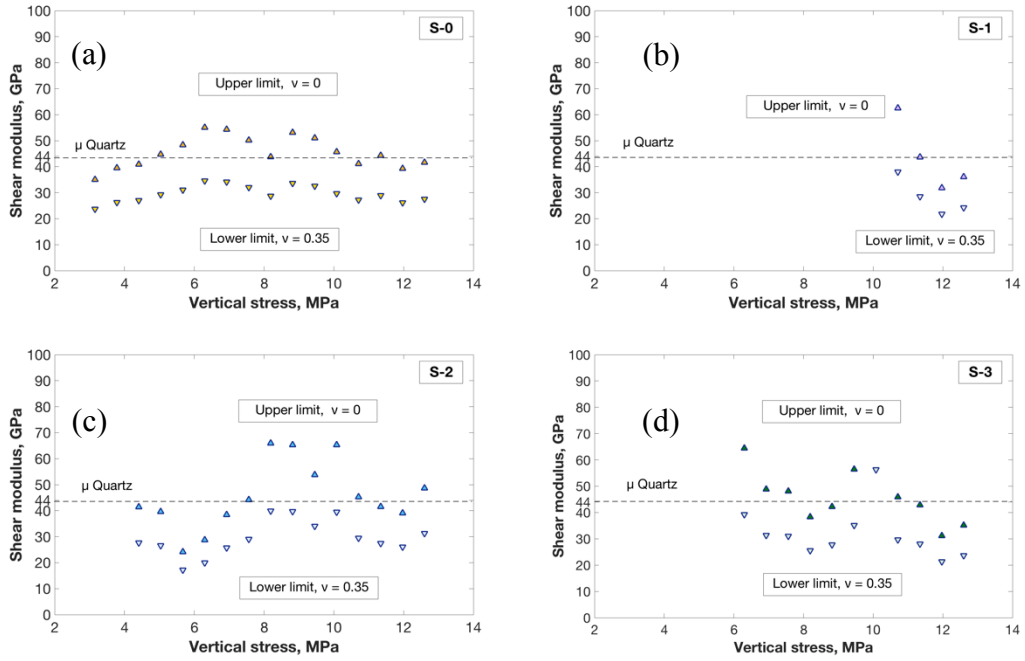

Figure 3.15: Shear modulus of the grains calculated from the dynamic data using α values for Poisson's ratio of the grain 0 and 0.35 in the samples (a) S-0, (b) S-1, (c) S-2 and (d) S-3. The dashed line is the actual shear modulus of quartz. At low stress levels, the samples S-1, S-2 and S-3 have non-physical α values negative or close to zero, which gives unacceptable shear modulus, hence they are omitted.

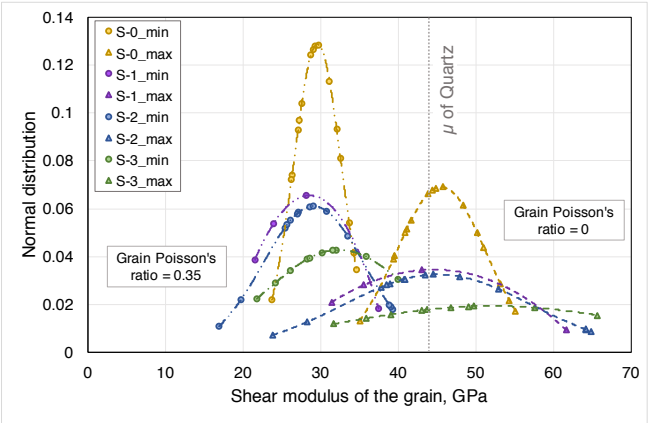

Figure 3.16: Normal distribution of the shear modulus of the grain in all samples that show the upper and lower range.

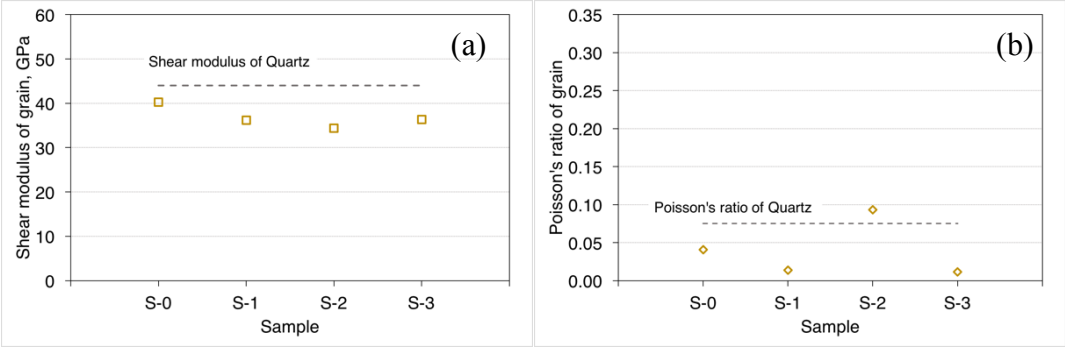

Figure 3.17: Calculated non-linear least square solution for (a) shear modulus and (b) Poisson's ratio of the grain after applying the constraint from the upper and lower range of the shear modulus. Dashed lines are the actual values.

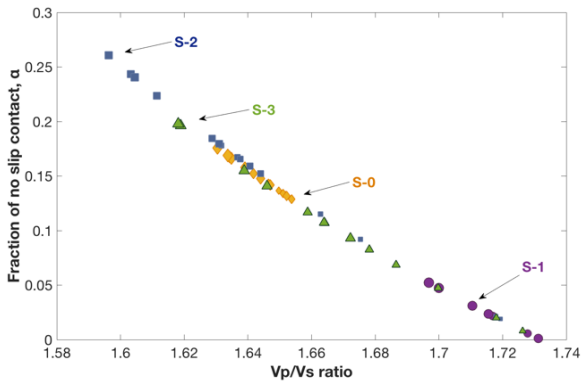

Figure 3.18: Fraction of no slip contact (α) against V_P/V_S ratio for all the samples. Marker sizes indicate the stress level, the smallest and largest marker among all the samples represent 3.15 and 12.6 MPa respectively.

3.9. Discussion

3.9.1. Significance of experiment procedure

Experimental technique plays a significant role in successfully implementing the methodology described in this chapter. The extent of the stress range can affect the grain damage. Moreover, the number and extent of loading–unloading phases have an impact on grain settling. We can further refine the technique described here by lowering the top stress, which essentially provides very little change in the V_P/V_S ratio over the stress range. Thus calculated α can be nearly constant which could be in accordance with the extended Walton model. Additionally, the low stress limit can avoid the deviation from the 1/3 power law of the Walton model during higher stress levels in the virgin loading phase. On the contrary, we have to keep in mind that the top stress should not be reduced too much so that the V_P/V_S ratio may remain higher than 1.731. We can also increase the number of sampling intervals, taking more ultrasonic measurements within this stress range so that the increased data can help find more accurate results in the non-linear least square solution.

3.9.2. Micro-CT images for C

Micro-CT images can provide C with greater precision, which are valuable to apply in the models. Moreover, Cs from the micro-CT image analysis can resolve confusion between the empirical results and numerical simulations. We have seen that grain shape factors and sorting have a big impact on the microstructure of the pack and eventually control the dynamic effective elastic moduli. Poorly sorted samples with less spherical and rounded grains have lower ultrasonic velocities than the well-sorted samples with grains of higher sphericity and roundness.

3.9.3. Effect of stress in α

An important aspect we observe is that α increases with increasing stress and decreasing porosity, whereas the model asserts it should be constant. It is obvious that the increasing V_P/V_S ratio with increasing stress is the reason, as α is calculated from this ratio. Most of the experimental results report a similar trend in velocity ratios with increasing pressure (Zimmer 2003) and uniaxial stress (Bhuiyan and Holt 2016).

Duffaut et al. (2010) argue that the increasing pressure causes the increment of internal frictional resistance or shear strength that facilitates this rising trend away from the model. On the other hand, a number of studies (e.g. Liu et al. 1995 and Howell et al. 1999) point out that force chains provide the principal supporting structure in a granular medium for static and dynamic loading. From their photo-elastic experiment, Owens and Daniels (2011) mention that the force chain network plays a key role in seismic wave propagation in a granular medium. They argue that the change in both coordination number and force chain networks while increasing pressure are the potential reasons behind this issue. Huang and Daniels (2016) follow a concept that the force chain network is composed of a number of groups of particles, termed as community, which are connected with each other. Using numerical simulation, they find that the average community size, network force, and hull ratio (that describes the dispersity of the grains in a community) are highly controlled by the friction coefficient and the pressure. For any given friction coefficient of the grains, increasing pressure increases the average size of the community.

In our samples, we observe that coordination numbers calculated by numerical simulation (Makse et al. 2004) and empirical relationships (Murphy 1982) change little as a result of the applied stresses and porosity reduction. On the other hand, Zimmer (2013) observes that the rate of increasing S wave velocity with increasing pressure is slightly higher than that of P wave velocity. This means that even though both of the velocities are increasing with increasing pressure, due to a higher increment rate in S wave velocity, the V_P/V_S ratio falls slightly. Thus we speculate there may be a causal effect between increasing coordination number and possible increase of contact surface area resulted from pressure increment and the higher rate of increment of S wave velocity than that of P wave velocity. Moreover, grain shape and sorting can affect the rate of change in velocity ratio throughout the stresses. The well-sorted and more spherical and rounded grains in S-0 result in less change whereas the other three angular and poorly sorted samples have more changes in velocity ratios. With increasing stress, the force chain network in the samples of poorly sorted and angular grains (S-1, S-2 and S-3) are likely to change more than the samples of well-sorted and rounded grains (S-0). Hence the community size is expected to become much larger at the final stress than its initial size at S-1, S-2 and S-3. We think the grain shape factors and contact surface areas together with the topology and magnitude of

the force in the network are responsible for the rising trend in velocity ratios rather than the stable trend in the models, which readily overlook these phenomena.

3.9.4. Comparing calculated α with previous studies

The resultant α values presented in Figure 3.18 are very similar to most of the previous studies. Bachrach and Avseth (2008) estimate α values of 0.07 and 0.35 from shear wave sonic logs in a shallow gas well and a deep water Gulf of Mexico well respectively. They mention that the increase of α value in the deeper sediments is due to the increase of pressure with depth. This is also similar to our findings where α values, which have marker sizes corresponding to the stress in Figure 3.18, show an increasing trend with increasing stress. Dutta et al. (2010) use an arbitrary constant α of 0.6, which is significantly higher than our results. Along with this parameter, they use two separate Cs in the model to predict P and S wave velocities in a Pomponio Beach sand sample measured by Zimmer (2003). Following our methodology, the V_P/V_S ratio of around 1.66 in that sample gives the α value of around 0.15, which is in accordance with typical values. Taking the P wave coordination number (assuming no new contacts are added during increasing pressure) and similar grain elasticity assumed in that study, the extended Walton model with α value of around 0.15 matches well with both of the effective bulk and shear moduli of the dynamic data in that sample.

3.9.5. Effective medium model for grain elasticity

In our methodology, we tackle the longstanding problem of predicting effective shear modulus using contact-based models based on the effective medium theory by implementing α of the extended Walton model calculated from the dynamic data itself. The pivotal point is to obtain a good match between the effective bulk moduli calculated from dynamic and model data. Appropriate C is the crucial parameter needed in order to do this. As long as there is a perfect match in effective bulk moduli, the effective shear moduli will always be a good match and, consequently, the calculated elastic parameters are much more likely to be close to the actual values.

3.10. Conclusion

We have developed a controlled and simple laboratory technique to obtain the elastic parameters of grains from the dynamic elastic moduli of their pack. We are able to predict dynamic effective bulk moduli with Walton's (1987) model using a real coordination number (C) from the micro-CT image. Then, implementation of fraction of no slip contacts obtained from the ultrasonic measurements gives a good match between the model and dynamic effective shear moduli. Introducing these parameters into the inverted form of the extended Walton model, we are able to obtain both the upper and lower limits of the elastic parameter of the grains. Finally, by constraining these upper and lower values into the non-linear least square solution, we obtain the elastic parameters of the grains and the fraction of no slip contacts. Thus, calculated parameters have been found very much in accordance with the actual elastic parameters.

Our technique can be a first step in obtaining the elastic properties of the hard and crystalline rocks, with limited anisotropy, from the fragmented powder that comes up during drilling. This technique can also be applied to the unconsolidated sand samples from potential reservoirs to get the elastic properties of the solid phase, which is a key parameter for rock physics characterisation and fluid substitution.

3.11. Acknowledgements

The work has been supported by the Deep Exploration Technologies Cooperative Research Centre, whose activities are funded by the Australian Government's Cooperative Research Centre Programme. This is DET CRC document 2017/1061. The authors also express their gratitude to the ASEG Research Foundation for sponsoring them with Grant (RF16M04). ZA was supported by a Curtin International Postgraduate Research Scholarship and Australian Government Research Training Program Scholarship. The authors deeply appreciate the help from Professor Boris Gurevich for valuable discussions and Alexey Yurikov for helping with least square solutions.

3.12. References for Chapter 3

Ahmed, Z., Lebedev, M., Madadi, M. & Uvarova, Y. 2016. Inverting Dynamic Elastic Moduli of a Granular Pack to Get Shear Modulus of the Grain. In: ASEG-PESA-AIG 2016, 25th Geophysical Conference and Exhibition, pp. 944-948.

Ahmed, Z. & Lebedev, M. 2018. Elastic properties of sands, Part 1: Micro computed tomography image analysis of grain shapes and their relationship with microstructure. Geophysical Prospecting. doi: 10.1111/1365-2478.12652

Bachrach, R. & Avseth, P. 2008. Rock physics modeling of unconsolidated sands: Accounting for nonuniform contacts and heterogeneous stress fields in the effective media approximation with applications to hydrocarbon exploration. Geophysics 73, E197-E209.

Bhuiyan, M.H. & Holt, R.M. 2016. Variation of shear and compressional wave modulus upon saturation for pure pre-compacted sands. Geophysical Journal International 206, 487-500.

Brandt, H. 1955. A study of the speed of sound in porous granular media. J. Appl. Mech. 22, 479-486.

Digby, P. 1981. The Effective Elastic Moduli of Porous Granular Rocks. Journal of Applied Mechanics 48, 803-808.

Domenico, S.N. 1977. Elastic properties of unconsolidated porous sand reservoirs. Geophysics 42, 1339-1368.

Duffaut, K. & Landrø, M. 2007. Vp:Vs ratio versus differential stress and rock consolidation — A comparison between rock models and time-lapse AVO data. Geophysics 72, C81–C94.

Duffaut, K., Landro, M. & Sollie, R. 2010. Using Mindlin theory to model friction-dependent shear modulus in granular media. Geophysics 75, E143–E152.

Dutta, T., Mavko, G. & Mukerji, T. 2010. Improved granular medium model for unconsolidated sands using coordination number, porosity, and pressure relations. Geophysics 75, E91-E99.

Gallop, J. 2013. Extended Walton third-order elastic coefficients modified by an anisotropic and stress-dependent coordination number. Geophysics 78, D545-D556.

Goddard, J.D. 1990. Nonlinear elasticity and pressuredependent wave speeds in granular media. Proceedings of the Royal Society of London, Series A, Mathematical and Physical Sciences 430, 105-131.

Hertz, H. 1882. On the contact of rigid elastic solids and on hardness. Macmillan Paper 6.

Howell, D., Behringer, R.P. & Veje, C. 1999. Stress fluctuations in a 2D granular couette experiment: A continuous transition. Physical Review Letters 82, 5241-5244.

Huang, Y. & Daniels, K.E. 2016. Friction and pressure-dependence of force chain communities in granular materials. Granular Matter 18.

Jenkins, J., Johnson, D., La Ragione, L. & Makse, H. 2005. Fluctuations and the e&ective moduli of an isotropic, random aggregate of identical, frictionless spheres. Journal of the Mechanics and Physics of the Solids 53, 197-225.

Johnson, D., Schwartz, L., Elata, D., Berryman, J., Hornby, B. & Norris, A. 1998. Linear and Nonlinear Elasticity of Granular Media: Stress- Induced Anisotropy of a Random Sphere Pack. Journal of Applied Mechanics 65, 380-388.

Koochak Zadeh, M., Mondol, N.H. & Jahren, J. 2016. Experimental mechanical compaction of sands and sand-clay mixtures: a study to investigate evolution of rock properties with full control on mineralogy and rock texture. Geophysical Prospecting 64, 915-941.

Liu, C.-h., Nagel, S.R., Schecter, D.A., Coppersmith, S.N., Majumdar, S., Narayan, O. & Witten, T.A. 1995. Force Fluctuations in Bead Packs. Science 269, 513-515.

Madadi, M., Bona, A., Lebedev, M. & Gurevich, B. 2015. Estimation of grain elasticity properties from ultrasonic measurements on dry granular pack. In: 3rd International Workshop on Rock Physics.

Makse, H.A., Gland, N., Johnson, D.L. & Schwartz, L. 2004. Granular Packings-Nonlinear elasticity, sound propagation and collective relaxation dynamics. Phys. Rev. E 70, 061302.

Makse, H.A., Gland, N., Johnson, D.L. & Schwartz, L.M. 1999. Why Effective Medium Theory Fails in Granular Materials. Physical Review Letters 83, 5070-5073.

Mavko, G., Mukerji, T. & Dvorkin, D. 2009. The Rock Physics Handbook, Second Edition Tools for Seismic Analysis of Porous Media. CAMBRIDGE UNIVERSITY PRESS, ISBN ISBN-13 978-0-511-65062-8, ISBN-13 978-0-521-86136-6.

Mindlin, R.D. 1949. Compliance of elastic bodies in contact. Journal of Applied Mechanics 16, 259-268.

Murphy, W. 1982. Effects of microstructure and pore fluids on the acoustic properties of granular sedimentary materials. In: PhD dissertation.

Norris, A. & Johnson, D. 1997. Nonlinear elasticity of granular media. Journal of Applied Mechanics 64, 39-49.

Nur, A., Mavko, G., Dvorkin, J. & Galmudi, D. 1998. Critical porosity- A key to relating physical properties to porosity in rocks. The Leading Edge 17, 357-362.

Owens, E.T. & Daniels, K.E. 2011. Sound propagation and force chains in granular materials. EPL (Europhysics Letters) 94, 54005.

Sain, R. 2010. Numerical simulation of pore-scale heterogeneity and its effects on elastic, electrical and transport properties. In: Department of Geophysics, Vol. PhD thesis. Stanford University.

Sava, D. & Hardage, B. 2006. Rock physics characterization of hydrate-bearing deepwater sediments. In: Seg/New Orleans 2006 Annual Meeting, Vol. Expanded Abstracts, pp. 1913-1917.

Walton, K. 1987. The effective elastic moduli of a random packing of spheres. J. Mech. Phys. Solids 35, 213-226.

Winkler, K. 1983. Contact stiffness in granular porous materials: comparison between theory and experiment. Geophysical Research Letters 10, 1073-1076.

Yin, H. 1992. Acoustic velocity and attenuation of rocks, Isotropy, intrinsic anisotropy, and stress-induced anisotropy. In: Department of Geophysics, Vol. PhD. Stanford University.

Zimmer, M., Prasad, M., Mavko, G., and Nur, A.. 2007. Seismic velocities of unconsolidated sands: Part 1- Pressure trends from 0.1 to 20 MPa. Geophysics 72, E1-E13.

Zimmer, M.A. 2003. Seismic velocities in unconsolidated sands: measurements of pressure, sorting, and compaction effects. In: Department of Geophysics, Vol. PhD thesis. Stanford University.

4. Elastic Properties of Hard Rock Core Sample Calculated from the Ultrasonic Velocities of its Powder Collected During Drilling

4.1. Abstract

Elastic properties of rocks are crucial parameters to delineate the distribution of subsurface deposits with the aid of geophysical methods. Rock powders that come up from penetrating hard rocks during mineral exploratory drilling can be a suitable source to obtain such elastic properties. Laboratory measurements of ultrasonic velocities at different stress levels through such dry, unconsolidated powder samples can provide their effective elastic properties, which can further be inverted to obtain the elastic properties of the constituent grains following Hertzian contact models that are proposed based on Effective Medium Theory. Most of the contact models are developed considering single mineral with the same elastic properties as constituent grains. In this study, we incorporate multiple mineral phases to calculate effective Young's modulus of the mineral composite, while they are in contact, by using the Hertzian contact approximation. This effective Young's modulus of the mineral composite, calculated from each mineral fraction present in the sample, are found to be lower than those calculated from the ultrasonic velocities of the corresponding core samples. Later we use this effective Young's modulus in the contact model which can provide close values of the elastic moduli of the grains compared with those calculated from the ultrasonic velocities of the core samples. Subsequent seismic wave velocities of the grains show little difference with the ultrasonic velocities measured on the corresponding core sample. The presented technique can be helpful in determining the elastic properties or seismic wave velocities of hard rock formations of which the core samples are not available.

4.2. Introduction

Solid core samples extracted during drilling provide significant, reliable micro- and mesoscale properties of the subsurface formations. Direct laboratory measurements of these physical and mechanical properties of the core samples can be key inputs in characterising rock formations. However, extraction of solid core samples is costly and time consuming. Sometimes, adverse field conditions may mean the logistic support to carry out this sort of operation is unavailable. Moreover, in the case of unconsolidated or fragile formations, most of the time it is hard to collect intact core samples, as they might be broken. In contrast, rock fragments or powders are the usual product of traditional drilling during mineral exploration in a hard rock environment. Laboratory measurements on dry rock powders can be time efficient and cost effective. In this study, our aim is to calculate the elastic properties of solid cores from ultrasonic measurements on their powders.

The elastic properties of unconsolidated sediments is an active field of research due to its application in near surface geophysics (Bachrach et al. 2000), shallow hydrocarbon reservoirs in deep water settings (Saul 2014) and gas hydrate bearing sediments in deep ocean bottom (Helgerud et al. 1999). These properties are significantly controlled by the mineralogy of individual grains, which may have a range of values in their elastic properties. For rock physics characterization of these sediments, detailed knowledge of the effective elastic properties of the composite minerals is required. In most cases either the elasticity of the mineral quartz or an approximation of the upper and lower bounds are used. Although these techniques are adequate for *ad hoc* situations, in many instances where a variety of minerals that have different elasticities are present, they are unlikely to provide reasonable results.

Contact-based models (a brief description is in Chapter 3) are widely used to characterise the elastic properties of a pack of granular materials. All these models rely on the assumption that the constituent minerals are an identical spherical shape with the same elasticity. Dvorkin et al. (1999) pointed out that the effective elastic constants of the dry sediment-frame largely depend on the elastic constants of the solid phase along with porosity and effective pressure. Berryman (1995) had a concise description of different theories used in calculating physical properties of the rocks that are

mixture of assorted minerals. To calculate the elasticity of a solid phase that contained a number of minerals, upper and lower bounds were frequently used. Voigt (1928) calculated the effective elastic properties of composite minerals, considered as the upper bound, under an assumption that the strain is uniform everywhere inside the mineral aggregate. On the other hand, the lower bound (Reuss 1929) was calculated under an assumption that the applied stress was uniform everywhere. Both of these bounds were calculated from the amount of each mineral present and their respective elastic constants. As these bounds were quite wide, Hill (1952) proposed the average of Voigt's upper bound and Reuss' lower bound, known as the Voigt-Reuss-Hill average. Hashin and Shtrikman (1963) presented the narrowest bound, which used each mineral fraction present and its respective elastic constants. The distance between the bounds largely depended on how variegated the elastic constants of individual minerals in the mixture were. The narrowest distance resulted from the minerals that have close elastic constant values and vice versa. Hossain et al. (2011) calculated the effective Young's modulus of two minerals that were in Hertzian contact (Hertz 1882) by following the equation presented in Johnson (1985). Then they approximated the effective Young's modulus of the mixture of two minerals that had three combinations of contacts between them. Sriram et al. (2014) further extended this technique for three phases to characterise gas hydrate-bearing sediments.

As the elastic constants of the solid phase in an unconsolidated sediment were not known, different approximations were considered in characterizing the rock properties. A number of previous studies (e.g., Dvorkin and Nur (1996); Zimmer (2003); Dutta et al. (2010)) used the elastic property of a single mineral quartz in contact-based models where several other minerals were present. Helgerud et al. (1999) preferred Hill's average to calculate the effective elasticity of the minerals to input into their rock physics model that characterises gas hydrate deposits. Dutta et al. (2010) calculated the elastic properties of the solid phase by averaging the Hashin-Shtrikman bounds. Dvorkin and Nur (1996) mentioned that it would be logical to use the properties of the composite minerals rather than using the property of the dominant mineral present in the sample. However, they found the composite velocities are not much different to those of quartz; hence, they used the latter. Moreover, Hossain et al. (2011) figured out that the Hertz-Mindlin model might not be adequate to predict the effective elastic properties of the unconsolidated sands if the constituent grains had

significantly different elasticities. To tackle this problem in glauconitic sand that had two minerals – namely quartz and glauconite – they approximated the effective Young's modulus of these two minerals after considering the contacts between themselves and each other. Velocities thus calculated by the Hertz-Mindlin contact model were found to be higher than the velocities calculated using the elasticity of the constituent minerals derived from Hill's average. Sriram et al. (2014) extended the equation to calculate the effective elastic properties of two minerals from Hossain et al. (2011) to three minerals. They applied that parameter into Walton (1987) smooth model to predict the velocities of fluid-saturated, unconsolidated sands and gas hydrate-bearing sands.

The measurement of ultrasonic velocities through unconsolidated rock samples of different mineral mixtures is quite common in the literature, with a variety of objectives. Murphy (1982) measured ultrasonic velocities together with their attenuation of unconsolidated sedimentary materials as functions of the frequency, water saturation, grain characteristics, relative humidity and strain amplitude. Mondol et al. (2010) studied the V_P-V_S relation, calculated from the ultrasonic data of unconsolidated sands during uniaxial compression, with variation in mineralogy, grain shape and sorting. Hagerty et al. (1993) and Chuhan et al. (2003)performed uniaxial stress on unconsolidated materials to study how grain crushing was affected by the initial porosity, particle size, shape and mineral composition. Extensive studies on sand and clay mixtures were carried out by a number of authors. Marion et al. (1992) conducted velocity measurements on brine-saturated, clean Ottawa sand, pure kaolinite and their mixtures to relate the velocity to the mineral contents. Yin (1993) conducted uniaxial stress on unconsolidated sand and clay mixtures to derive the relationships among porosity, permeability and clay content along with their effect on the velocity anisotropy. Koochak Zadeh et al. (2016) performed a uniaxial compaction test on pure quartz sands and sand clay mixtures to investigate the rock physical properties. Fawad et al. (2011) ran a similar test by measuring the ultrasonic velocities of sand samples that contain a number of different minerals. Their measurement revealed that the mineralogy of the samples can affect the elastic wave velocity. In his study on geoacoustics, Hamilton (1980) explains that porosity, compaction and lithology had a significant impact on velocity measurements through unconsolidated sediments. Neither these laboratory measurements nor other studies, to our knowledge,

aimed to obtain the effective elastic moduli of the minerals in an unconsolidated mineral mixture. This chapter attempts to fill this gap by using contact-based models on ultrasonic measurements through multi-mineral granular samples.

Unconsolidated sediments that contain a number of minerals need to have the effective elastic constants calculated by considering the elasticity of the individual minerals. In this study we propose to incorporate a number of minerals in calculating effective Young's modulus following the technique presented in Hossain et al. (2011). Our objective is to obtain elastic properties (e.g. shear modulus and Poisson's ratio) of the constituent minerals by applying the method described in the previous chapter for quartz sand samples. To achieve this, we run an ultrasonic velocity experiment on three rock powder samples collected from a hard rock exploratory drilling well. The velocities are largely controlled by the internal arrangements and types of contacts, which can be explained by Hertzian contact theory. One of the assumptions of Hertzian contact theory is that the contact surface area is likely to be much smaller than the average radius of the grain. Even though the grains in our sample are very fine, we tend to adhere to this assumption. Thus, the elastic constants of the constituent minerals calculated in all three samples have the leverage to compare with respective elastic constants measured in their corresponding core samples collected from the same depth. We have also assumed that the powder samples are representative of the whole depth interval from where the core samples are collected at the corresponding depth.

4.3. Effective medium model for granular packs of various minerals

In the previous chapter, we discussed the effective medium models for a granular medium composed of a single mineral with the same elasticity. Considering two different types of minerals with two significantly different elastic properties, Hossain et al. (2011) proposed a contact model that incorporated three combinations of contacts between those two minerals. The effective Young's modulus resulting from the contact of a dissimilar mineral pair can be calculated from the elastic properties of those two minerals after following Johnson (1985) as,

$$E_{eff(m1m2)} = \left(\frac{1-\nu_{m1}^2}{E_{m1}} + \frac{1-\nu_{m2}^2}{E_{m2}}\right)^{-1} \quad (4.1)$$

where v and E are Poisson's ratio and Young's modulus of the mineral, and subscript $m1$ and $m2$ denote mineral 1 and mineral 2, respectively. Young's modulus of any isotropic material can be formulated in terms of its shear modulus, μ and Poisson's ratio, v, compressional wave velocity, V_P and shear wave velocity, V_S as

$$E = 2\mu(1+\nu) = \rho V_S^2 \left(\frac{3V_P^2 - 4V_S^2}{V_P^2 - V_S^2}\right). \quad (4.2)$$

Using this E from equation 4.2 into equation 4.1, the following equation can be rewritten as

$$E_{eff(m1m2)} = \left(\frac{1-\nu_{m1}}{2\mu_{m1}} + \frac{1-\nu_{m2}}{2\mu_{m2}}\right)^{-1}. \quad (4.3)$$

For the contact between similar minerals in which the elastic properties of $m1$ and $m2$ are the same, the effective Young's modulus of the similar mineral pair in equation 4.3 becomes

$$E_{eff(m1m1)} = \frac{\mu_{m1}}{1-\nu_{m1}} \quad (4.4)$$

For an unequal mixture of two minerals in an unconsolidated granular pack, assuming the different categories of contacts are not dependent on each other, Hossain et al. (2011) approximated the effective Young's modulus of those two minerals in that granular pack while they are in contact. They consider the volume fraction of each mineral and its contribution to the effective Young's modulus as in the following equation

$$E_{eff(2)} = f_{m1}\left(f_{m1} \cdot E_{eff(m1m1)} + f_{m2} \cdot E_{eff(m1m2)}\right) +$$

$$f_{m2}\left(f_{m1} \cdot E_{eff(m1m2)} + f_{m2} \cdot E_{eff(m2m2)}\right), \quad (4.5)$$

where f is the volume fraction of the respective mineral denoted as subscript.

On the other hand, the effective bulk modulus of a dry granular pack expressed in equation 3.1 of the previous chapter for a single mineral case can be rewritten in terms of shear modulus and Poisson's ratio of the mineral as

$$K_{eff} = \left[\frac{C^2(1-\phi)^2\mu^2 P}{18\pi^2(1-\nu)^2}\right]^{\frac{1}{3}} \tag{4.6}$$

where K_{eff}, C, and ϕ are the effective bulk modulus, coordination number and porosity of the granular pack respectively, and P is the hydrostatic pressure. Replacing the grain elastic properties from equation 4.4, equation 4.6 can be rewritten as

$$K_{eff} = \left[\frac{C^2(1-\phi)^2 E_{eff(m1m2)}^2 P}{18\pi^2}\right]^{\frac{1}{3}} \tag{4.7}$$

In the case of a granular pack having two minerals, the effective bulk modulus of the granular pack can be written as

$$K_{eff} = \left[\frac{C^2(1-\phi)^2 E_{eff(2)}^2 P}{18\pi^2}\right]^{\frac{1}{3}} \tag{4.8}$$

Sriram et al. (2014) extended equation 4.5 – which was introduced by Hossain et al. (2011) – for a mixture of three minerals following the same principle by adding one more component factor for the additional mineral. In this study, we are proposing to include more minerals in the dry, unconsolidated granular pack. If the number of minerals is N, equation 4.5 can be extended as

$$\begin{aligned} E_{eff(N)} = {} & f_{m1}\left(f_{m1}\cdot E_{eff(m1m1)} + f_{m2}\cdot E_{eff(m1m2)} \ldots\ldots + f_{mN}\cdot E_{eff(m1mN)}\right) + \\ & f_{m2}\left(f_{m1}\cdot E_{eff(m1m2)} + f_{m2}\cdot E_{eff(m2m2)} \ldots\ldots + f_{mN}\cdot E_{eff(m2mN)}\right) + \\ & \vdots \\ & \vdots \\ & f_{mN}\left(f_{m1}\cdot E_{eff(m1mN)} + f_{m2}\cdot E_{eff(m2mN)} \ldots\ldots + f_{mN}\cdot E_{eff(mNmN)}\right) \end{aligned} \tag{4.9}$$

Now equation 4.8 can be rewritten to calculate the effective bulk modulus of the granular pack that has a number of N minerals,

$$K_{eff} = \left[\frac{C^2(1-\phi)^2 E_{eff(N)}^2 P}{18\pi^2}\right]^{\frac{1}{3}} \tag{4.10}$$

Plugging the effective Young's modulus from equation 4.9 – of the mineral composite while they are in contact – into equation 4.10 and using appropriate parameters, we can predict the effective bulk modulus of a granular pack that has a number of minerals. On the other hand, following the technique described in the previous chapter, we can derive other elastic properties; for example, shear modulus and Poisson's ratio of the constituent minerals from the ultrasonic velocities.

4.4. Description of the samples and corresponding measurements

We have three powder samples (Figure 4.1) collected from rock fragments that came up during drilling for mineral exploration at Brukunga drill site in South Australia (35°00'10.0"S 138°56'16.6"E). The powder samples are fine-grained (<30 μm) and contain a variety of minerals (Table 4.1). Figure 4.2 shows SEM images of powder samples collected from a depth of 190.9 m which is a bit lower than one of our samples. We name the samples according to their end depth as S188, S215 and S309 (the depths are 188m, 215m, and 309m, correspondingly). All the samples have common rock-forming minerals, such as quartz, feldspar and micas; in addition, the former two have two additional heavy minerals, namely pyrite and pyrrhotite. We measure the density of the demoisturised powder samples using a pycnometer. We also calculate the density of the sample by averaging the density of the individual minerals present in the sample. We take the density and elastic properties of the individual minerals from Mavko et al. (2009), shown in Table 4.2. Table 4.3 shows a summary of the sample density measured by different techniques. Both of the calculated densities show very similar values, which suggests that density averaging is an acceptable technique in this case. As the samples are fine grained, we are unable to acquire micro-CT images of the samples with the optimum resolution that is required to calculate the microstructural parameters on a representative elementary volume.

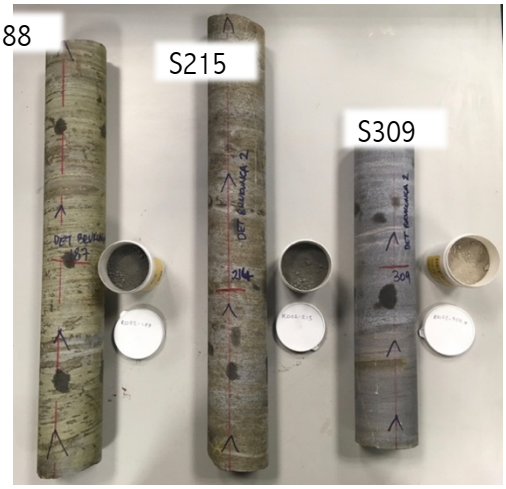

Figure 4.1: Core samples and their corresponding powder samples used in this study.

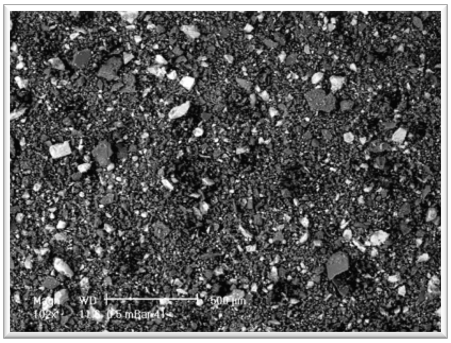

Figure 4.2: SEM images of the powder samples collected from a depth of 190.9 m. Darker grains are commonly recognised as quartz and feldspars, large flakes are commonly biotite and muscovite, and brighter specs are pyrite/pyrrhotite.

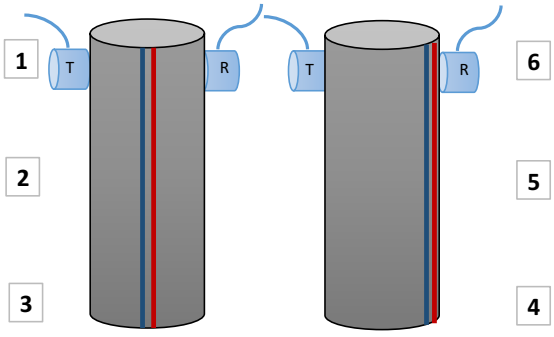

Figure 4.3: Schematic diagram of the ultrasonic measurement positions marked as numbers from 1 to 6 in a core sample with a source (T) and a receiver (R) transducer.

Table 4.1: Sample depth with their mineral composition in percentage.

	Depth	Quartz	Oligoclase	Muscovite	Biotite	Pyrite	Pyrrhotite
S188	186.5-188m	19.4	25.7	29.5	13.3	6.7	5.4
S215	213.5-215m	21.1	22.4	26.6	18.4	3.7	7.7
S309	308-309.5m	24.9	34.6	24.9	15.7	0.0	0.0

Solid core samples from corresponding depths are also available from another hole that is three meters apart (Figure 4.1). They all are from HQ drilling that produced a core diameter of ~63.5 mm. We measure the density and ultrasonic velocities of these core samples. For density measurement, we apply the traditional technique by dividing the mass of the sample by its volume. We calculate the volume of the sample by subtracting the mass of the sample measured in water from the mass measured in air. We consider the density of the water as 1 g/cm^3. Table 4.3 includes this measured density together with the density of the powders measured by pycnometer, and that arrived at by averaging the density of the constituent minerals. The density of the solid core is found to be very much in accordance with the previous two measurements on the powders. We measure the ultrasonic velocities in six different positions of the core sample shown in Figure 4.3 to see the possible anisotropic behaviour. Table 4.4 has all the velocity measurements carried out on the core samples. Samples S188 and S215 have small standard deviation in S wave velocity whereas S309 has comparatively large standard deviation in both of the velocities. This suggests that sample S309 is more anisotropic in a plane perpendicular to the borehole axis than the other two samples. For further calculation, we use the average velocity for both P and S waves.

Table 4.2: Theoretical values of mineral properties found in literature Mavko et al. (2009)

		Quartz	Oligoclase	Muscovite	Biotite	Pyrite	Pyrrhotite
Young's modulus	GPa	94.5	39.7	100.8	102.7	305.9	85.7
Bulk modulus	GPa	37	37.5	61.5	59.7	147.4	53.8
Shear modulus	GPa	44.0	15.0	41.1	42.3	132.5	34.7
Poisson's ratio		0.08	0.32	0.23	0.21	0.15	0.23
Density	g/cm3	2.65	2.62	2.79	3.05	4.93	4.55

Table 4.3: Density of powder samples measured from two different techniques and density of the core sample from corresponding depths.

Density of the core sample	Density of the powder sample	
	from mineral composition	from pycnometer
g/cm3	g/cm3	g/cm3
3.0055	3.0062	2.9966
2.9838	3.0052	2.9967
2.7300	2.7372	2.7506

Prior to putting them inside the odeometric cell, we demoisturise the powder samples in an oven for 24 hours. Following the same experiment setup and loading-unloading cycles presented in the previous chapter in Figure 3.2, we measure the ultrasonic velocities of all the samples. We maintain a scale to measure any change in length for volumetric calculation during each loading step.

The measurements show S215 has the highest P wave velocities whereas S309 has the lowest (Figure 4.4 (a)). These measurements are in accordance with those from Mavko et al. (2009), who found that quartz-poor (<55%) sands tend to have higher velocities

than quartz-rich sands. On the other hand, all three samples have similar S wave velocities at the initial stresses but they differ slightly at the end (Figure 4.4(a)). The V_P/V_S ratio decreases with increasing stress in all the samples, as expected (Figure 4.4(b)). Even though the measured porosity in S215 is as low as 31 percent, the V_P/V_S ratios do not go below 1.731, which is the upper limit that the Extended Walton model (e.g. Jenkins et al. (2005)) allows to validly predict effective elastic properties of unconsolidated granular packs. On the contrary, sample S309 has a V_P/V_S ratio below 1.731 in all measurements except in few at the initial stresses. Interestingly, it has the highest porosity values among the samples.

Table 4.4: Measured velocities of the core samples at different positions shown in Figure 4.3 with their average and standard deviation values.

	S188		S215		S309	
	V_P	V_S	V_P	V_S	V_P	V_S
	m/s	m/s	m/s	m/s	m/s	m/s
Position_1	5983	3640	5568	3610	5430	3422
Position_2	5850	3642	5510	3695	5594	3694
Position_3	6001	3642	5750	3725	5477	3751
Position_4	5740	3671	5668	3553	4861	3402
Position_5	5630	3617	5627	3756	5497	3934
Position_6	5626	3605	5846	3747	5470	3722
Average	5805	3636	5661	3681	5388	3654
Standard Deviation	167	23	122	82	264	206

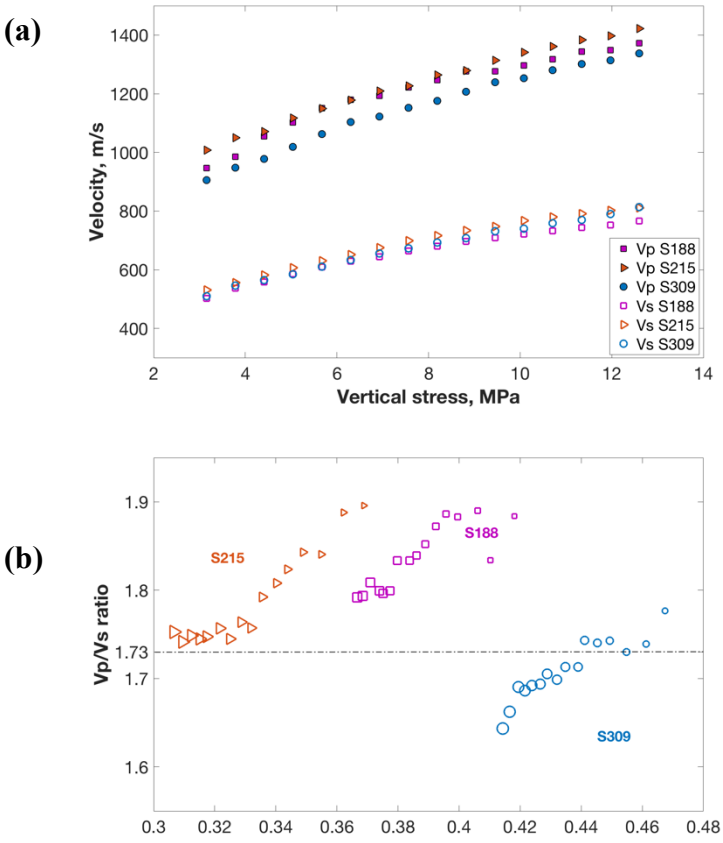

Figure 4.4: (a) Ultrasonic P and S wave velocities of the powder samples with vertical stress. (b) V_P/V_S ratio of the samples with the porosity values. Marker size indicates the stress level. The smallest and largest ones are for 3.15 and 12.6 MPa respectively.

From the mineral composition and their respective theoretical elastic properties presented in Table 4.2, we calculate the effective Young's modulus of the mineral composite, while they are in contact, using equation 4.9 for each sample. Now if we consider a granular pack made of the grains fragmented from a solid core, we can calculate similar effective elastic properties of the composite grains, while they are in contact, using equation 4.4. In that case, we consider the elastic properties of all the grains are the same as the elastic properties of the solid core. We calculate the shear modulus and Poisson's ratio of the grains from the measured velocities of the core sample to input into equation 4.4. Comparison between these two shows that the effective Young's moduli calculated from the mineral composition are less in all three samples (Table 4.5). S188 has the highest difference at 16.12%, whereas S309 has the lowest difference of 8% with respect to the measurements on the core sample.

Table 4.5: Effective Young's moduli of the mineral composite, while they are in contact, calculated from the mineral composition and the velocity data of the core sample.

	$E_{eff(N)}$ from mineral composition	E_{eff} from velocities of core samples	Difference in percentage
	GPa	GPa	
S188	40.51	48.29	16.12
S215	40.43	46.68	13.37
S309	36.35	39.51	8.00

4.5. Forward modelling

Both samples S188 and S215 show similar values of dynamic effective bulk moduli calculated from the ultrasonic measurements. However, S188 shows a slightly steeper trend with increasing stress than the trend in S215. On the other hand, S309 shows lower values of dynamic effective bulk modulus. To calculate the forward models following Walton (1987), we use effective Young's modulus of the mineral composite, while they are in contact, calculated from the mineral composition. Feeding this with the parameters measured from the ultrasonic experiment, we invert equation 4.10 for coordination numbers (Figure 4.5(b)) that provide the best fit between the model and dynamic data. Figure 4.5(a) shows the effective bulk moduli of the powder packs calculated from the dynamic measurements and Walton (1987) model where the coordination numbers used from Figure 4.5(b). Unlike the small changes in coordination numbers throughout the stress range from 3.15 MPa to 12.6 MPa in the quartz sand samples described in the previous chapter, we see significant change throughout the same stress range in all three samples. S188 has the largest increase of around 4, from 10.25 to 14.5 at 3.15 to 12.6 MPa stresses respectively. S309 shows an increase of coordination number around 3 from initial to end stress. S215 shows the lowest increase of around 2.5 among the three.

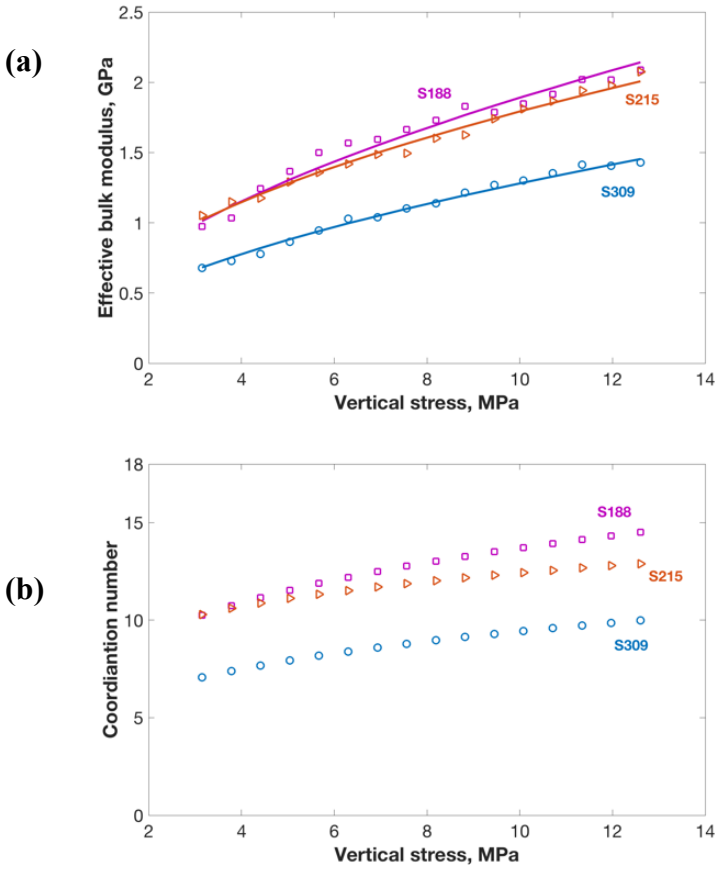

Figure 4.5: (a) Effective bulk moduli of the granular pack calculated using Walton (1987) model (equation 4.6) and dynamic data from ultrasonic measurements. (b) The corresponding coordination numbers used to calculate effective bulk moduli in (a).

4.6. Calculating the elastic moduli of the grains

We have seen in the previous chapter that in predicting the effective shear modulus of the granular pack considering the fraction of no lip contacts, the extended Walton model requires the V_P/V_S ratio of the granular pack to be below 1.731. Among the three samples in this study, only S309 has such a V_P/V_S ratio at the higher stresses. Therefore, we are able to implement the technique described in the previous chapter on this sample only.

The fraction of no slip contacts, α, in S309 calculated from the equation 3.13, shows a range from 0 to 0.2 (Figure 4.6) depending on the applied vertical stresses. As the Poisson's ratio of the grains is unknown, we calculate α with its lower and upper limits

considering the values as 0 and 0.35 respectively. Using these α values, we are able to calculate the lower and upper limits of the shear modulus of the grains (Figure 4.7(a)). A dashed line in that graph represents the shear modulus, which is calculated using ultrasonic velocities of the core sample that is extracted from the same depth. The shear modulus from the core sample lies at the edge of the upper limit, which corresponds to the grains' Poisson's ratio of approximately 0. We determine the single values for both the upper and lower limits from the peak values of the normal distribution curves of both of the datasets (Figure 4.7(b)). These single values provide the constraints that are used in the non-linear, least square solution of equation 3.2 stated in the previous chapter to calculate the shear modulus and Poisson's ratio of the grains. From the least square solution, we obtain the shear modulus of the grains as 30.35 GPa and Poisson's ratio as 0.002, whereas the respective values from the core sample are 36.58 and 0.075 respectively. By converting these values to the velocities, we find a P wave velocity of 4722.41 m/s and an S wave velocity of 3335.90 m/s, whereas the measured average P and S waves velocities of the core sample are 5388.23 and 3654.26 m/s respectively.

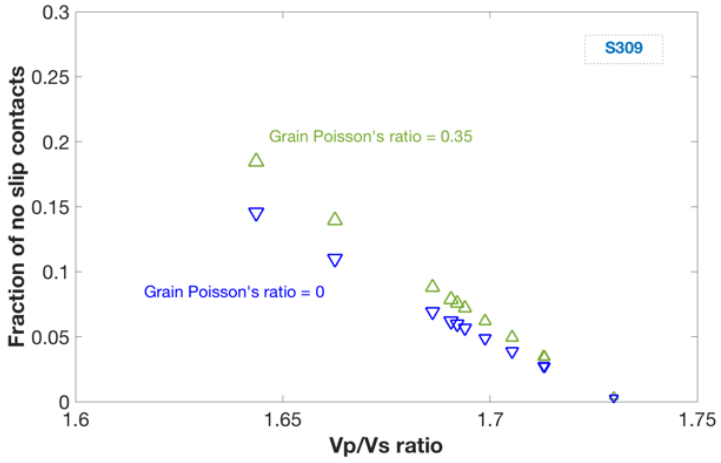

Figure 4.6: Fraction of no slip contact, α, calculated from the V_P/V_S ratio in S309.

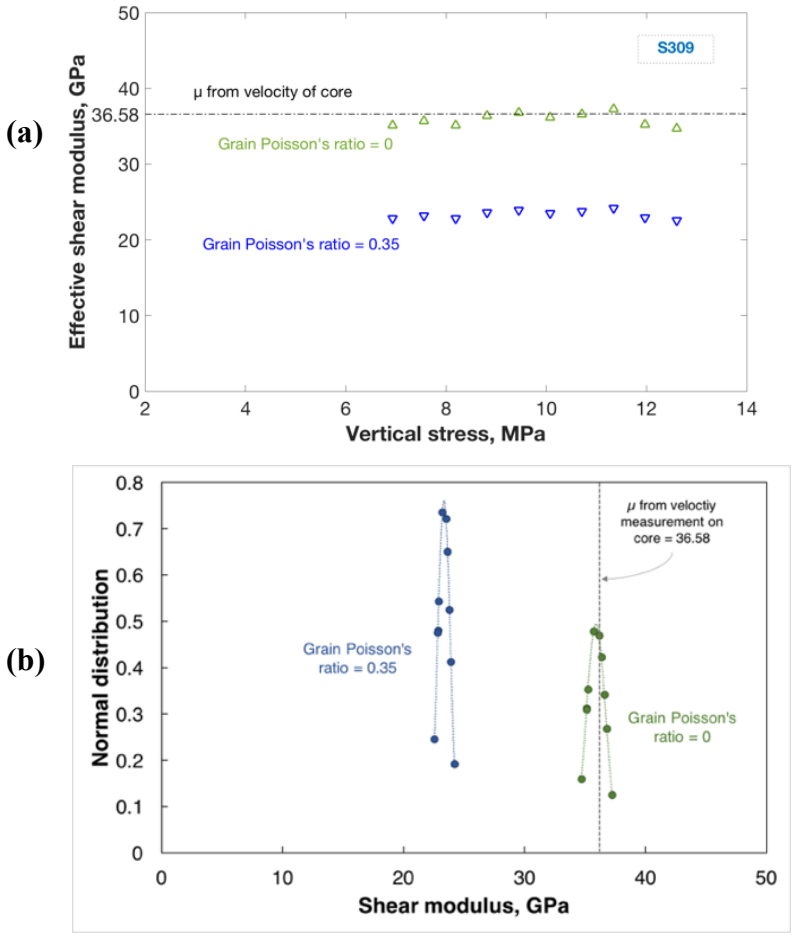

Figure 4.7: (a) Upper and lower limit of effective shear modulus of the composite minerals considering the effective Poisson's ratio of the composite mineral is 0 and 0.35 in S309 (b) The normal distribution curve for the limits to obtain a peak value for each of the limits in S309.

4.7. Discussion

All three samples contain different fractions of the same rock-forming minerals including quartz, feldspar and micas. However, S188 and S215 have two additional heavy minerals: pyrite and pyrrhotite. Solid core samples S188 and S215 extracted from the same depth of the powder samples show limited anisotropy both in P and S wave velocities. On the other hand, S309 has a slightly higher anisotropy in both of the velocities. The average P wave velocities in S188 and S215 are higher than that in S309. This might be explained by the higher density of the former two samples caused by the presence of the two heavy minerals. On the other hand, the S wave velocities are quite close in all three samples. The densities of the core samples, measured from

their mass and volume, show excellent agreement with the densities measured in their corresponding powder samples, in which two separate methods are used. The density of the powder measured using a pycnometer shows very similar values to that calculated by averaging the density of the individual minerals present in the sample.

For ultrasonic measurement through the powder samples, we keep the sample preparation and experiment procedure similar to the experiment with the Esperance Beach sand described in the previous chapter so that we can follow the prototype. Similar to the core samples, P wave velocity through the powders show higher values in S188 and S215 than that in S309. S wave velocities in all the powder samples show values similar to the core samples as well. Porosities in all the samples have larger changes (around 6–7%) than the porosity changes in quartz sand (around 1–3%) from Esperance beach. The presence of flaky minerals such as Muscovite and Biotite in the samples is the main reason for that. Although S188 and S215 have lower porosities, their V_P/V_S ratios are still higher than our desired threshold of 1.731. In contrast, even though the porosities are higher in S309, most of the end stresses have a V_P/V_S ratio under this threshold. This allows us to calculate the elastic properties as well as fractions of no slip contacts for S309. The effective Young's moduli of the grains, while they are in contact, calculated from the velocities of the core samples show higher values than those calculated from the theoretical elasticity of the individual minerals in all three respective powder samples.

Higher values of dynamic effective bulk moduli of powder samples S188 and S215, compared with that of S309, can be associated with the presence of heavy minerals in the former two samples. Coordination numbers that are required to match the effective bulk moduli between the model and dynamic data show significant increase throughout the stress range. Compared with the Esperance Beach sand, in which Cs have an increase of around 0.5, samples from Brukunga show an increase of as much as 4. This may also be caused by the significant change in microstructure that is evidenced by the significant porosity change with increasing stress.

We are able to perform the technique described in the previous chapter only on sample S309 as it has a V_P/V_S ratio below the threshold. The α values calculated from those V_P/V_S ratios show an increasing trend with applied stress, as expected. The upper and lower limits of the shear modulus of the grains using these α values have very steady

flat trend over the stress ranges. This is obviously due to using a non-linear *C* as a function of stress in the model. The *C* values render the model to fit well with the dynamic data, from which, in fact they are calculated. The shear modulus of the respective core sample calculated from the ultrasonic velocity data lies at the verge of the upper limit of the shear modulus of the grains calculated from the model. The reason for this is that the model uses the effective Young's modulus of the mineral composite, while they are in contact, which is found to be 8% lower than that calculated from the measured velocities of the core sample. Therefore, it is obvious that the elastic properties calculated from the model will be under-predicted by the model while it is compared with those of the core sample. However, in sample S309, the small difference allows a good approximation of the calculated elastic properties of the constituent minerals. The results have much proximity to the elastic properties derived from the velocities of the core sample.

4.8. Conclusion

We have expanded the contact model proposed by Hossain et al. (2011) by taking into account multiple minerals to calculate the effective Young's modulus of the composite minerals, while they are in contact, in a granular pack. This effective Young's modulus is found to be lower than the modulus calculated from the ultrasonic velocities at all three corresponding core samples. We have observed that the change in a coordination number with stress is significantly large for all three powder samples compared with the granular sand pack (Figure 3.10(a), from previous chapter 3). A possible explanation for this could be the presence of platy shape minerals that allow the internal microstructure to shrink more. A higher change in porosity with increasing stress than that of the granular sand pack (Figure 3.10(b), from previous chapter 3) also strengthens this fact. A coordination number of the powder (granular) pack sample can be calculated by fitting the dynamic data obtained from the ultrasonic velocities and the model that uses the effective Young's modulus of the mineral composite, while they are in contact. Feeding these parameters into the extended Walton model, further calculations to obtain elastic moduli, such as shear modulus and Poisson's ratio of the grains of a core sample, are possible. Of the three samples, only one (namely S309)-containing only common rock-forming minerals- has V_P/V_S ratios within the valid range in which the contact model is applicable. The calculated shear modulus and

Poisson's ratio in that sample come quite close to those calculated form the velocity data of the respective core sample.

Improvement of this technique may be possible in cases similar to the other two samples (S188 and S215) by modifying the sample preparation procedures and the experiment methods. Samples with larger particle sizes can have more contact surface areas, which may increase the shear wave velocity and eventually bring the V_P/V_S ratio inside the valid range for the model. Moreover, a larger grain size can allow micro-CT images to be acquired, which has been found to be a powerful tool to investigate the microstructure of the sample. Simultaneously, modification in the loading-unloading cycles together with the maximum stress level may provide encouraging results. Thus, calculated elastic moduli of the solid phases can be very helpful in rock physics characterisation of unconsolidated sands composed of multiple minerals with different elasticity. Moreover, this technique can be useful to obtain the elastic constants of crystalline rocks from the fragments that come up during drilling in mineral exploration where core samples are not available.

4.9. Acknowledgements

The work presented in the Chapter 4 has been supported by the Deep Exploration Technologies Cooperative Research Centre, whose activities are funded by the Australian Government's Cooperative Research Centre Programme. This is a DET CRC document. The authors would like to thank Dr Lionel Esteban of CSIRO Perth for his help in measuring the density of the rock powders using a pycnometer. The authors also express their gratitude to the ASEG Research Foundation for sponsoring them with Grant (RF16M04). ZA was supported by a Curtin International Postgraduate Research Scholarship and an Australian Government Research Training Program Scholarship.

4.10. References for Chapter 4

Bachrach, R., Dvorkin, J. & Nur, A. 2000. Seismic velocities and Poisson's ratio of shallow unconsoidated sands. Geophysics 65, 559-564.

Berryman, J.G. 1995. Mixture theories for rock properties. In: A handbook of physical constants (ed. T.J. Ahrens), pp. 205-228. American Geophysical Union, ISBN 1080-305X.

Chuhan, F.A., Kjeldstad, A., Bjørlykke, K. & Høeg, K. 2003. Experimental compression of loose sands: relevance to porosity reduction during burial in sedimentary basins. Canadian Geotechnical Journal 40, 995-1011.

Dutta, T., Mavko, G. & Mukerji, T. 2010. Improved granular medium model for unconsolidated sands using coordination number, porosity , and pressure relations. Geophysics 75, E91-E99.

Dvorkin, J. & Nur, A. 1996. Elasticity of high-porosity sandstones: Theory for two North Sea data sets. Geophysics 61.

Dvorkin, J., Prasad, M., Sakai, A. & Lavoie, D. 1999. Elasticity of marine sediments: Rock physics modeling. Geophysical Research Letters 26, 1781-1784.

Fawad, M., Mondol, N.H., Jahren, J. & Bjørlykke, K. 2011. Mechanical compaction and ultrasonic velocity of sands with different texture and mineralogical composition. Geophysical Prospecting 59, 697-720.

Hagerty, M.M., Hite, D.R., Ullrich, C.R. & Hagerty, D.J. 1993. One-dimensional high-pressure compression of granular media. J. Geotech. Engrg. 119, 1-18.

Hamilton, E.L. 1980. Geoacoustic modeling of the sea floor. The Journal of the Acoustical Society of America 68, 1313-1340.

Hashin, Z. & Shtrikman, S. 1963. A variational approach to the theory of the elastic behaviour of multiphase materials. J. Mech. Phys. Solids 11, 127-140.

Helgerud, M.B., Dvorkin, J., Nur, A., Sakai, A. & Collett, T. 1999. Elastic-wave velocity in marine sediments with gas hydrates: Effective medium modeling. Geophysical Research Letters 26, 2021-2024.

Hertz, H. 1882. On the contact of rigid elastic solids and on hardness. Macmillan Paper 6.

Hill, R. 1952. The elastic behaviour of a crystalline aggregate. Proc. Phys. Soc. London A 65, 349-354.

Hossain, Z., Mukerji, T., Dvorkin, J. & Fabricius, I. 2011. Rock physics model of glauconitic greensand from the North Sea. Geophysics 76, E-199-E209.

Jenkins, J., Johnson, D., La Ragione, L. & Makse, H. 2005. Fluctuations and the effective moduli of an isotropic, random aggregate of identical, frictionless spheres. Journal of the Mechanics and Physics of the Solids 53, 197-225.

Johnson, K.L. 1985. Contact mechanics. Cambridge University Press.

Koochak Zadeh, M., Mondol, N.H. & Jahren, J. 2016. Experimental mechanical compaction of sands and sand-clay mixtures: a study to investigate evolution of rock properties with full control on mineralogy and rock texture. Geophysical Prospecting 64, 915-941.

Marion, D., Nur, A., Yin, H. & Han, D. 1992. Compressional velocity and porosity in sand–clay mixtures. Geophysics 57, 554-563.

Mavko, G., Mukerji, T. & Dvorkin, D. 2009. The Rock Physics Handbook, Second Edition Tools for Seismic Analysis of Porous Media. CAMBRIDGE UNIVERSITY PRESS.

Mondol, N.H., Avseth, P., Fawad, M. & Smith, T. 2010. Vs prediction in unconsolidated sands: Physical and geological controls on shear wave velocities. In: 72nd EAGE meeting.

Murphy, W. 1982. Effects of microstructure and pore fluids on the acoustic properties of granular sedimentary materials. In: PhD dissertation.

Reuss, A. 1929. Berechnung der fliessgrense von mischkristallen auf grund der plastizitatsbedingung fur einkristalle. Zeitschrift fur Angewandte Mathematik and Machanik 9, 49-58.

Saul, M.J. 2014. Pressure-dependent elastic properties of sandstones, with applications to seismic reservoir characterisation and monitoring. In: Centre for Petroleum Geoscience and CO2 Sequestration, Vol. PhD. University of Western Australia.

Sriram, G., Dewangan, P. & Ramprasad, T. 2014. Modified effective medium model for gas hydrate bearing, clay-dominated sediments in the Krishna–Godavari Basin. Marine and Petroleum Geology 58, 321-330.

Voigt, W. 1928. Lehrbuch der Kristallphysik. Teubner, Leipzig. Macmillan, NewYork.

Walton, K. 1987. The effective elastic moduli of a random packing of spheres. J. Mech. Phys. Solids 35, 213-226.

Yin, H. 1993. Acoustic velocity and attenuation of rocks: Isotropy, intrinsic anisotropy and stress-induced anisotropy. In: Department of Geophysics, Vol. PhD. Stanford University.

Zimmer, M.A. 2003. Seismic velocities in unconsolidated sands: measurements of pressure, sorting, and compaction effects. In: Department of Geophysics, Vol. PhD thesis. Stanford University.

5. Conclusions and further studies

The preceding chapters have their own conclusions and recommendations for further studies. However, this chapter contains the summary of those outcomes so they appear altogether.

5.1. Conclusions

The micro-structure or internal arrangement of the grains in an unconsolidated sand plays a vital role in its effective elastic properties. The coordination number, which is one of the key micro-structural parameters, has been derived either from empirical equations or numerical simulations so far in previous studies. In the current study, micro-CT images of four quartz sand samples have been acquired, comprehensively processed and analysed to derive the coordination number and contact surface area with an aim of investigating effective elastic properties for the first time. Grain shape factors that are precisely calculated from the micro-CT images have an impact on the coordination number and contact surface area. Samples with higher sorting indices and more spherical and rounded grains have a larger coordination number and contact surface area than those of the samples with lower sorting indices and less spherical and rounded grains.

A controlled and simple laboratory technique incorporating a comprehensive ultrasonic measurement procedure with increasing uniaxial stress have been presented in this study. Ultrasonic velocities in granular media are largely dependent on the coordination number and contact surface area of the grains. As these micro-structural parameters are controlled by the sorting indices and shape factors of the grains, samples with higher sorting indices and more spherical and rounded grains have higher seismic wave velocities than their counterparts. The coordination numbers calculated from the micro-CT images have been found conducive to fit the dynamic and model data for effective bulk modulus. The approach to calculating the fraction of no slip contact from the dynamic data itself and then plugging in to the model has been found very effective in forward modelling for the effective shear modulus of the sand pack. As a result, the calculated elastic properties of the quartz sand grains appear close to the actual values found in the literature.

This prototype method developed for a quartz sand sample has been successfully applied on one of three rock powder samples that consist of multiple minerals. Higher sensitivity of coordination number and porosity on stress has been observed in these samples compared with a small change in those properties in quartz sand samples. This might be caused by the presence of platy minerals, which can accommodate more internal deformation after changing their orientation while subjected to loading. An extension of an existing model that calculates the effective Young's modulus of a mineral composite while they are in contact has been presented. This effective modulus has been found to be lower than the modulus calculated from the ultrasonic velocities of the corresponding solid core samples collected from the same depth. The calculated elastic properties of the constituent minerals are close to the elastic properties of the corresponding solid core calculated from the ultrasonic velocities. However, only outcomes of one of the three samples have been successful; refining the experiment technique and sample preparation could broaden its validity.

5.2. Further studies

This study can be used as an initiator of a number of topics that could be further explored;

- The relationship among grain shape factors and micro-structural parameters could be further elaborated using a number of samples with a range of sorting indices and grain shape factors. This relationship can be very much helpful in rock physics characterisation for unconsolidated sediments where micro-CT images are not available.
- As a number of ultrasonic measurements have V_P/V_S ratios over the valid range of the model, modification of experiment procedure, such as more loading unloading cycles before final loading, could be applied.
- A standard sample size for the methods described in this thesis could be determined so that acquiring micro-CT images with optimum resolution would be possible hence micro-structural parameters could be accurately calculated.

Copyright consent

For the paper published in *Geophysical Prospecting*, I have found that the no prior permission is required as long as an acknowledgement is presented.

Wiley Online Library | Access by Curtin University Library | rightsLink | Login / Register

Geophysical Prospecting | EAGE

HOME | ABOUT | CONTRIBUTE | BROWSE

Permissions

***PLEASE NOTE: If the links highlighted here do not take you to those web sites, please copy and paste address in your browser.**

Permission to reproduce Wiley journal Content:

Requests to reproduce material from John Wiley & Sons publications are being handled through the RightsLink® automated permissions service.

Simply follow the steps below to obtain permission via the Rightslink® system:

- Locate the article you wish to reproduce on Wiley Online Library (http://onlinelibrary.wiley.com)
- Click on the 'Tools' link and then follow the 'Request Permissions' link
- Follow the online instructions and select your requirements from the drop down options and click on 'quick price' to get a quote
- Create a RightsLink® account to complete your transaction (and pay, where applicable)
- Read and accept our Terms & Conditions and download your license
- For any technical queries please contact customercare@copyright.com
- For further information and to view a Rightslink® demo please visit www.wiley.com and select Rights & Permissions.

AUTHORS - If you wish to reuse your own article (or an amended version of it) in a new publication of which you are the author, editor or co-editor, prior permission is not required (with the usual acknowledgements). However, a formal grant of license can be downloaded free of charge from RightsLink by selecting "Author of this Wiley article" as your requestor type.

Individual academic authors who are wishing to reuse up to 3 figures or up to 400 words from this journal to republish in a new journal article they are writing should select **University/Academic** as the requestor type. They will then be able to download a free permission license.

Either of the above who are publishing a new journal article or book chapter with an **STM Signatory Publisher** may also select that requestor type and the STM Signatory publisher's name from the resulting drop-down list in RightsLink. This list is regularly updated. The requestor is required to complete the republication details, including the publisher name, during the request process. They will then be able to download a free permissions license.

Photocopying

Teaching institutions with a current paid subscription to the journal may make multiple copies for teaching purposes without charge, provided such copies are not resold or copied. In all other cases, permission should be obtained from a reproduction rights organisation (see below) or directly from RightsLink®.

Copyright Licensing Agency

Institutions based in the UK with a valid photocopying and/or digital license with the Copyright Licensing Agency may copy excerpts from Wiley books and journals under the terms of their license. For further information go to CLA.

Submit an Article
Browse free sample issue
Get content alerts
Recommend to a librarian
Subscribe to this journal

Published on behalf of the European Association of Geoscientists & Engineers
EAGE

More from this journal

- Energy Resources Collection
- SEARCH ENGINE OPTIMIZATION Guidelines for Authors
- Journal Information
- Jobs

Advertisement

Wiley Researcher Academy
Online publishing training program
Hear insights direct from the editorial office
Find out more
WILEY

Advertisement

Journal Recommendation service
Find the right journal for your research

Permission to use in PhD thesis

WP Wiley Global Permissions <permissions@wiley.com>
Wed 9/12, 4:25 PM
Zubair Ahmed

Reply all

Flag for follow up. Start by Monday, September 17, 2018. Due by Monday, September 17, 2018.

Dear Zubair,

Thank you for your email.

Permission is granted for you to use the material requested for your thesis/dissertation subject to the usual acknowledgements (author, title of material, title of book/journal, ourselves as publisher) and on the understanding that you will reapply for permission if you wish to distribute or publish your thesis/dissertation commercially.

You should also duplicate the copyright notice that appears in the Wiley publication in your use of the Material. Permission is granted solely for use in conjunction with the thesis, and the material may not be posted online separately.

Any third-party material is expressly excluded from this permission. If any material appears within the article with credit to another source, authorisation from that source must be obtained.

Many thanks,

Orla Davies
Rights Assistant
John Wiley & Sons Ltd

WILEY

...

ZA Zubair Ahmed
Hello, I would like to use our paper (https://doi.org/10.1111/1365-2478.12652) in my PhD thesis as a chapter. Could you please help me by letting me know how I should proceed to get t... Tue 9/4, 5:13 PM